学位論文

A Study of the Zodiacal Emission with the *AKARI* Mid-Infrared All-Sky Maps

（「あかり」中間赤外線全天マップを用いた黄道光の研究）

近藤　徹

Abstract

Our Solar System is rich with interplanetary dust (IPD) mainly of cometary and asteroidal origins. The IPD is observed as the zodiacal light, which is sunlight scattered by the IPD grains in the visible light. On the other hand, the zodiacal emission, thermal emission from the IPD grains is observed in the infrared (IR), which is the major component in the diffuse mid- to far-IR sky brightness. Although the zodiacal emission has been studied for a long time, our understanding is far from being complete. Further investigation of the origin and the distribution of the zodiacal emission will elucidate the dynamical evolution and the physical properties of the IPD.

Previous studies have established the IPD cloud models based on the all-sky IR data obtained by the *IRAS* and the *COBE* satellites. However, these models have not been successful to reproduce the all-sky spatial distribution of the zodiacal emission, especially, in the mid-IR where the zodiacal emission peaks. We therefore aim to improve the IPD cloud model based on Kelsall et al. (1998), using the *AKARI* 9 and 18 μm all-sky survey data which have higher spatial resolution than the *COBE* and the *IRAS* data. Besides studying the IPD, accurate modeling of the zodiacal emission is also important to study the Galactic diffuse dust emission of brightness much lower than the zodiacal emission. In order to robustly determine model parameters, we changed the fitting procedure from Kelsall et al. (1998); we modeled the absolute intensity of the zodiacal emission on a large-scale and a small-scale structure separately by taking a step-by-step procedure.

As a result, we have succeeded in reproducing the all-sky distribution of the mid-IR zodiacal emission significantly better ($\sim 50\%$) than the previous studies. We study the properties of the IPD, using the parameters of the zodiacal emission newly obtained with the improved IPD cloud model. We find that the radial distribution of the smooth cloud, a dominant component of the IPD cloud, is more compact than previously thought. This distribution is different from that expected if the IPD grains are falling into the Sun from outer regions of our Solar System by the Poynting-Robertson effect. Therefore, our result suggests the necessity of additional dust supply mechanisms around 1 AU. We also find that the distribution of the dust temperature cannot be explained by the dust grains emitting the blackbody radiation, which indicates that the dust sizes are not large enough to emit the blackbody radiation in the mid-IR. Furthermore we significantly detect an isotropically-distributed component, owing to accurate baseline measurement with *AKARI*. This component is likely to be the IPD grains of interstellar origins which come from outside our Solar System.

Comparing the *AKARI* and the *COBE* data, we confirm that the changes of the parameters from the previous model to the new model are mostly due to model improvement, but not temporal variations between the *AKARI* and the *COBE* epoch, except for the distribution of the Earth-trailing blob, a dust cloud trapped on the trailing side of the Earth. We find that the position of

the Earth-trailing blob has moved to the north direction between the *COBE* and the *AKARI* epoch, which may suggest that dust is recently supplied by comets near the Earth, asymmetrically trapped on the trailing side of the Earth. In addition to the IPD cloud, we serendipitously detected a likely local cloud passing near the Earth. Considering the observed date and position of the cloud, it may be related to the solar coronal mass ejection which took place on 2007 January 25.

Contents

1 Introduction **1**

1.1 Interplanetary Dust . . . 1

1.1.1 IPD Cloud Component . . . 3

1.1.1.1 Smooth Cloud . . . 3

1.1.1.2 Dust Bands . . . 3

1.1.1.3 Mean Motion Resonance (MMR) Component . . . 4

1.1.2 Dust Temperature . . . 6

1.1.3 Origin of the IPD . . . 7

1.2 *AKARI* Satellite . . . 8

1.3 Objectives of This Study . . . 9

2 Observations and Data Reduction **11**

2.1 *AKARI* Mid-IR All-Sky Survey . . . 11

2.2 Production of the All-Sky Maps . . . 12

2.2.1 Basic Process . . . 14

2.2.2 Map Production . . . 23

2.2.3 Corrections for the Maps . . . 24

3 Modeling of the Zodiacal Emission **39**

3.1 The Kelsall Model . . . 39

3.1.1 Model Components . . . 41

3.1.1.1 Smooth Cloud . . . 41

3.1.1.2 Dust Bands . . . 43

3.1.1.3 MMR Component . . . 43

3.2 Fitting Technique . . . 43

3.2.1 One-Dimensional Fitting at the Poles and on the Plane . . . 49

3.2.2 Two-Dimensional Fitting of the All-Sky Maps . . . 49

3.2.3 Uniqueness of the Model Parameters 50

4 Results **53**

4.1 Improvement of the Zodiacal Model Fitting 53

4.2 Differences between the New Model and the Kelsall Model 56

4.3 Confirmation of the Time Variation of the Zodiacal Emission 58

5 Discussion **65**

5.1 Radial Distribution 65

5.2 Time Variation of the Blob Structure 67

5.3 Origin of the IPD 68

5.4 Small-Scale Structures of the Dust Bands 69

5.5 Likely Local Cloud Passing near the Earth 75

6 Final Products and Future Works **79**

7 Summary **83**

Acknowledgments **85**

List of Figures

1.1 IPD cloud models shown in Giese et al. (1986) 2
1.2 Radial distributions of the smooth cloud models 4
1.3 Isodensity contours for the smooth cloud models 5
1.4 Numerical simulation of the structure of the MMR component 6
1.5 DIRBE 12 μm map after subtraction of the smooth cloud 6
1.6 Radial temperature distributions of the IPD cloud models 7
1.7 Relative spectral response curves of the *AKARI* bands with the zodiacal emission and the ISM emission spectra 8
1.8 DIRBE mid-IR all-sky maps after subtraction of the zodiacal emission with the Kelsall model 10

2.1 Schematic view of the detector array and image reconstruction method 12
2.2 Outline of the mid-IR all-sky survey data processing 13
2.3 Example of the processed data 14
2.4 Schematic image of the detector circuit (one pixel) 15
2.5 Schematic images of the effects of the reset anomaly and the non linearity on the observational data 15
2.6 Example of the images affected by the reset anomaly and the non linearity 16
2.7 Schematic image for showing the method of the estimation of the constant real intensity of the incident light 17
2.8 Schematic image for showing the method of the estimation of the quadratic real intensity of the incident light 17
2.9 Correction functions for the non linearity 18
2.10 Time variations of the offset levels caused by the reset anomaly 19
2.11 Comparing the present corrections for the reset anomaly and the non linearity with the previous corrections 20
2.12 Flat functions for the one-dimensional arrays in the 9 and 18 μm bands 21

2.13 Examples of the pattern of the scattered light in the camera 22
2.14 Example of the detections of point sources 23
2.15 Example of the image affected by the ionizing radiation 25
2.16 Amount of radiation is overlaid on the world map 26
2.17 Correlation plots between the output offset level and the hitting rate of cosmic rays 26
2.18 Example of the formerly-established correction for the ionizing radiation effect . . . 27
2.19 *AKARI* 9 and 18 μm images after the formerly-established correction for the ionizing radiation effect 27
2.20 *AKARI* 9 and 18 μm images after the newly-established correction for the ionizing radiation effect 28
2.21 Image of the region affected by the scattered light from the moon 29
2.22 Template map of the scattered light from the moon 29
2.23 Time variation of the relative sensitivity in the 18 μm band 30
2.24 Images of NGC 7023 in the 9 μm band 31
2.25 Relations between the brightness of the all-sky survey observation and that of the pointed observation 31
2.26 Images of η Car in the 9 and 18 μm bands (Example of the stray light from bright sources) 33
2.27 Difference image of η Car between Phases 1 and 2a 34
2.28 Images of η Car after masking the stray light in the 18 μm band 34
2.29 Images of η Car after subtraction of the stray light in the 9 and 18 μm bands 35
2.30 *AKARI* mid-IR all-sky diffuse maps after subtraction of the zodiacal emission in the ecliptic coordinates 36
2.31 Templates of the distributions of the earthshine 37
2.32 *AKARI* mid-IR all-sky diffuse maps after combining all the seasonal maps 38

3.1 Brightness variations at the ecliptic poles against the Earth's position 40
3.2 Three-dimensional distributions of the IPD cloud components in the Kelsall model . 42
3.3 *AKARI* mid-IR all-sky diffuse maps on the plane of the ecliptic latitude versus the Julian day relative to 2006 April 24 44
3.4 *AKARI* mid-IR all-sky diffuse maps after masking the regions affected by the Galactic emission and the earthshine 45
3.5 Process of the modeling of the zodiacal emission 47
3.6 Surface brightness profiles observed at the ecliptic poles and on the ecliptic plane . . 48
3.7 *AKARI* 9 μm map after subtraction of the zodiacal emission other than Earth-trailing blob and the blob model map 50

3.8 Surface brightness profiles observed on the ecliptic plane with the α and δ changes . 51
3.9 Confidence contours of α and δ 52

4.1 *AKARI* mid-IR maps after subtraction of the zodiacal emission with the new model 54
4.2 *AKARI* mid-IR maps after subtraction of the zodiacal emission with the Kelsall model 55
4.3 Histograms of the residual brightness after subtraction of the zodiacal emission . . . 56
4.4 Isodensity contours for the smooth cloud with the model and the Kelsall model . . . 58
4.5 Residual maps after subtraction of the zodiacal emission with and without introducing $Z_{0,\mathrm{TB}}$ 60
4.6 DIRBE Solar Elongation = 90 deg Sky Maps after subtraction of the zodiacal emission with the new model 61
4.7 DIRBE 12 μm and *AKARI* 9 μm trailing-side maps after subtraction of the zodiacal emission with the new model 62
4.8 DIRBE Solar Elongation = 90 deg Sky Maps after subtraction of the zodiacal emission 63

5.1 Correlation plots between the observed brightness and the predicted brightness . . . 68
5.2 *AKARI* 18 μm map after subtraction of the zodiacal emission without the dust bands and the dust band model map 70
5.3 Cutting profiles of the dust bands for the observed and the model predicted brightnesses 72
5.4 Cutting profiles of the dust bands predicted by the Kelsall model 73
5.5 Cutting profiles of the dust bands which are spatially band-pass-filtered 74
5.6 The position of a likely local cloud passing near the Earth in the *AKARI* mid-IR maps 76
5.7 Solar elongation of the CME fronts as a function of the date 77
5.8 Fish-eye view of the interplanetary CME brightness distribution 77

6.1 *AKARI* 9 and 18 μm all-sky maps after subtraction of the zodiacal emission in the galactic coordinates 80
6.2 *AKARI* 9 and 18 μm all-sky maps after subtraction of the zodiacal emission in the galactic coordinates after masking the regions of brightness levels lower than the thresholds 81
6.3 Enlarged view of the Taurus and the Orion regions in the 9 μm map 82

List of Tables

2.1 Parameters for the mid-IR all-sky survey operation 12

4.1 Parameters of the IPD cloud model in Kelsall et al. (1998) and in the present study 57

5.1 Comparison of the radial distribution of the IPD cloud between the present study and other representative studies 66

Chapter 1

Introduction

1.1 Interplanetary Dust

It is known that our Solar System is rich with dust of cometary and asteroidal origins within a few AU of the Sun from previous studies based on both ground-based observations and space observations. The interplanetary dust (IPD) is observed as the zodiacal light, which is sunlight scattered by the IPD grains in the ultraviolet (UV), visible, and near-infrared (IR), and observed as the thermal emission from the IPD grains in the mid- to far-IR (the zodiacal emission). At IR wavelengths of about 1–100 μm, the signal from the IPD is the major component in the diffuse sky brightness and dominant in the mid-IR ($\sim$10–60 μm) (Kelsall et al. 1998).

The zodiacal light has been observed in the visible light as a faint diffuse glow seen in the night sky along the ecliptic plane since the remote past when the IPD was not known at all. Cassini (1685) firstly proposed that the zodiacal light could be caused by a lenticular dust cloud centered on the Sun with its main axis lying on the ecliptic plane. In the early 1940s, Fessenkov considered the IPD distribution as a prolate spheroid surrounded by a dust torus, which is formed from fragmentation of asteroids in the asteroid belt (Struve 1943). Giese et al. (1986) summarized the early studies on modeling of the three-dimensional distribution of the IPD based on the visible scattered light. They reviewed several kinds of models such as fan, ellipsoid, sombrero, and multilobe models. These models consist of two factors which are related to the distance from the Sun, R, and the elevation from the symmetry plane of the IPD cloud, $\zeta \equiv |Z/R|$, as

$$n(X, Y, Z) = n_0 R^{-\alpha} f(\zeta), \tag{1.1}$$

where $n(X, Y, Z)$ is the dust density at position (X, Y, Z), n_0 is the dust density at 1 AU, and R is given in units of AU. For the radial distribution, the ground-based observations and the space

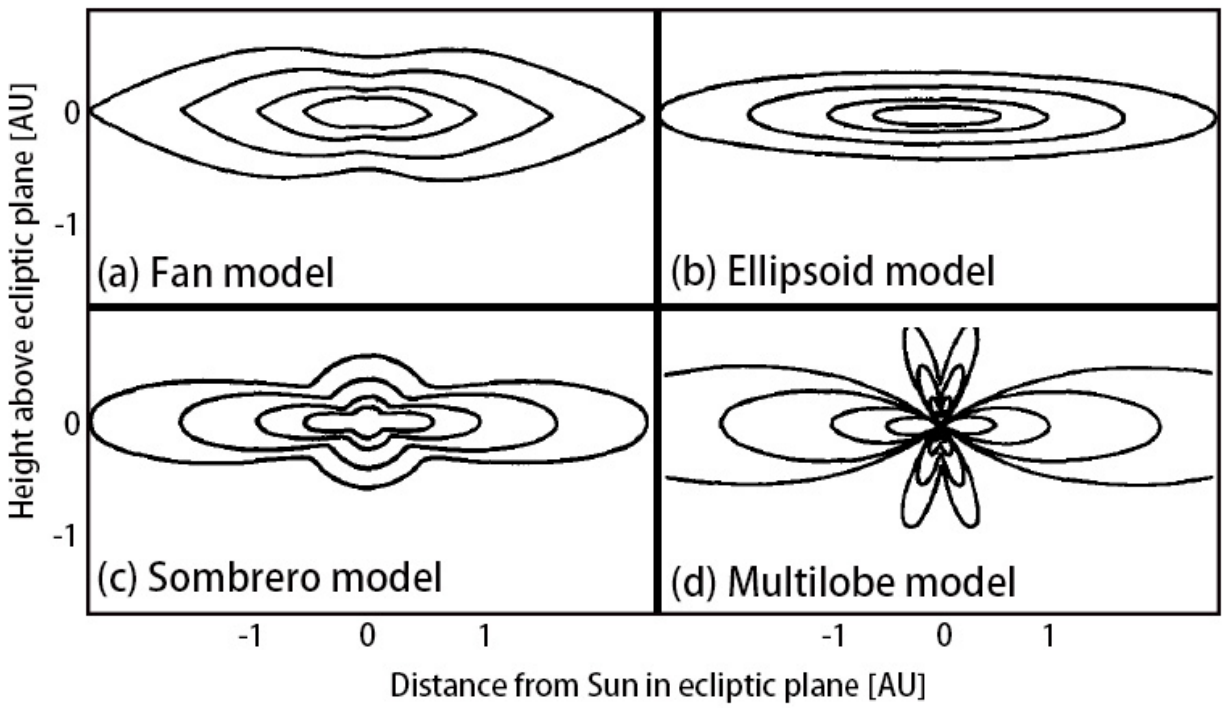

Figure 1.1 IPD cloud models shown in Giese et al. (1986): (a) fan model, (b) ellipsoid model, (c) sombrero model, and (d) multilobe model. The drawing planes are the heliocentric meridian planes. Curves represent isodensities for $n = 2n_0$, $1n_0$, $0.5n_0$, $0.3n_0$ from inner to outer contours.

observations with probes showed $\alpha = 1.0$–1.5 (e.g., Dumont & Sánchez 1975; Hanner et al. 1976; Leinert et al. 1981). For the vertical distribution, the shape of the IPD cloud depends on $f(\zeta)$. Figure 1.1 shows isodensity contours of the IPD cloud models shown in Giese et al. (1986). Among them, the fan model has been considered to be the most popular form for $f(\zeta)$ in equation (1.1) as

$$f(\zeta) = \exp(-\beta\zeta). \tag{1.2}$$

In the 1980s, the zodiacal emission came to be observed with satellites in the IR. The *IRAS* observations in 1983 gave the first all-sky maps of the zodiacal emission and revealed that the cloud has more complicated structures. In addition to a smooth cloud, which is a widely spread component, Low et al. (1984) found asteroidal dust bands based on the *IRAS* data. Rowan-Robinson et al. (1990) and Jones & Rowan-Robinson (1993) gave the first full models of the zodiacal emission based on the *IRAS* data. The former study modeled only the smooth cloud, while the latter study modeled not only the smooth cloud but also the dust bands. Wheelock et al. (1994) also made the IPD cloud model including only the smooth cloud to produce the *IRAS* Sky Survey Atlas maps. In 1989–1990, the Diffuse Infrared Background Experiment (DIRBE) on board *COBE* gave the all-sky

maps of the zodiacal emission, which has information on wider ranges of wavelengths (1.25–240 μm) and of the solar elongations (64°–124°) than those of the *IRAS* data. Furthermore, an absolute brightness calibration for the DIRBE data is better than that for the *IRAS* data. However, the spatial resolution of the DIRBE data is lower than that of the *IRAS* data. Based on the DIRBE data, Reach et al. (1995) confirmed a mean motion resonance (MMR) component trapped by the Earth into resonant orbits near 1 AU. Wright (1998) and Kelsall et al. (1998) constructed an IPD cloud model including the smooth cloud, the dust bands, and the MMR component based on the DIRBE data. Recently, Rowan-Robinson & May (2013) made the model which reproduces both *IRAS* and DIRBE data.

1.1.1 IPD Cloud Component

1.1.1.1 Smooth Cloud

In the above studies with *IRAS* and *COBE*, the fan model (equations (1.1) and (1.2)) was adopted as the spatial distribution of the smooth cloud. For the radial distribution, Rowan-Robinson et al. (1990) and Rowan-Robinson & May (2013) used $\alpha = 1.3$ obtained form the space observations with the *Helios 1* and *2* space probes (Leinert et al. 1981) in their models, while Jones & Rowan-Robinson (1993) used $\alpha = 1$ in their model assuming that the orbital evolution of the IPD grains is dominated by the Poynting-Robertson effect. On the other hand, Wheelock et al. (1994), Wright (1998), and Kelsall et al. (1998) determined the α values to be 1.80 ± 0.01, 1.2186 (the error is not written in the paper), and 1.34 ± 0.02, respectively, by fitting the *IRAS* or the DIRBE data. Figure 1.2 shows the radial profiles of the dust density of the smooth cloud models. For the vertical distribution, the formulation of $f(\zeta)$ in equation (1.2) was modified to better fit the *IRAS* or the DIRBE data in each study. For example, Figure 1.3 shows the isodensity contours of the smooth cloud models in Wheelock et al. (1994), Kelsall et al. (1998), and Rowan-Robinson & May (2013).

1.1.1.2 Dust Bands

The dust bands represent asteroidal collisional debris (Dermott et al. 1984; Nesvorný et al. 2006, 2008), which were first discovered by *IRAS* (Low et al. 1984). The IPD grains are slowly spiraling inward by the Poynting-Robertson effect and the dust bands are thought to be produced by replenishment from main-belt asteroids. The dust bands appear as pairs which are symmetrical with respect to the ecliptic plane. The model constructed by Kelsall et al. (1998) contains three pairs of the dust bands, called bands 1, 2, and 3, which appear at the ecliptic latitudes around $\pm 10°$, $\pm 1\overset{\circ}{.}4$, and $\pm 15°$, respectively. The *IRAS* data revealed more dust bands owing to higher spatial resolution than that of the DIRBE data, and the bands are called bands α, β, γ, E/F, G/H, J/K, and M/N

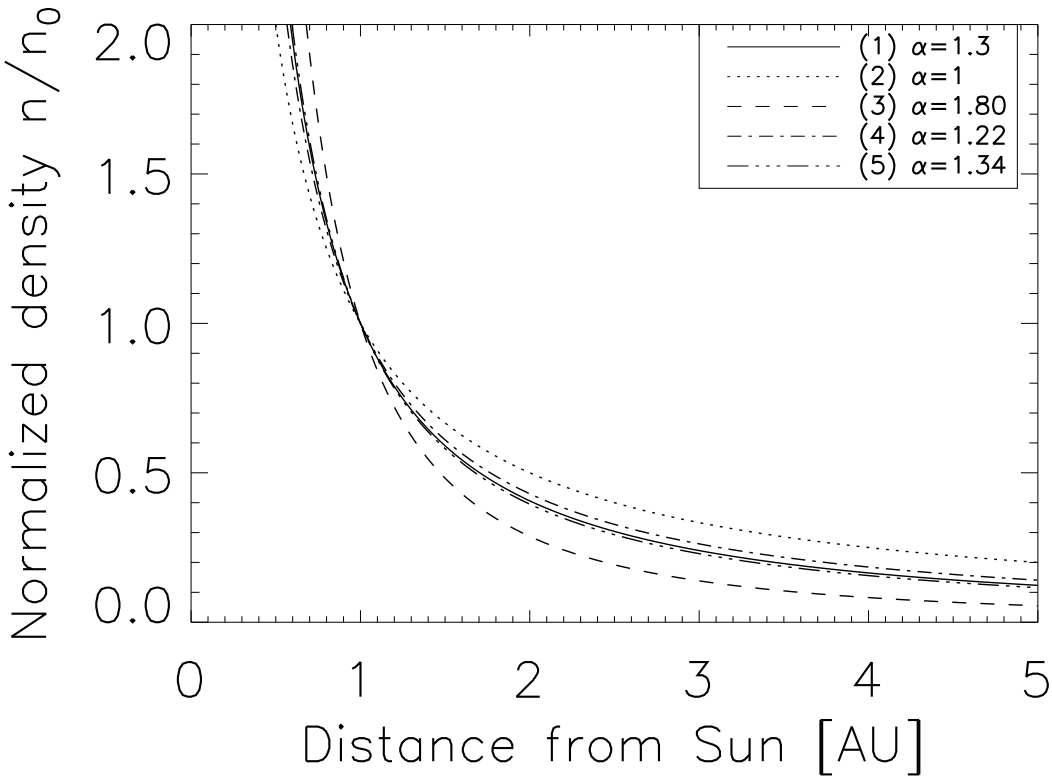

Figure 1.2 Radial distributions of the smooth cloud models: (1) $\alpha = 1.3$; Rowan-Robinson et al. (1990) and Rowan-Robinson & May (2013), (2) $\alpha = 1$; Jones & Rowan-Robinson (1993), (3) $\alpha = 1.80$; Wheelock et al. (1994), (4) $\alpha = 1.22$; Wright (1998), and (5) $\alpha = 1.34$; Kelsall et al. (1998). The density is normalized by that at 1 AU.

(Sykes 1990).

Band 1 or band γ had been considered to be associated with the Eos family of asteroids (Dermott et al. 1984; Sykes & Greenberg 1986; Reach et al. 1997). However, Nesvorný et al. (2003) suggested the origin of band 1 to be the Veritas family. Band 2 is a blend of bands α and β, which are considered to be associated with the Themis and the Koronis families, respectively (Dermott et al. 1984; Sykes & Greenberg 1986; Reach et al. 1997). Band 3 is a blend of bands J/K and M/N, which had been considered to be associated with the Eunomia and the Maria families, respectively. However, Nesvorný et al. (2003) suggested other candidates for the origin of the bands: the compact asteroid clusters around (4652) Iannini and (845) Naema for band J/K, and the clusters around (1521) Seinajoki for band M/N.

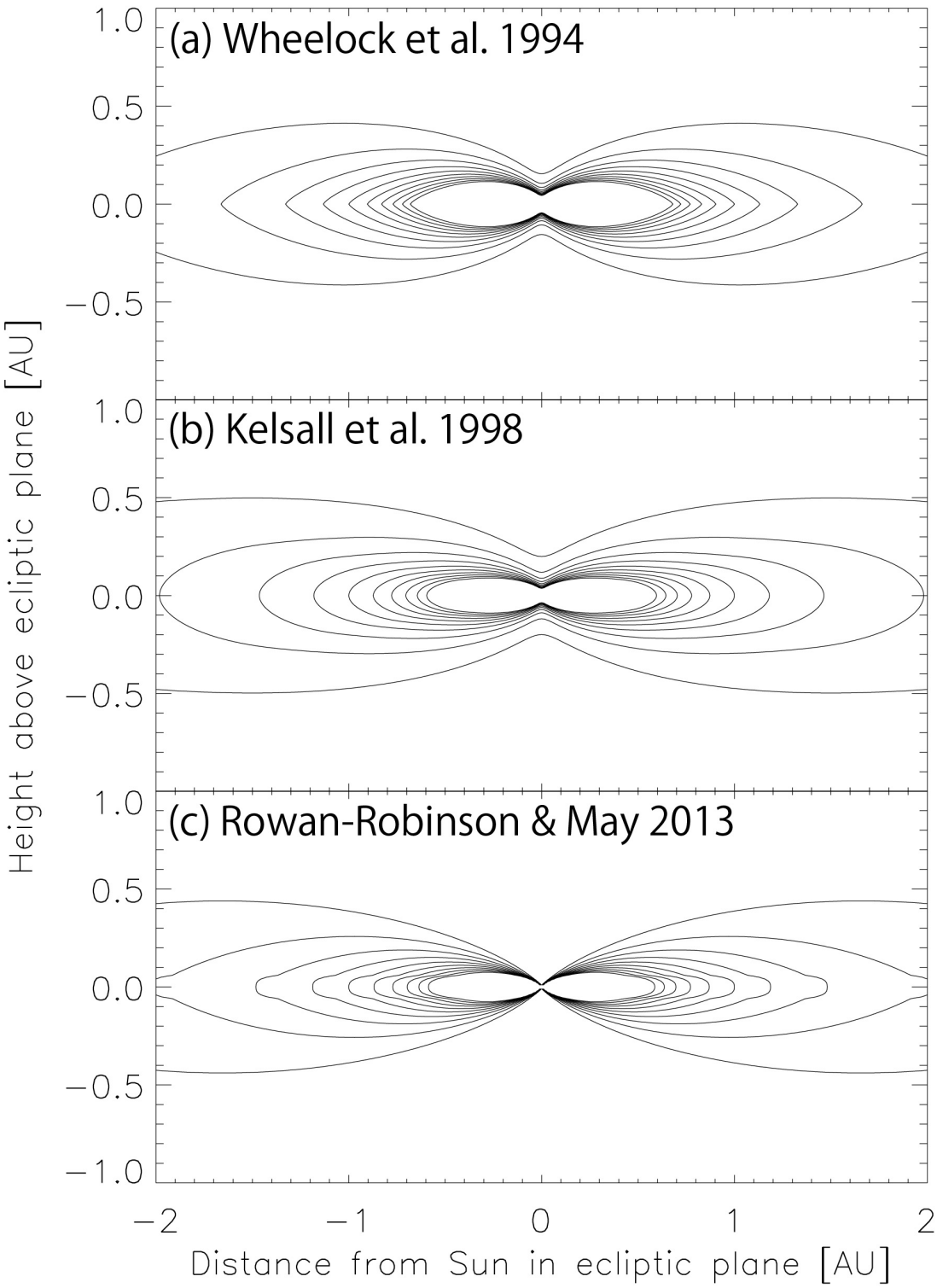

Figure 1.3 Isodensity contours for the smooth cloud models: (a) Wheelock et al. (1994), (b) Kelsall et al. (1998), and (c) Rowan-Robinson & May (2013). The drawing planes are the heliocentric meridian planes. Curves represent isodensities for $n = 2.0n_0$, $1.8n_0$, $1.6n_0$, $1.4n_0$, $1.2n_0$, $1.0n_0$, $0.8n_0$, $0.6n_0$, $0.4n_0$, $0.2n_0$ from inner to outer contours.

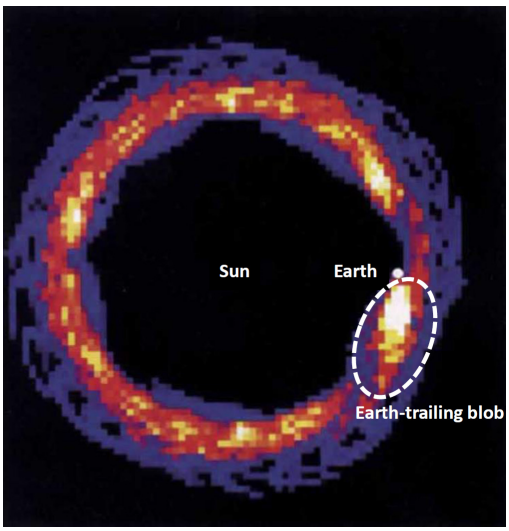

Figure 1.4 Numerical simulation of the structure of the MMR component (Dermott et al. 1994).

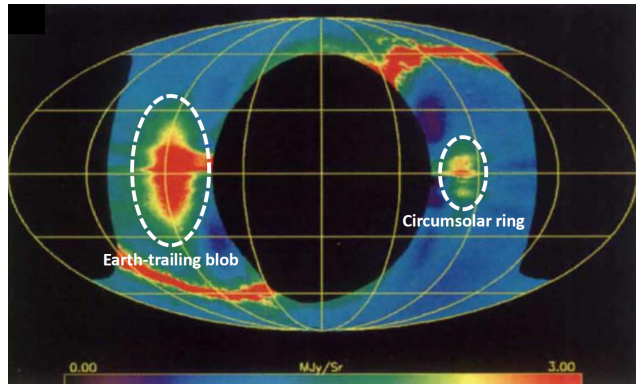

Figure 1.5 DIRBE 12 μm map obtained by the one-week observation from 1990 July 2, in the ecliptic coordinates with the Sun in the center (Reach et al. 1995). The smooth cloud is subtracted.

1.1.1.3 Mean Motion Resonance (MMR) Component

The MMR component is composed of migrating dust grains, which are temporarily trapped into resonant orbits near 1 AU by the Earth. This component had been expected theoretically (Jackson & Zook 1989; Marzari & Vanzani 1994a,b; Dermott et al. 1994, 1996). Figure 1.4 shows the distribution of the MMR component obtained from the numerical simulation by Dermott et al. (1994). It has a ring-like structure whose radius is about 1 AU (a circumsolar ring) with an enhancement in a three-dimensional blob trailing the Earth (hereafter called Earth-trailing blob). The existence was confirmed by Reach et al. (1995) based on the DIRBE data as shown in Fig. 1.5, which is the residual map after subtraction of the smooth cloud in the DIRBE 12 μm band. We can see the cross-sections of both circumsolar ring and Earth-trailing blob in Fig. 1.5.

1.1.2 Dust Temperature

IR observations enable us to estimate the distribution of the IPD temperature. The dust temperature, T, is considered to vary with the distance from the Sun, R, as

$$T(R) = T_0 R^{-\delta}, \tag{1.3}$$

where T_0 is a dust temperature at 1 AU. The power-law index, δ, and the temperature at 1 AU, T_0, should be 0.5 and 279 K, respectively, if the dust grains emit the blackbody radiation in the thermal equilibrium. In practice, the dust temperature depends on the dust size and the albedo in the UV

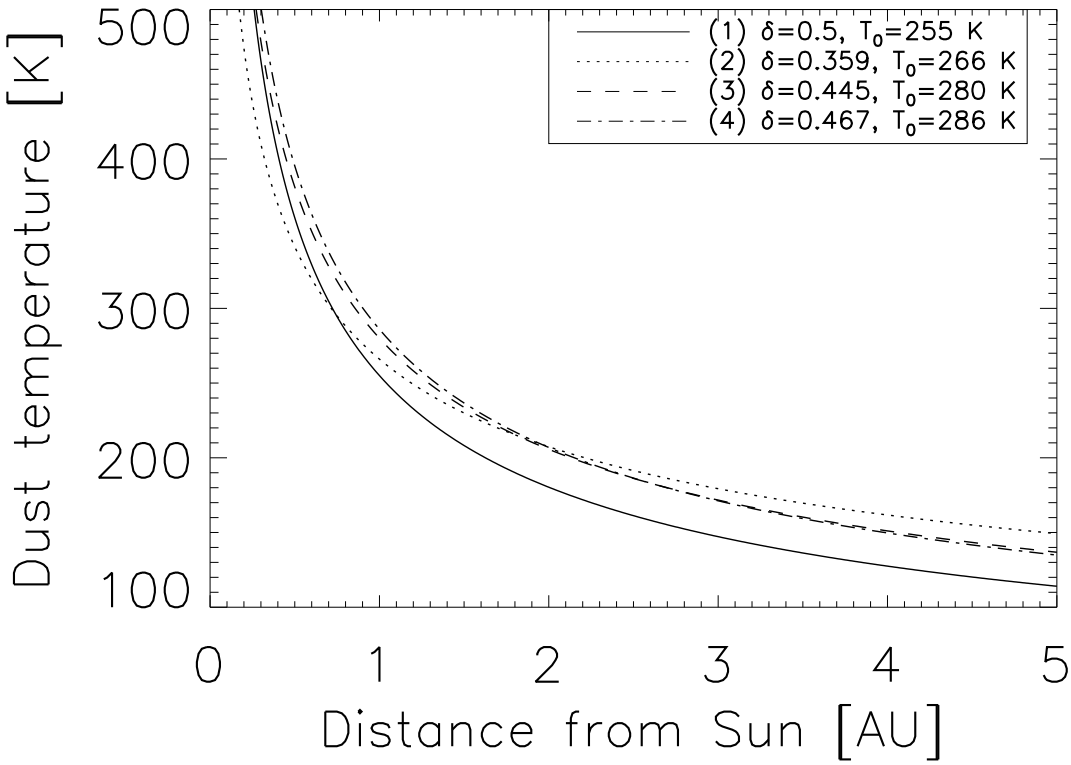

Figure 1.6 Radial temperature distributions of the IPD cloud models: (1) $\delta = 0.5$, $T_0 = 255$ K; Rowan-Robinson et al. (1990), Jones & Rowan-Robinson (1993), and Rowan-Robinson & May (2013), (2) $\delta = 0.359$, $T_0 = 266$ K; Wheelock et al. (1994), (3) $\delta = 0.445$, $T_0 = 280$ K; Wright (1998), and (4) $\delta = 0.467$, $T_0 = 286$ K, Kelsall et al. (1998).

and visible light. Rowan-Robinson et al. (1990), Jones & Rowan-Robinson (1993), and Rowan-Robinson & May (2013) fixed the δ value at 0.5, assuming that the dust sizes are large enough to emit blackbody radiation in the IR (i.e., typical radii > 10 μm). On the other hand, Wheelock et al. (1994), Wright (1998), and Kelsall et al. (1998) determined the δ value to be 0.359 ± 0.004, 0.4451 (the error is not written in the paper), and 0.467 ± 0.004, respectively, by fitting the *IRAS* or the DIRBE data. Rowan-Robinson et al. (1990) and Kelsall et al. (1998) estimated the T_0 value to be 255 and 286 K, respectively, using the mid-IR band data on the assumption that the dust emits blackbody radiation. Once the T_0 value was obtained, they fixed the T_0 value when they determined the other model parameters. Jones & Rowan-Robinson (1993) and Rowan-Robinson & May (2013) adopted $T_0 = 255$ K in their models. Wheelock et al. (1994) determined the T_0 value to be 266.2 ± 0.2 K simultaneously with the other model parameters. On the other hand, Wright (1998) assumed $T_0 = 280$ K, which is almost the same as the equilibrium temperature, 279 K. We

summarize the radial temperature distribution of each model in Fig. 1.6.

1.1.3 Origin of the IPD

Although it has been considered that the origins of the IPD are cometary, asteroidal, and interstellar dust grains, the proportion of them is not well known. From a study of 200 captured dust grains, Schramm et al. (1989) found that 45% of the grains are of a cometary origin and 37% of those are of an asteroidal origin. Liou et al. (1995) carried out a dynamical analysis and found that a mixture of 74% cometary and 26% asteroidal dust matches the *IRAS* brightness profiles. Durda & Dermott (1997) showed that 34% of the IPD cloud arises from collisional destruction of asteroids using numerical modeling. In addition to the cometary and the asteroidal origin dust, Baguhl et al. (1995) found that interstellar dust is flowing into our Solar System using the *Ulysses* dust-detection data. Grogan et al. (1996) showed that the contribution of the brightness of the IPD from the interstellar dust is small (<0.1 MJy sr^{-1} at 12 μm), while Rowan-Robinson & May (2013) claimed that Baguhl et al. (1995) underestimated the density of the interstellar dust.

1.2 *AKARI* Satellite

AKARI (Murakami et al. 2007), the first Japanese IR astronomical satellite, was launched on 2006 February 21 (UT) and was brought into a sun-synchronous orbit at an altitude of 700 km. *AKARI* has a telescope of 68.5 cm aperture diameter cooled at 6 K by liquid helium and mechanical coolers (Kaneda et al. 2005, 2007). Two scientific focal-plane instruments on board the *AKARI* satellite, the Infrared Camera (IRC; Onaka et al. 2007) and the Far-Infrared Surveyor (FIS; Kawada et al. 2007), cover the wavelengths of 1.8–26.5 μm and 50–180 μm, respectively. *AKARI* carried out the all-sky survey during a period from 2006 May 8 to 2007 August 28 and covered about 94% of the whole sky. The 9 and 18 μm photometric bands of the IRC and the 65, 90, 140, 160 μm bands of the FIS were used for the all-sky survey. The spectral response curves of these bands are shown in Fig. 1.7. In addition to the all-sky survey, *AKARI* carried out pointed observations including both imaging and spectroscopy. After exhaustion of liquid helium, only the near-IR spectroscopic observations were continued until May 2010.

1.3 Objectives of This Study

As mentioned above, the zodiacal emission in the mid- to far-IR has information on both density and temperature distributions of the IPD, and many authors modeled the IPD cloud using the IR all-sky data. However, accurate modeling of the zodiacal emission has not been successful to reproduce

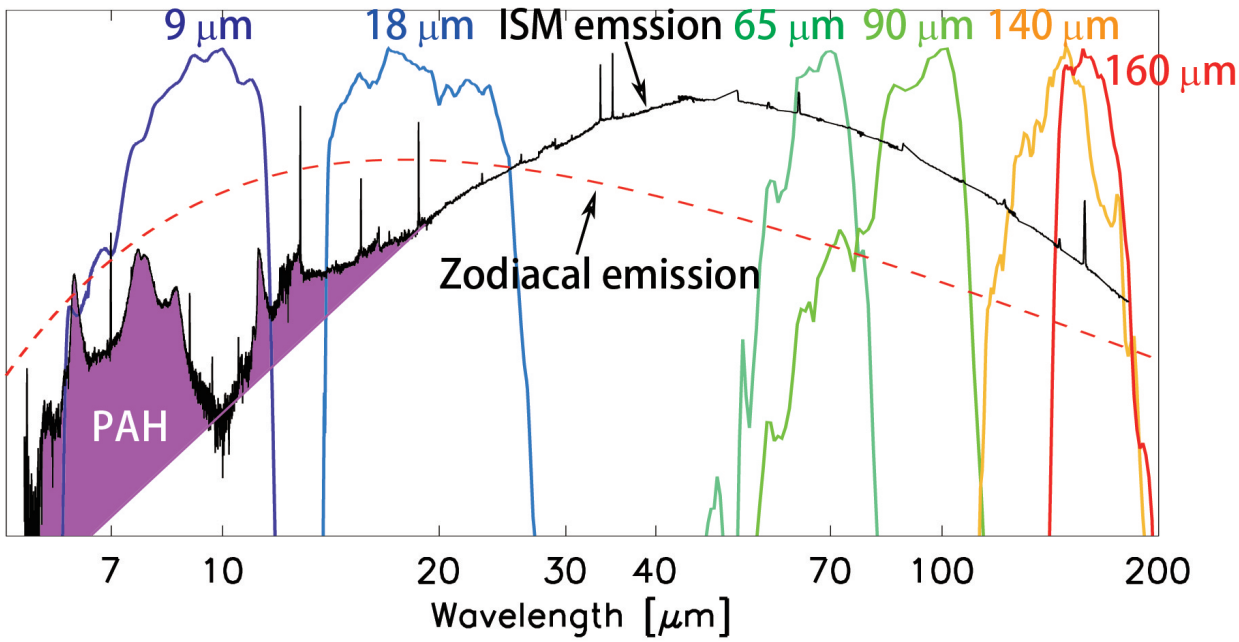

Figure 1.7 Relative spectral response curves of the *AKARI* 9, 18, 65, 90, 140, and 160 μm bands. A dashed curve represents the zodiacal emission spectrum (the blackbody radiation with temperature of 286 K). A black solid curve represents the spectrum of M 82, a typical starburst galaxy. The PAH features are painted over in magenta.

the all-sky spatial distribution of the zodiacal emission, especially in the mid-IR where the zodiacal emission peaks. Kelsall et al. (1998) removed the zodiacal emission from the DIRBE maps using their model (hereafter called the Kelsall model), which is considered to be one of standard IPD models. However, there is a significant residual component of the zodiacal emission in the DIRBE mid-IR maps as shown in Fig. 1.8. We therefore aim to improve the IPD cloud model based on the Kelsall model, using the *AKARI* mid-IR all-sky survey data, which have higher spatial resolution ($\sim 6''$) than the *COBE*/DIRBE ($\sim 0\overset{\circ}{.}7$) and the *IRAS* data ($\sim 4'$). In addition to the accurate modeling and discussion about the properties of IPD, we investigate whether or not the distribution of the zodiacal emission changed in the past 10–20 years, comparing the *AKARI* and the DIRBE data; the interval between the launches of *COBE* and *AKARI* is about 16 years.

Aside from the zodiacal emission study, the 9 μm map is crucial to investigate the all-sky distribution of polycyclic aromatic hydrocarbons (PAHs), while the 18 μm map is useful to trace hot dust grains, as shown in Fig. 1.7. The 9 μm map is the world-first all-sky PAH map with high spatial resolution. Therefore, it is also important to model the zodiacal emission accurately for studies of the Galactic interstellar medium (ISM). *AKARI* has revealed the spatial distribution and the spectral properties of PAHs in our Galaxy (e.g., Kaneda et al. 2012; Kondo et al. 2013) and nearby galaxies (e.g., Kaneda et al. 2010; Kondo et al. 2012a,b; Mori et al. 2012; Yamagishi et al.

2012) with both imaging and spectroscopic observations. The all-sky PAH map is expected to reveal a large-scale distribution and the chemical evolution of organic matter such as PAHs throughout our Galaxy.

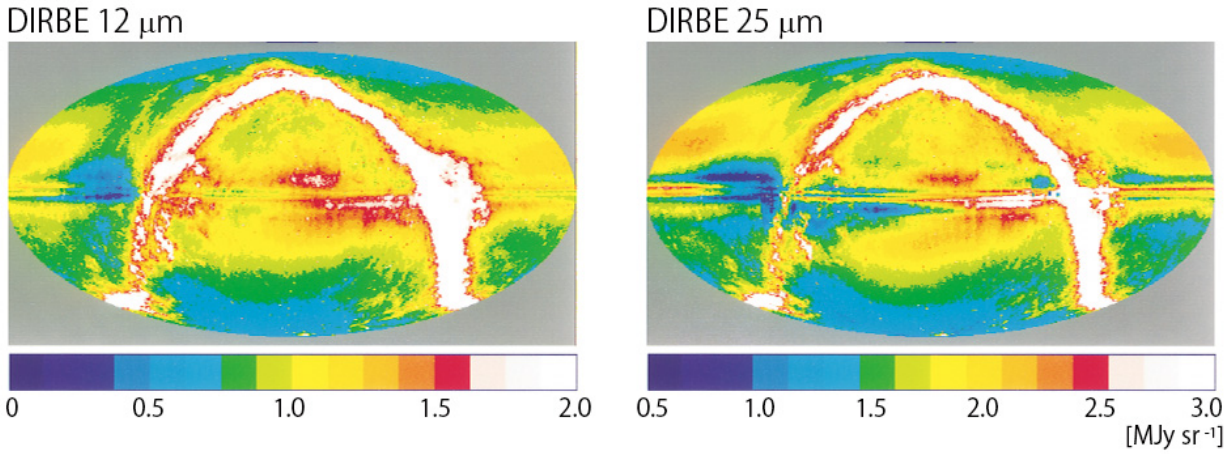

Figure 1.8 DIRBE 12 and 25 μm all-sky maps after subtraction of the zodiacal emission with the Kelsall model in the ecliptic coordinates (Kelsall et al. 1998).

Chapter 2

Observations and Data Reduction

2.1 *AKARI* Mid-IR All-Sky Survey

The mid-IR all-sky survey was conducted with the two photometric broad band filters centered at 9 μm (*S9W*) and 18 μm (*L18W*) of the MIR-S and MIR-L channels, respectively (Onaka et al. 2007; Ishihara et al. 2010). Table 2.1 shows the parameters for the mid-IR all-sky survey operation. *AKARI* revolved around the Earth in a sun-synchronous polar orbit. In the all-sky survey, the satellite scanned the sky along the circle of the solar elongation at approximately 90°. The MIR-S and MIR-L channels use 256×256 Si:As arrays with the pixel scales of $2\farcs34 \times 2\farcs34$ and $2\farcs51 \times 2\farcs39$, respectively.

Two detector rows out of 256 in the sensor array were used for the all-sky observations, and the two rows scanned the sky in a continuous and non-destructive readout mode (Ishihara et al. 2006, 2010). The independent observations with the two rows improve the reliability of the data quality. In the all-sky survey, four adjacent pixels were binned as virtual pixels whose sizes are $9\farcs36 \times 9\farcs36$ and $10\farcs4 \times 9\farcs36$ in the 9 and 18 μm bands, respectively. The virtual pixels are shifted by two pixels in the cross-scan direction between the two rows as shown in Fig. 2.1. Hence, the spatial resolution obtained in the all-sky survey observations is comparable with that obtained in the pointed observations, by combining the images obtained by the two rows even if the virtual pixel sizes are larger than the original full widths of half maximum (FWHM) of the point spread functions (PSF) of $5\farcs5$ and $5\farcs7$ in the 9 and 18 μm bands, respectively.

The array width is $10'$ in the cross-scan direction and the scan path is shifted from one to another by $4'$ at largest. Hence, the scan path overlaps at least $6'$ with the next scan path in 100 minutes. The orbit rotated about the axis of the Earth in one year, and hence the satellite covered the whole sky in half a year. *AKARI* observed the leading and the trailing directions of the Earth orbit alternately for every scan, because the solar elongation was fixed at 90°.

Table 2.1 Parameters for the mid-IR all-sky survey operation

Filter band	$S9W$	$L18W$
Wavelength (μm)	6.7–11.6	13.9–25.6
Isophotal wavelength (μm)	8.61	18.39
Effective bandwidth (μm)	4.10	9.97
Virtual pixel scale	$9''.36 \times 9''.36$	$10''.4 \times 9''.36$
FWHM of the PSF	$5''.5$	$5''.7$
Dark level (MJy sr^{-1})	1.68 ± 0.03	3.87 ± 0.06

These parameters are taken from Ishihara et al. (2010), except for the dark level.

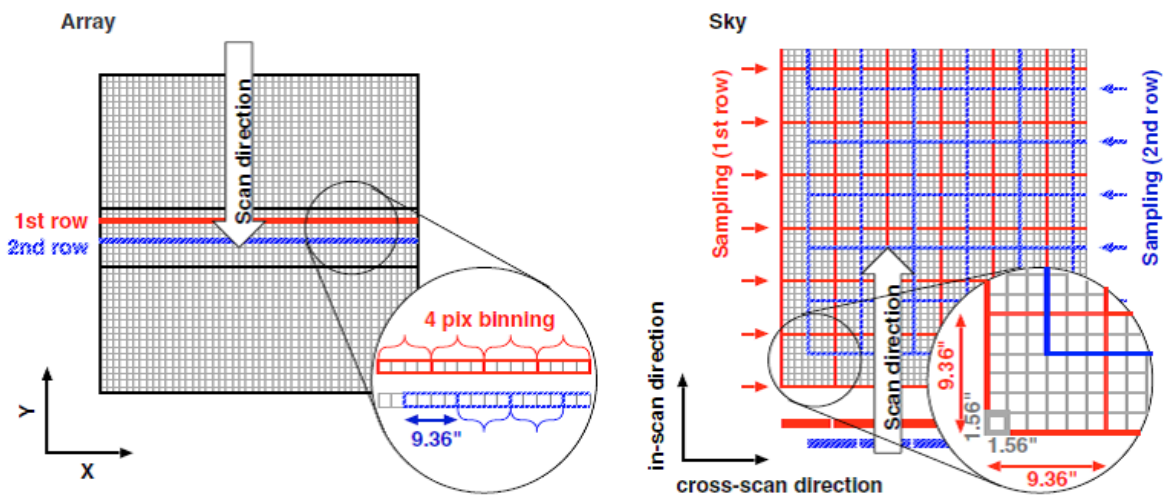

Figure 2.1 Left: schematic view of the detector array. Only the red and the blue rows out of 256 in the sensor array were used for the all-sky survey observations. Right: image reconstruction of the data obtained in the all-sky survey observations. This figure is taken from Ishihara et al. (2010).

The zero level of the surface brightness observed by *AKARI* is well calibrated for diffuse sources because of accurate dark current measurement. The dark current was measured with the cold shutter closed during the maneuver operation of the satellite. The dark current measurement took about 10 minutes and was performed about seven times per day on average. We evaluate the average and standard deviation of the dark level using all the measurements made during the mission period. The dark levels are 1.68 ± 0.03 MJy sr^{-1} and 3.87 ± 0.06 MJy sr^{-1} at 9 and 18 μm, respectively, and these values are subtracted from the data.

2.2 Production of the All-Sky Maps

We produced the mid-IR all-sky diffuse maps through the following processes. Those processes are summarized in Fig. 2.2. First, we made a unit image of $50' \times 10'$ from the raw data through the

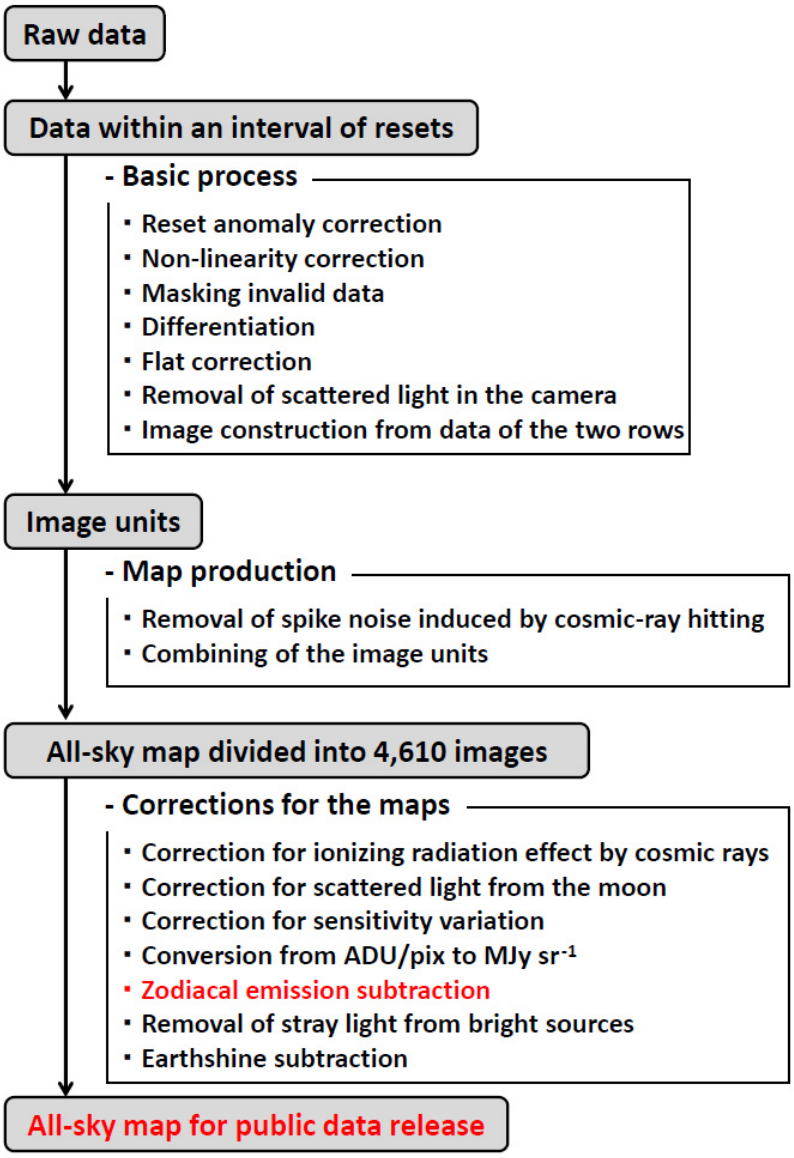

Figure 2.2 Outline of the mid-IR all-sky survey data processing.

basic process including corrections for reset anomaly and non-linearity of the detector. Secondly, we produced the maps by combining the unit images after removal of the spike noise induced by cosmic-ray hitting. Then, we corrected for the ionizing radiation effect by high-energy cosmic rays, and scattered light from the moon. After that, we converted the unit of the surface brightness from an analog-to-digital unit (ADU) to MJy sr^{-1}. For the public data release, we removed the zodiacal emission from the maps using the IPD cloud model which we had established in this study. After subtraction of the zodiacal emission, we removed the stray light from bright sources and the earthshine which is stray light from the Earth near the ecliptic poles.

2.2.1 Basic Process

In the basic process, we carried out corrections for instrumental artifacts such as reset anomaly and non linearity, and produced a unit image of $50' \times 10'$ from the raw data. Figure 2.3 shows an example of the processed data.

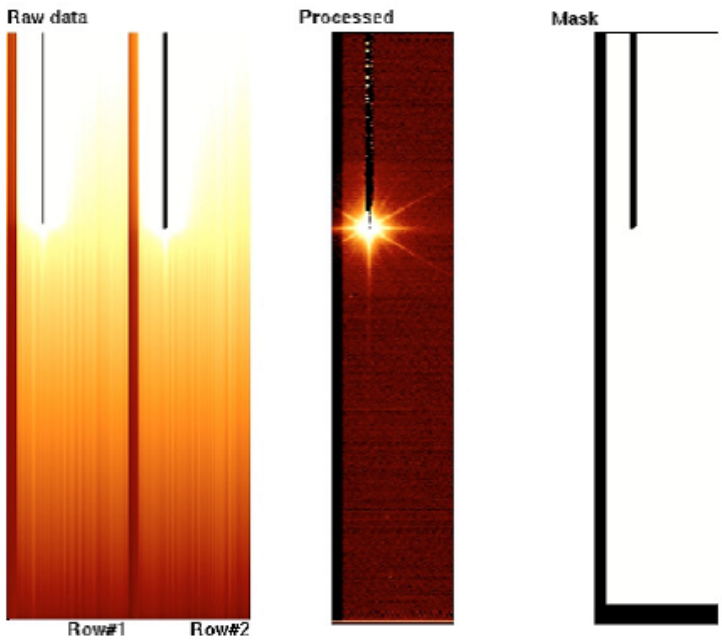

Figure 2.3 Example of the processed data (Ishihara et al. 2010). Left: raw data obtained from row#1 and row#2. Middle: processed data where the two rows are combined. Right: mask pattern for the processed data.

Corrections for reset anomaly and non linearity

We corrected the variations of the output level in a few seconds after the reset (reset anomaly) and the non linearity of the photo-response of the detector. Figure 2.4 shows a schematic image of the detector, whose behavior can be explained by a photodiode and a capacitor with two FETs as a readout circuit. The photoelectrons stacked in the capacitor flow out at the reset and thus the voltage applied to the FETs rapidly changes. As a result, the temperature of the FETs rises temporarily, and then, the temperature recovers slowly. We consider that the reset anomaly is explained by the drift of the offset level of the readout circuit because the offset level of the output of the detector depends on the temperature (Ishihara et al. 2003). On the other hand, the photoelectrons accumulate in the sensors by detection of IR photons with the detector. The response to the photons becomes non-linear with time from the resets due to the decrease in the effective quantum efficiency, because the bias voltage decreases with the accumulation of the photoelectrons. Figure 2.5 shows the effects of the reset anomaly and the non linearity on the observational data.

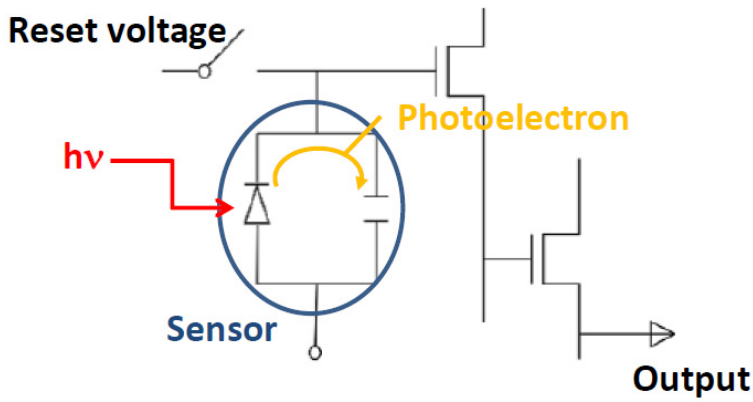

Figure 2.4 Schematic image of the detector circuit (one pixel).

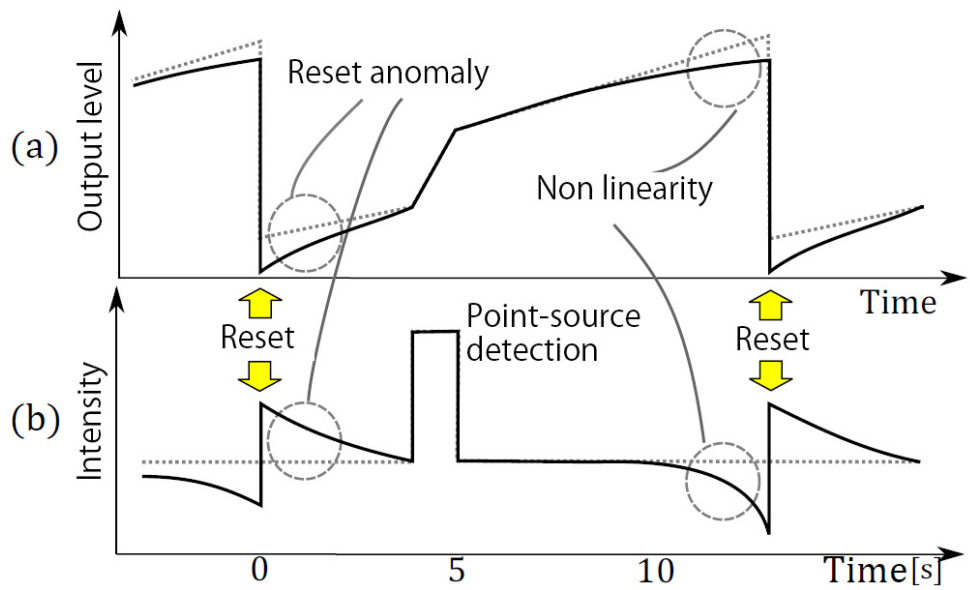

Figure 2.5 Schematic images of the effects of the reset anomaly and the non linearity on the observational data (Amatsutsu 2015). (a) Time variation of the amount of electrons stacked in the capacitor. (b) Time variation of the intensity of the incident light which are obtained by differentiating the amount of the stacked electrons by time. Solid and dotted curves represent the observational data and the corrected data, respectively.

The reset anomaly depends on the amount of the photoelectrons which flowed out at the previous reset, $e_{\rm rst}$, and the time from the previous reset, t. The non linearity depends on the amount of the stacked electrons. We show the relation between the observed output level, $I_{\rm obs}(t)$, and the real output level without the effects of the reset anomaly and the non linearity, $I_{\rm real}(t)$, as

$$I_{\rm obs}(t) = (I_{\rm real}(t) - O(t, e_{\rm rst})) \times L(I_{\rm obs}(t)), \tag{2.1}$$

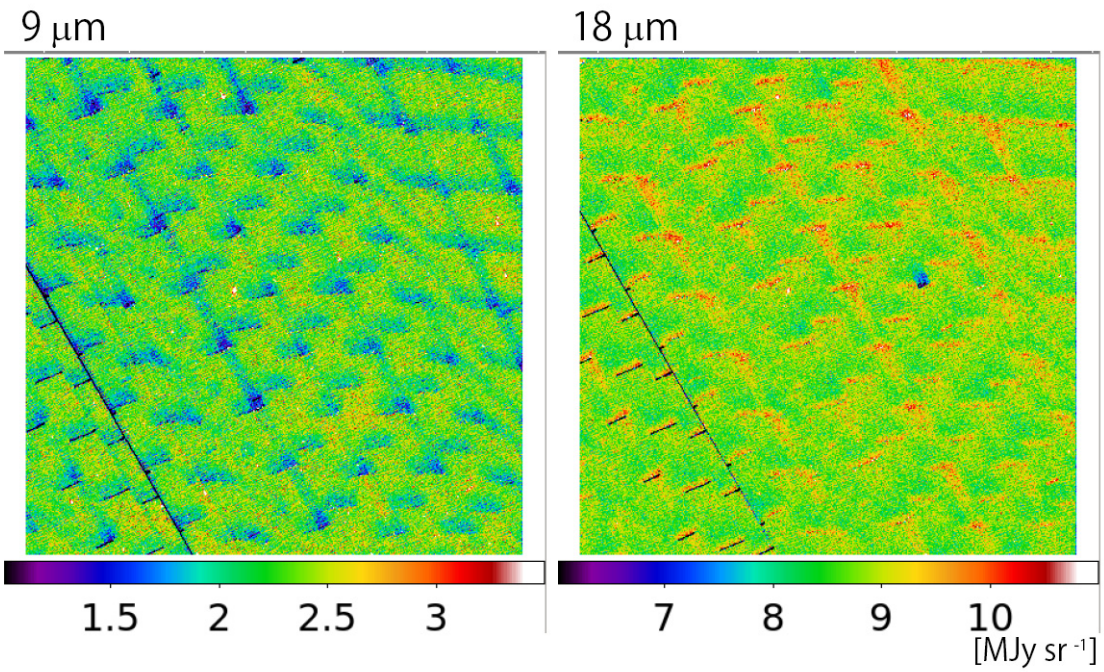

Figure 2.6 *AKARI* 9 and 18 μm images for an area of $6^\circ \times 6^\circ$ with the center at $(\alpha_{\rm J2000}, \delta_{\rm J2000}) = (169^\circ, -33^\circ)$ (Amatsutsu 2015). The corrections for the reset anomaly and the non linearity established by Ishihara et al. (2010) are adopted to the data.

where $O(t, e_{\rm res})$ is the offset level variation due to the reset anomaly and $L(I_{\rm obs}(t))$ is the photo-response, which varies with the amount of the stacked electrons due to the non linearity. Considering that the two FETs are cooled by heat conduction of the substrate, we assumed the offset level variation, $O(t, e_{\rm rst})$, as

$$O(t, e_{\rm rst}) = C_1(e_{\rm rst}) \exp\left(-t/C_2(e_{\rm rst})\right) + C_3(e_{\rm rst}) \exp\left(-t/C_4(e_{\rm rst})\right), \tag{2.2}$$

where C_1 to C_4 are functions of the amount of the outflowed photoelectrons, $e_{\rm rst}$.

Although Ishihara et al. (2010) previously established the corrections for the reset anomaly and the non linearity from the response of the detector under the constant illuminating source in a laboratory test, the artifacts remain in the all-sky maps as shown in Fig. 2.6, whose patterns are repeated every $50'$ corresponding to the reset interval.

We therefore derived more accurate corrections using the observational data whose brightness range is wider than the laboratory data. We utilized the zodiacal emission for deriving the corrections because of the two following reasons; the first reason is that the spatial scale of the zodiacal emission is relatively large, which means that the brightness variation is small between the resets. The second one is that the zodiacal emission includes the surface brightness with a wide dynamic

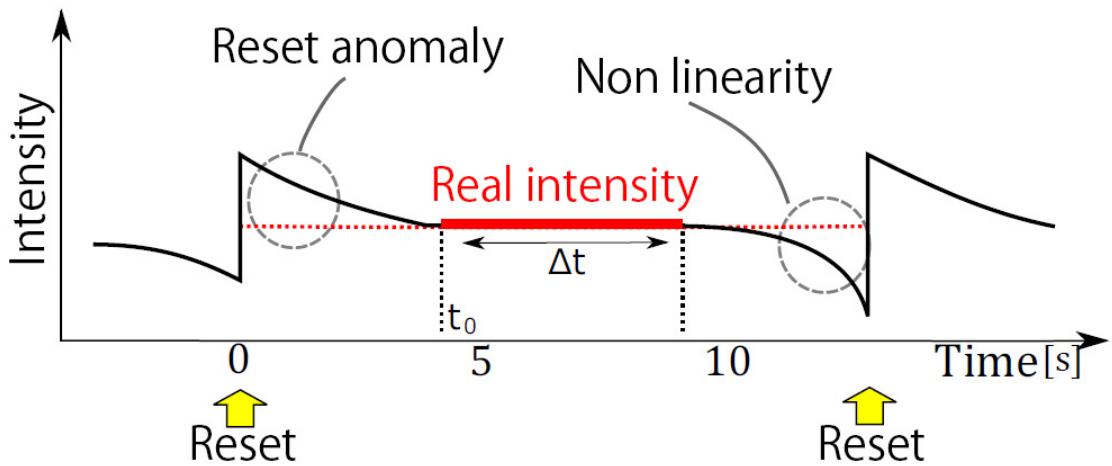

Figure 2.7 Schematic image for showing the method of the estimation of the constant real intensity of the incident light, which are represented by a red line (Amatsutsu 2015). The horizontal and the vertical axes represent the time and the intensity of the incident light, respectively. The constant real intensity is estimated from the data taken at time from t_0 to $t_0 + \Delta t$.

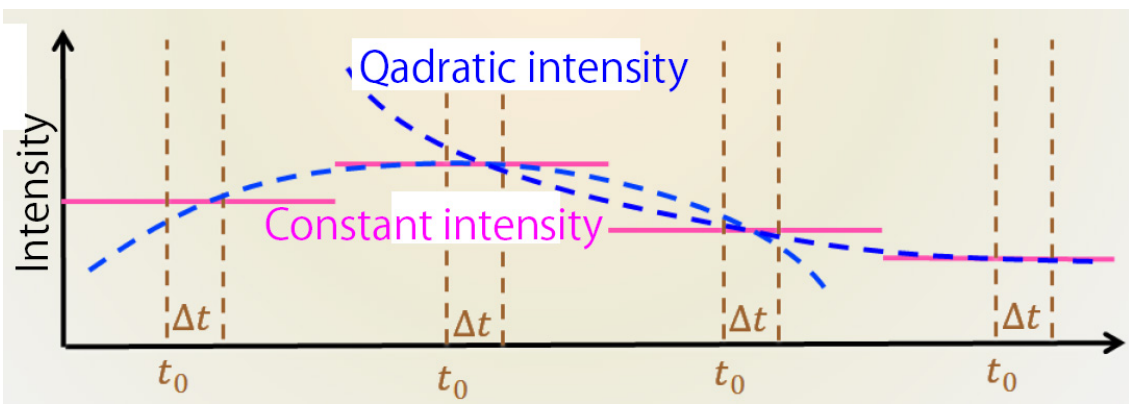

Figure 2.8 Schematic image for showing the method of the estimation of the quadratic real intensity of the incident light, which are represented by dashed blue curves (Amatsutsu 2015). The horizontal and the vertical axes represent the time and the intensity of the incident light, respectively. Magenta lines represent the constant real intensity of the incident light.

range. We selected 94,373 data points for each of analyses in the 9 and 18 μm bands. In order to evaluate the effects of the reset anomaly and the non linearity, we estimated the time-differential real output level (the real intensity of the incident light), $dI_{\rm real}(t)/dt$, from the data where these effects are small. We estimated the lower limit of the elapsed time from the previous reset where the reset anomaly is negligible and estimated the upper limit of the amount of the stacked electrons where the non linearity is negligible in each dataset between the two adjacent resets. Then, we obtained the constant real intensity of the incident light from the data where we consider that there are no effects of the reset anomaly and the non linearity as shown in Fig. 2.7. Next, we fitted

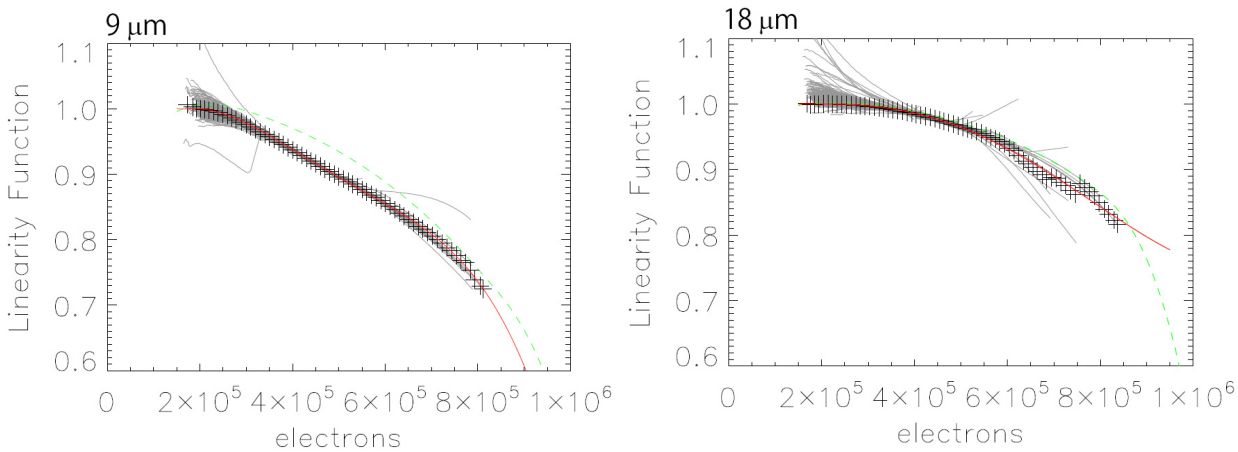

Figure 2.9 Correction functions for the non linearity, $L(I_{\rm obs})$, obtained by the fitting (red curves) at 9 μm (left) and 18 μm (right) (Amatsutsu 2015). The horizontal and the vertical axes indicate the amount of the stacked electrons, $I_{\rm obs}$, and the ratios of the observed to real output level, $I_{\rm obs}/I_{\rm real}$, respectively. Gray curves represent the observational data points and cross points represent the 10,000-electron median values of $I_{\rm obs}/I_{\rm real}$. Green dashed curves represent the previous correction functions established by Ishihara et al. (2010).

the three adjacent values of the constant real intensity with a quadratic function as shown in Fig. 2.8. As can be seen in Fig. 2.8, the real intensity represented by the quadratic function has two values at the same time. We did not use the data if the two values have difference larger than 3%. Eventually, we used 92,120 and 92,180 data points for the corrections in the 9 and 18 μm bands, respectively. We integrated the quadratic real intensity with respect to the time elapsed from the previous reset and thus obtained the real output level, $I_{\rm real}(t)$.

We derived the correction function for the reset anomaly and that for the non linearity from the relation between $I_{\rm obs}(t)$ and $I_{\rm real}(t)$ (equation (2.1)). In the regions where the reset anomaly is negligible, the correction function for the non linearity, $L(I_{\rm obs}(t))$ is represented as

$$L(I_{\rm obs}(t)) = \frac{I_{\rm obs}(t)}{I_{\rm real}(t)}. \tag{2.3}$$

We defined the correction function for the non linearity, $L(I_{\rm obs})$, as

$$L(I_{\rm obs}) = 1 - c_1(I_{\rm obs} - I_0)^2 - c_2(I_{\rm obs} - I_0)^3 - c_3(I_{\rm obs} - I_0)^4, \tag{2.4}$$

where I_0 is the amount of the stacked electrons at the reset. We calculated the median values of $I_{\rm obs}/I_{\rm real}$ every 10,000 stacked electrons. Then, we fitted the median values with the correction function (equation (2.4)) and thus obtained the fitting parameters c_1 to c_3, as shown in Fig. 2.9.

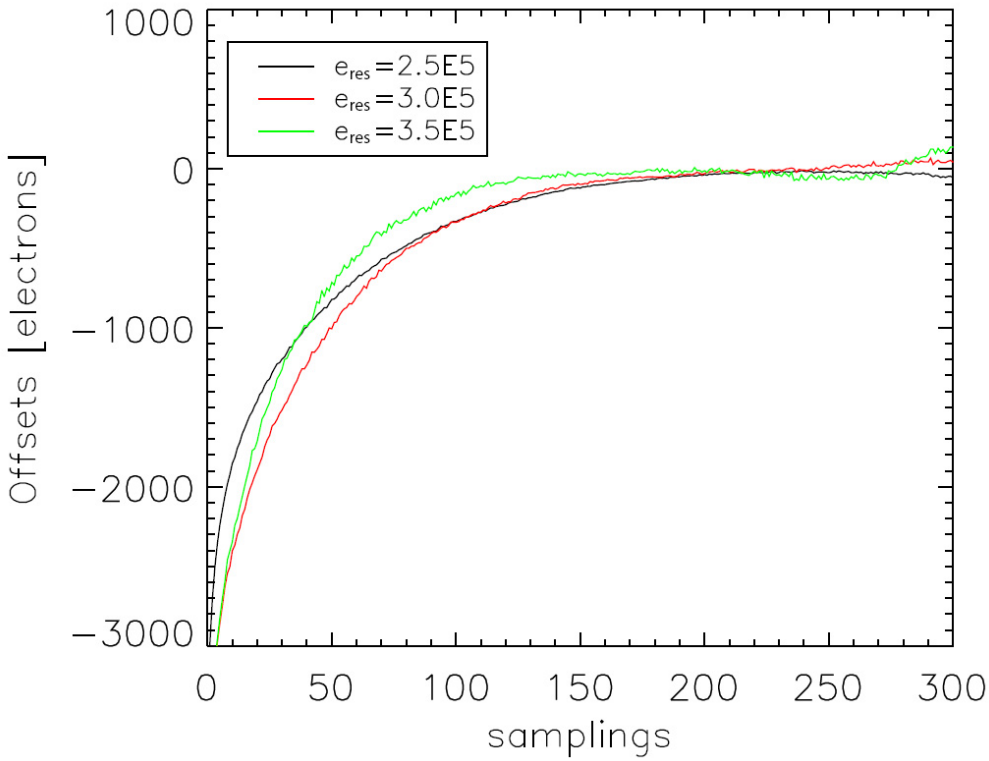

Figure 2.10 Time variations of the offset levels, $O(t, e_{\rm rst})$, in the 18 μm band for the amount of the outflowed photoelectrons, $e_{\rm rst}$, of 2.5×10^5, 3.0×10^5, and 3.5×10^5, which are represented by black, red, and green curves, respectively (Amatsutsu 2015).

Then, the correction function for the reset anomaly is represented as

$$O(t, e_{\rm rst}) = \frac{I_{\rm obs}(t, e_{\rm rst})}{L(I_{\rm obs})} - I_{\rm real}(t). \tag{2.5}$$

We fitted $O(t, e_{\rm rst})$ in equation (2.5) with equation (2.2) and thus obtained the correction function, $O(t, e_{\rm rst})$. Figure 2.10 shows the offset level variations due to the reset anomaly in the 18 μm band for the different $e_{\rm rst}$ values of $e_{\rm rst} = 2.5 \times 10^5$, 3.0×10^5, and 3.5×10^5. As can be seen in this figure, both coefficients (C_1 and C_3) and time constants (C_2 and C_4) in the correction function (equation (2.2)) depend on $e_{\rm rst}$. We first obtained C_1 to C_4 as constant parameters in each $e_{\rm rst}$ value, and then we fitted C_1 to C_4 as a function of $e_{\rm rst}$.

We compare the data corrected in the present method with those corrected in the previous method. Figure 2.11 shows the 9 μm image of the data corrected in the present method for both reset anomaly and non linearity, that of the data corrected in the present method only for the reset anomaly, and that of the data corrected in the present method only for the non linearity. Comparing these images, it is clear that we have succeeded in reducing the levels of the artifacts caused by the

reset anomaly and the non linearity, and thus in improving the corrections.

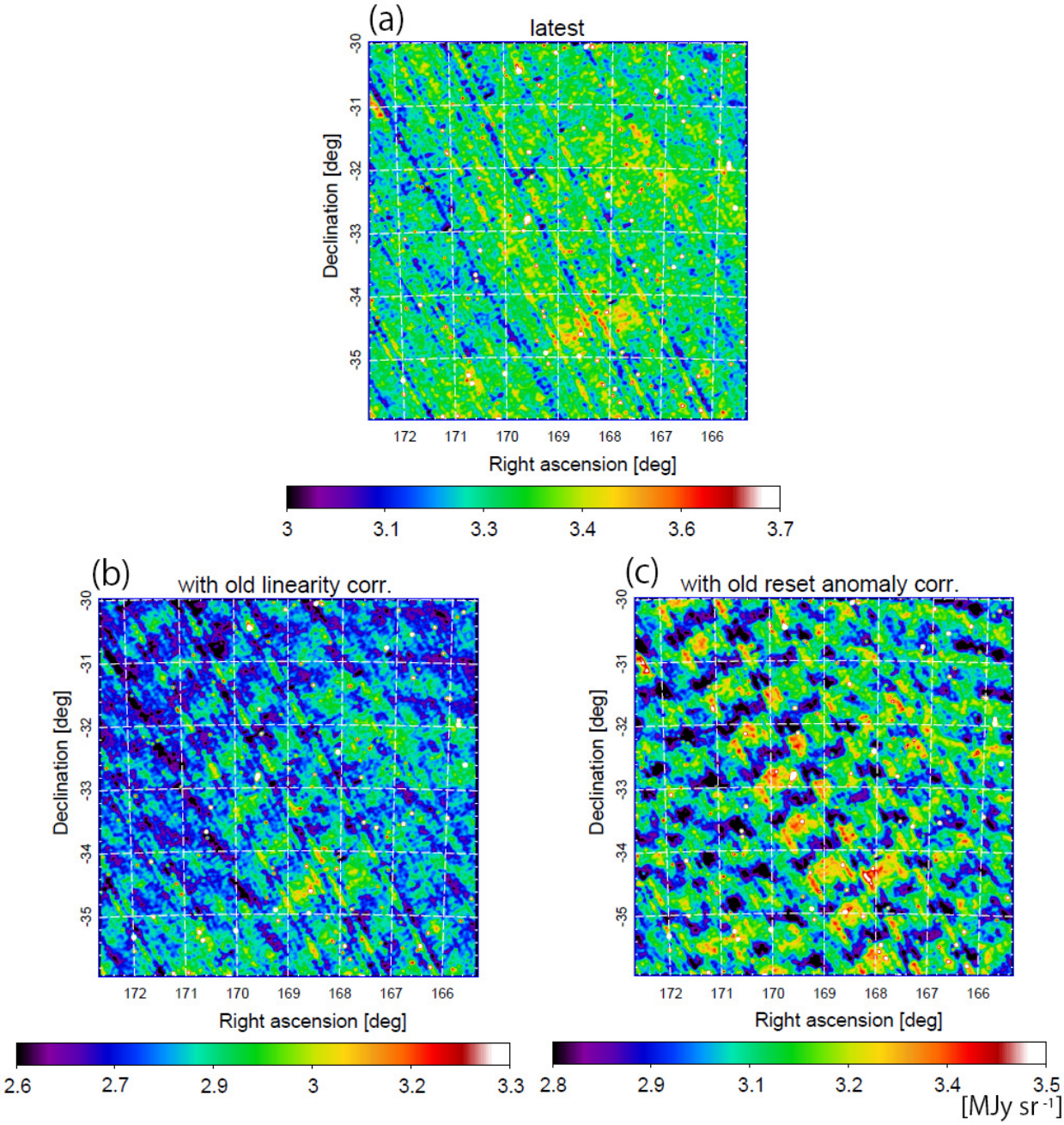

Figure 2.11 *AKARI* 9 μm images in the same region as those in Fig. 2.6. Panels (a), (b), and (c) show the image of the data corrected in the present method for both reset anomaly and non linearity, that of the data corrected in the present method only for the reset anomaly, and that of the data corrected in the present method only for the non linearity, respectively. The color levels are different but the dynamic range is same among these panels.

Masking invalid data

In order not to use invalid data, we masked the following regions:

(1) all the pixels during the resets and the periods heavily affected by the reset anomaly,

(2) saturated pixels from the moment of the saturation to the next reset,

(3) the pixels under the slit masks for the diffuse spectroscopy.

The right panel of Fig. 2.3 shows an example of the mask pattern.

Differentiation

The signal at the observed celestial position was obtained by differentiating the amount of stacked photoelectrons between the resets as

$$S^{(1)}(i,t) = I_{\rm real}(i, t+\Delta t) - I_{\rm real}(i,t), \tag{2.6}$$

where i is the pixel number and Δt is the time step of 44 ms corresponding to the sampling rate.

Flat correction

We corrected the difference in the pixel-by-pixel sensitivities. We obtained the flat-corrected signal, $S^{(2)}(i,t)$, by dividing the differential signal, $S^{(1)}(i,t)$, by the flat function, $F(i)$, which represents the difference in the pixel-by-pixel sensitivities, as

$$S^{(2)}(i,t) = S^{(1)}(i,t)/F(i). \tag{2.7}$$

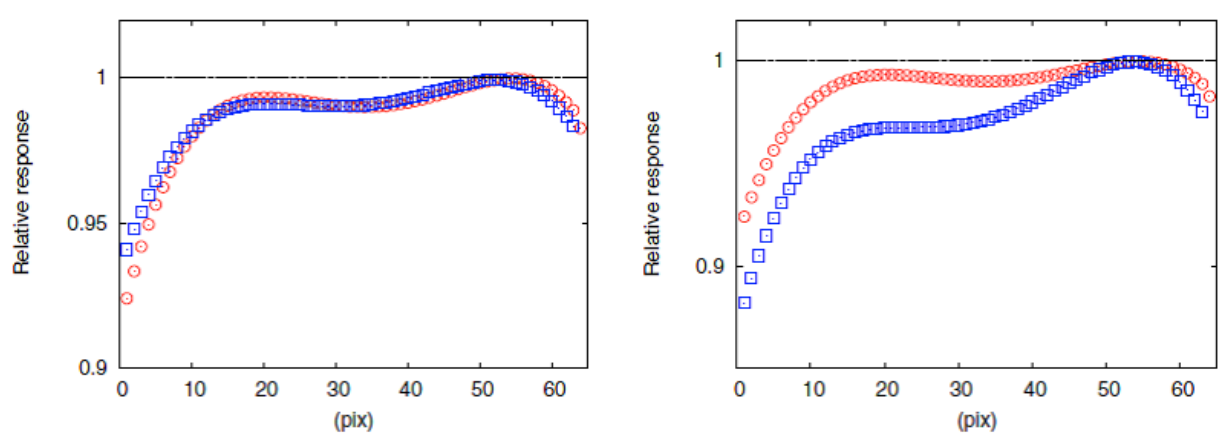

Figure 2.12 Left and Right panels show the flat functions for the one-dimensional arrays in the 9 and 18 μm bands, respectively (Ishihara et al. 2010). The red open circles and the blue open squares represent row#1 and row#2, respectively, in both panels.

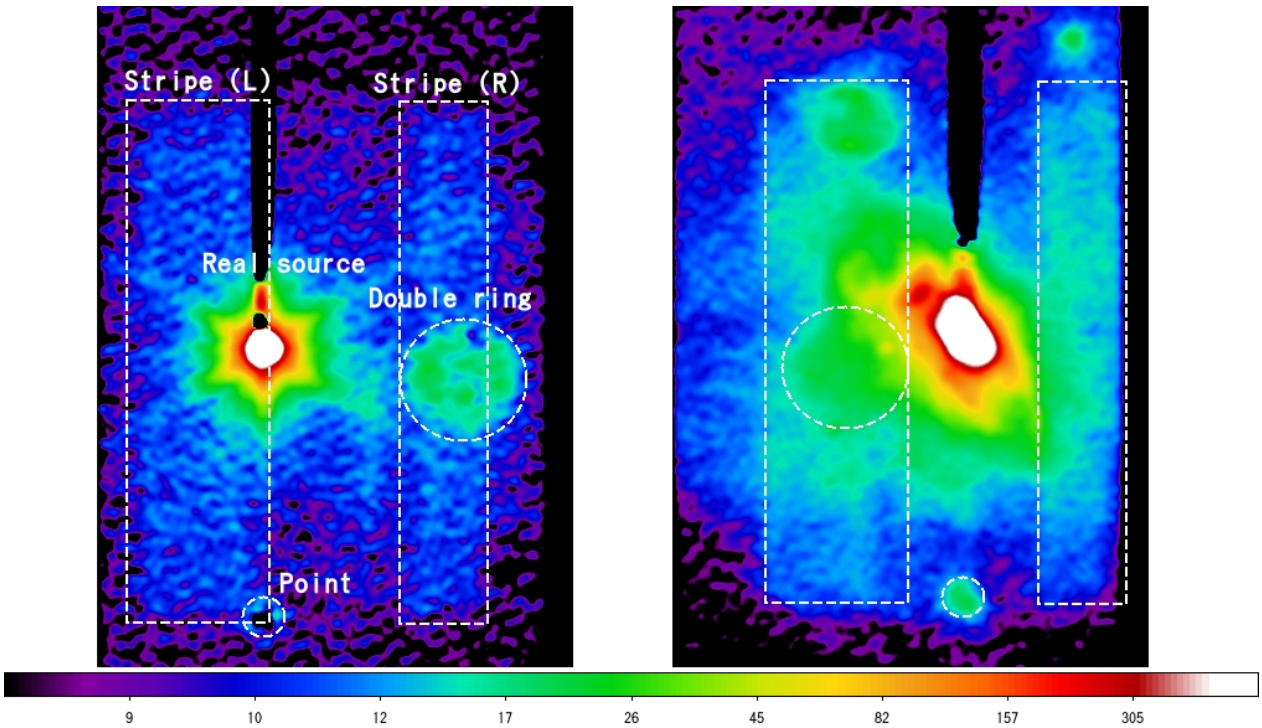

Figure 2.13 Examples of the pattern of the scattered light in the camera at 18 μm. The sizes of these images are $15' \times 10'$. The left and the right panels show the scattered light patterns due to a point source and a bright diffuse object, respectively. There are point-, ring-, and stripe-like structures.

We evaluated the flat function, $F(i)$, from multiple detections of the same stars on different pixels. The flat function, $F(i)$, was normalized to the value in the pixel which has the highest sensitivity. Figure 2.12 shows the flat functions for both rows (row#1 and row#2) in the 9 and 18 μm bands.

Removal of scattered light in the camera

We removed the scattered light in the camera, which came into the detector through unexpected paths. The scattered light behaves as the offset. Figure 2.13 shows the scattered light pattern. We defined the scattered light pattern as a function of an incident light intensity, $I_{\rm bg}$. We subtracted the scattered light pattern, $SC(i, I_{\rm bg})$, from the signal after the correction for flat fielding, $S^{(2)}(i,t)$, as

$$S^{(3)}(i,t) = S^{(2)}(i,t) - SC(i, I_{\rm bg}). \tag{2.8}$$

Image construction from data of the two rows

We constructed a single image with a pixel scale of $1\farcs56$, combining the data from row#1 and row#2. The middle panel of Fig. 2.3 shows an example of the data thus processed. Using two data

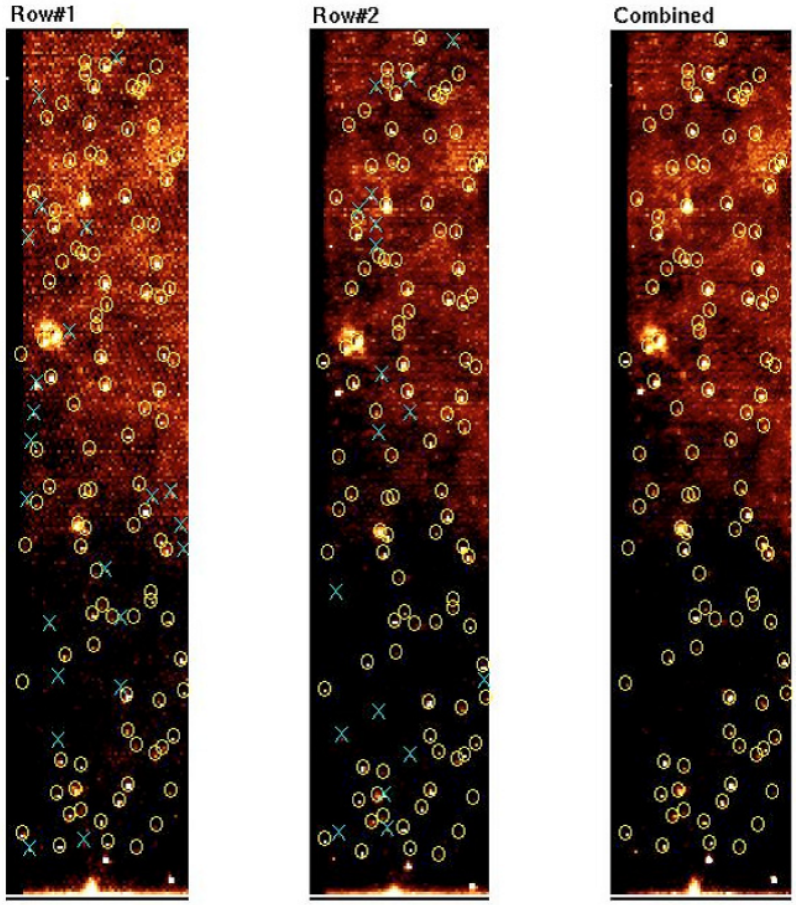

Figure 2.14 Example of the detections of point sources (Ishihara et al. 2010). The left, middle, and right images are obtained from row#1, row#2, and the combined data, respectively. The crosses represent point sources detected in only one row. The circles represent point sources detected in both rows with similar fluxes.

sets enables us to reject the effect of cosmic-ray hitting as mentioned below, and to achieve higher signal-to-noise (S/N) ratios than those with a single row data.

2.2.2 Map Production

We produced the maps by combining the processed images of $50' \times 10'$ after removal of spike noise.

Removal of spike noise induced by cosmic-ray hitting

There is spike noise in the basic-processed data because cosmic rays hit the detector. We therefore aimed to remove the spike noise. First, we extracted point sources from the two row images with 3σ threshold using the Source Extractor (Bertin & Arnouts 1996). Next, we cross-identified point sources extracted from the images between row#1 and row#2 at the detected

position. If a detected point source is a celestial source, it should be detected in both rows in the same pixel number i with similar fluxes. On the other hand, if a detected point source is spike noise, it should be detected in only one row. We therefore judged a pair of detections at the same celestial position with similar fluxes of $0.1 < F_{\mathrm{row\#1}}/F_{\mathrm{row\#2}} < 10$ to be a celestial source. Finally, we removed the other point sources as the spike noise as shown in Fig. 2.14.

Combining of the unit images

We combined the images of $50' \times 10'$ and thus produced the maps. For the data management and the public data release, the all-sky maps are maintained in the form of the total 4,610 tile images of $3\overset{\circ}{.}2 \times 3\overset{\circ}{.}2$ at 3° interval in the Galactic coordinates in each photometric band. Since *AKARI* observed the whole sky in half a year and the all-sky survey observation was carried out for about one year and three months, there are two or three tiles of the same celestial region. We divide the mission period into the three seasons every half a year: Phase 1 (May 2006–November 2006), Phase 2a (November 2006–May 2007), and Phase 2b (May 2007–August 2007).

2.2.3 Corrections for the Maps

First, we corrected for the ionizing radiation effects by high-energy cosmic rays (Mouri et al. 2011; Mouri 2012; Amatsutsu 2015) and scattered light from the moon. Secondly, we converted the unit of the surface brightness from ADU to MJy sr^{-1}. Then, we removed the zodiacal emission based on the IPD cloud model which we had established in this study. The surface brightnesses of the zodiacal emission are different among the seasons even if the satellite observed the same celestial position. On the other hand, the surface brightnesses of the large-scale diffuse celestial objects other than the zodiacal emission should not vary among the seasons. We therefore removed the extended artifacts whose positions or shapes are different among the seasons, such as the stray light from bright sources and the earthshine, comparing the different seasonal maps after subtraction of the zodiacal emission.

Correction for ionizing radiation effects by high-energy cosmic rays

We found that the surface brightnesses are systematically higher in the regions where the observations were carried out under the heavy bombardment of high-energy ionizing cosmic rays on the detector as shown in Fig. 2.15, even after the spike noise is removed. In particular, a large amount of cosmic rays hit the detector when *AKARI* passed through the South Atlantic Anomaly (SAA), which is the local geomagnetic anomaly structure over Brazil. In this region, an altitude of the inner Van Allen radiation belt is lower ($\sim$300 km) than those of the other regions ($\sim$1,000 km). The amount of radiation is shown in Fig. 2.16, overlaid on the world map.

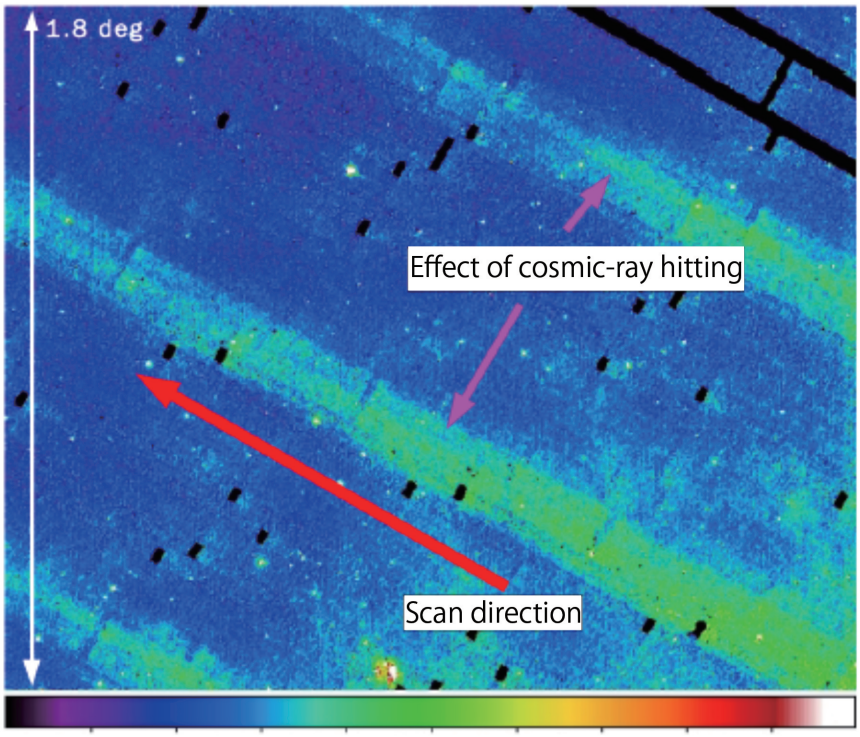

Figure 2.15 Example of the image affected by the ionizing radiation (Mouri 2012). In the regions affected by the ionizing radiation, the surface brightnesses are systematically higher than those of the other regions. These structures are seen along the scan direction indicated by a red arrow.

AKARI observed the same celestial region twice or three times in different seasons. Hence, if the region observed in one season is affected by the ionizing radiation, the region observed in the other seasons is not affected. We therefore aimed to quantitatively find the relation between the ionizing radiation effect and the hitting rate of cosmic rays, comparing the data affected by the ionizing radiation with those not affected in the same celestial region.

As a result, we found that the ionizing radiation effect can be explained by the changes in the offset of detector output against the hitting rate of cosmic rays (Mouri et al. 2011; Mouri 2012). Figure 2.17 shows the relation between the output offset level and the hitting rate of cosmic rays. Mouri et al. (2011) and Mouri (2012) fitted the relation with a line and obtained the slope, which were used for the correction function, as shown in the green lines in Fig. 2.17. As a result, they succeeded in removing the artifacts caused by the ionizing radiation effects, as shown in Fig. 2.18 where the stripe-like structures appeared in panel (a) are removed from the map in panel (b). Recently, Amatsutsu (2015) found that the linear function was not enough to correct the data where the surface brightness is relatively low of a few MJy sr^{-1} as shown in Fig. 2.19, and that a quadratic function better explains the behavior of the offset level than the linear function. Therefore, we newly

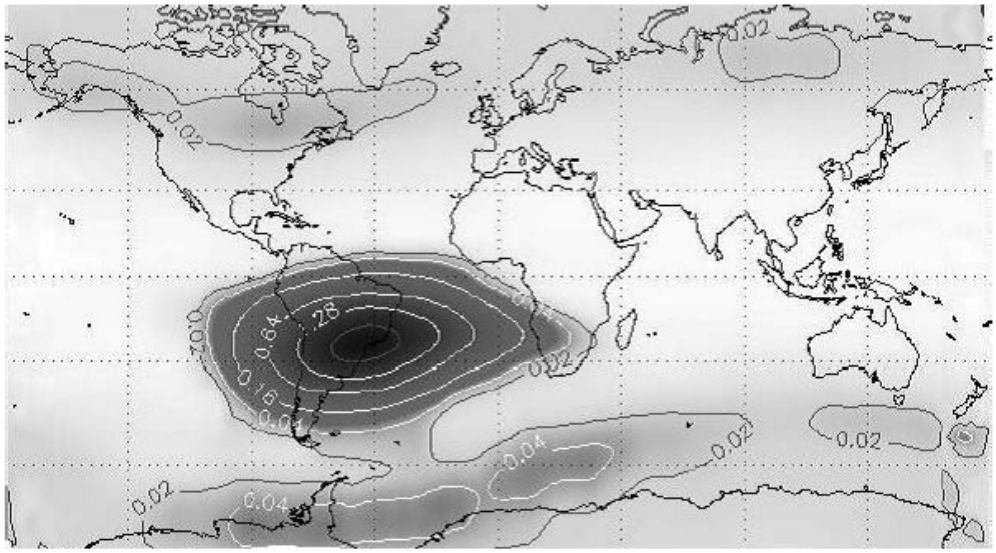

Figure 2.16 Amount of radiation is overlaid on the world map (Mouri 2012).

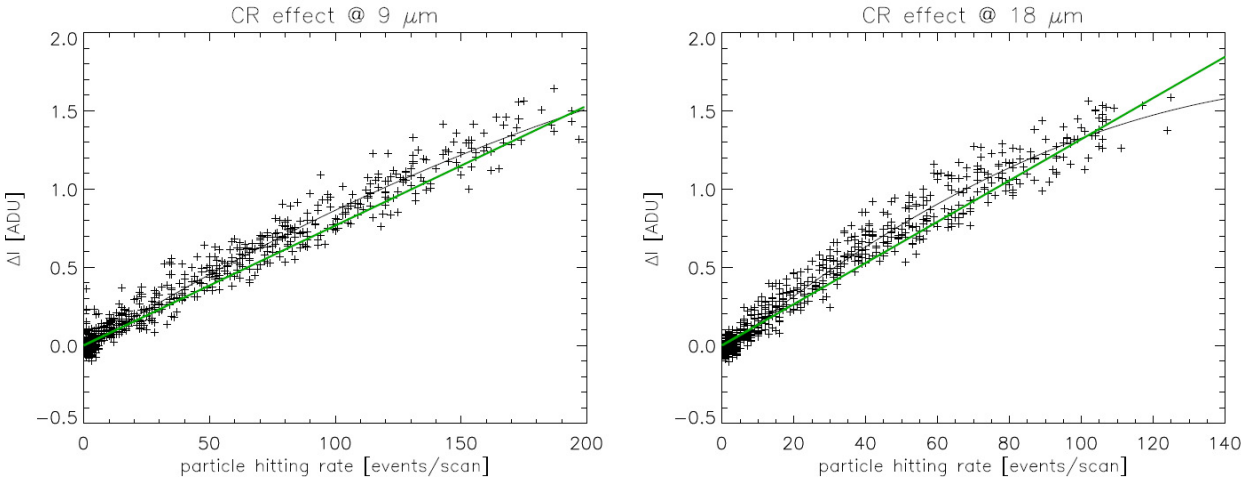

Figure 2.17 Correlation plots between the output offset level and the hitting rate of cosmic rays at 9 μm (left) and 18 μm (right) (Amatsutsu 2015). Black curves represent the best-fit result of quadratic fitting. Green lines represent the best-fit result of linear fitting previously obtained by Mouri et al. (2011) and Mouri (2012).

obtained the correction function by the quadratic fitting as shown in the black curves in Fig. 2.17. Figure 2.20 shows the result of the new correction for the ionizing radiation effect. By comparing Figs. 2.19 with 2.20, it is clear that we have succeeded in reducing the artifact levels through the improvement of the correction.

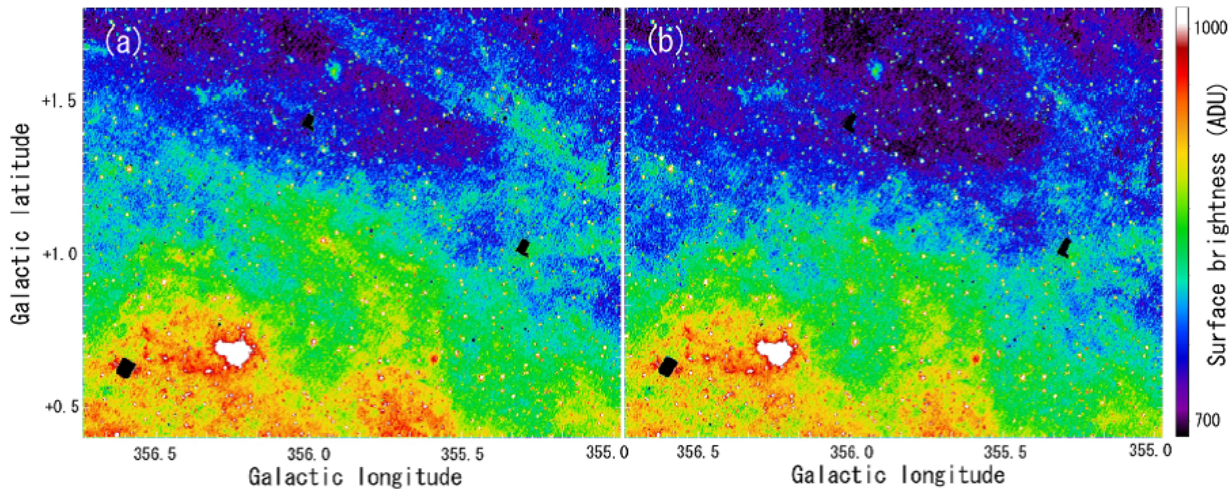

Figure 2.18 *AKARI* 18 μm map near the Galactic center (Mouri et al. 2011; Mouri 2012). (a) Image including the regions of the data taken from the observations under the ionizing radiation effect. (b) Image after the formerly-established correction for the ionizing radiation effect in the same region as panel (a).

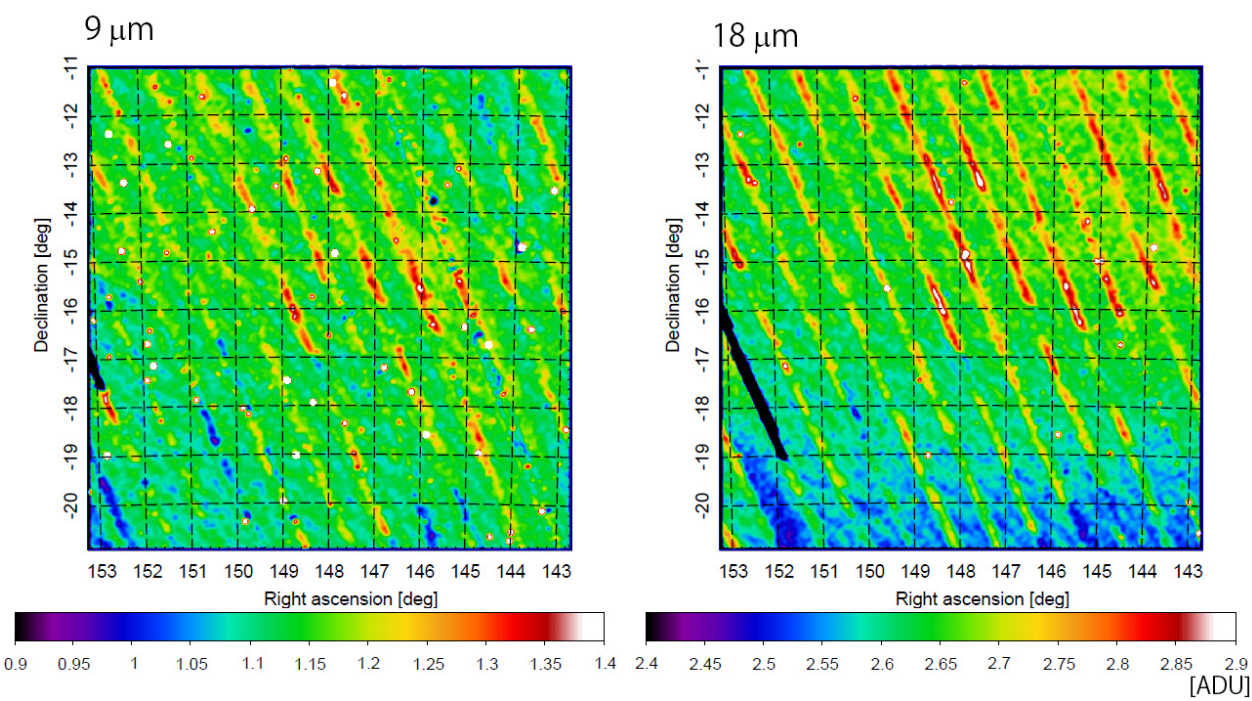

Figure 2.19 *AKARI* 9 and 18 μm images after the formerly-established correction (Mouri et al. 2011; Mouri 2012) for the ionizing radiation effect for an area of $10^\circ \times 10^\circ$ with the center at $(\alpha_{\rm J2000}, \delta_{2000}) = (148^\circ, -16^\circ)$.

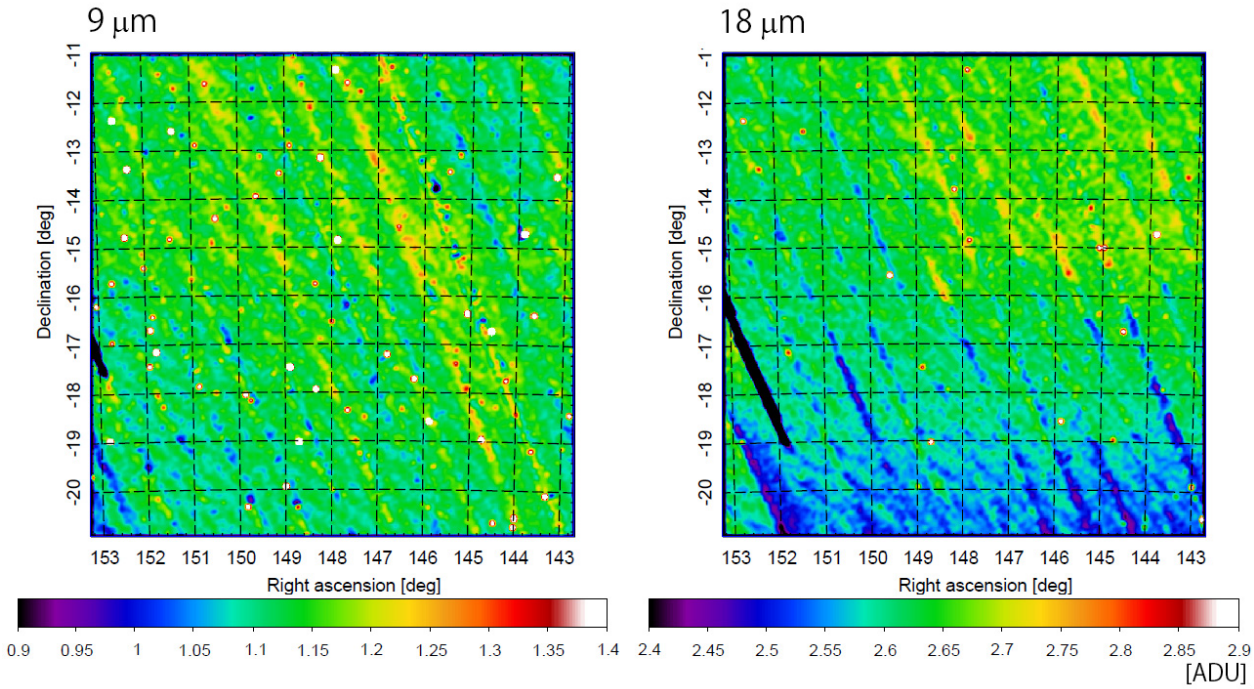

Figure 2.20 *AKARI* 9 and 18 μm images after the newly-established correction (Amatsutsu 2015) for the ionizing radiation effect for the same area as the images in Fig. 2.19.

Correction for scattered light from the moon

The moon light comes into the telescope of *AKARI* from outside the field of view. Figure 2.21 shows the 9 μm map in the region of a $40^\circ \times 12^\circ$ area, which is affected by the scattered light from the moon. In Fig. 2.21(a), the regions of the lunar elongations lower than 17° are masked to avoid the effect of the scattered light from the moon. However, the effect appears even on the outside of the masked regions. We therefore corrected the effect in the regions of the lunar elongations higher than 17° by more precisely estimating the distribution of the scattered light from the moon against the moon position in order not to increase the data which are not utilized any further.

Figure 2.22(a) shows the template map of the scattered light from the moon, which is made from the ten datasets affected by the scattered light. The map has an area of $80^\circ \times 80^\circ$ in the detector coordinates centered at the position of the moon. In this map, there are spider-like structures, which are scattered light produced by the truss structures supporting the secondary mirror. We therefore masked the spider-like structures in addition to the regions of the lunar elongation lower than 17° as shown in Fig. 2.22(b). Figure 2.21(b) shows the result of the correction for the scattered light from the moon by utilizing the template map, where the scattered light shown in Fig. 2.21(a) is successfully removed.

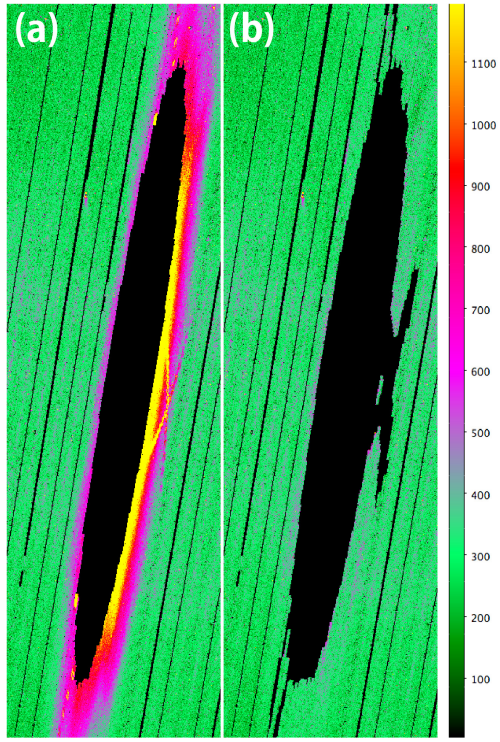

Figure 2.21 (a) Image of the region affected by the scattered light from the moon, for an area of $40^\circ \times 12^\circ$ with the center at $(\alpha_{\rm J2000}, \delta_{\rm J2000}) = (19^{\rm h}36^{\rm m}, -26^\circ)$, after masking the regions of the lunar elongations lower than 17° in the 9 μm band. (b) Same as panel (a), but the scattered light from the moon is removed from the map and the spider-like structures are masked by utilizing the template map shown in Fig. 2.22(b).

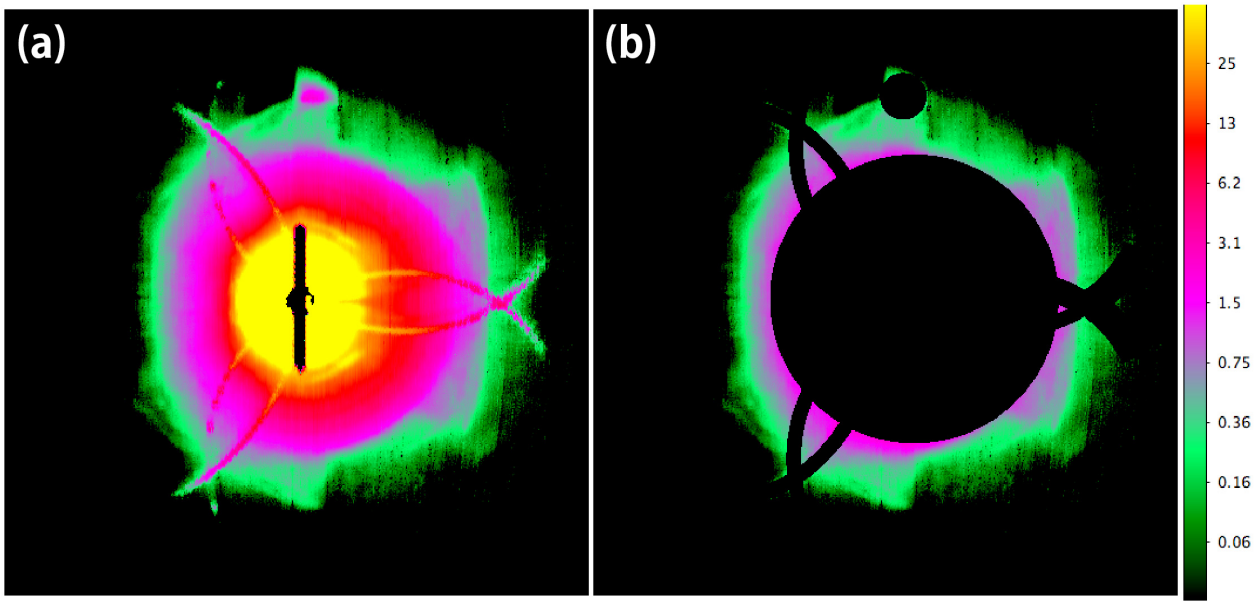

Figure 2.22 (a) Template map of the scattered light from the moon, for an area of $80^\circ \times 80^\circ$ in the detector coordinates centered at the position of the moon in the 9 μm map. (b) Same as panel (a), but the regions of the lunar elongations lower than 17° and the regions affected by the spider-like structures are masked.

Correction for sensitivity variation in the 18 μm band

We found that the sensitivity in the 18 μm band decreased with time during half a year after launch. In order to quantitatively estimate the variation, we measured the fluxes of the same point sources observed in different seasons. We selected the point sources which are not variable stars with S/N $\geq$ 40. Figure 2.23 shows the time variation of the fluxes of the point sources normalized by the mean fluxes of those observed at Phase 2b. We calculated the mean values of the normalized fluxes every 15 days, which are represented by asterisks in Fig. 2.23. We fitted the relation between the mean normalized flux and the time with an exponential function, as represented by the red curve in Fig. 2.23. We adopted this curve to correct for the relative sensitivity variation. As can be seen in this figure, the sensitivity varied by ~9% for about one year. We have not identified the cause of the sensitivity variation yet.

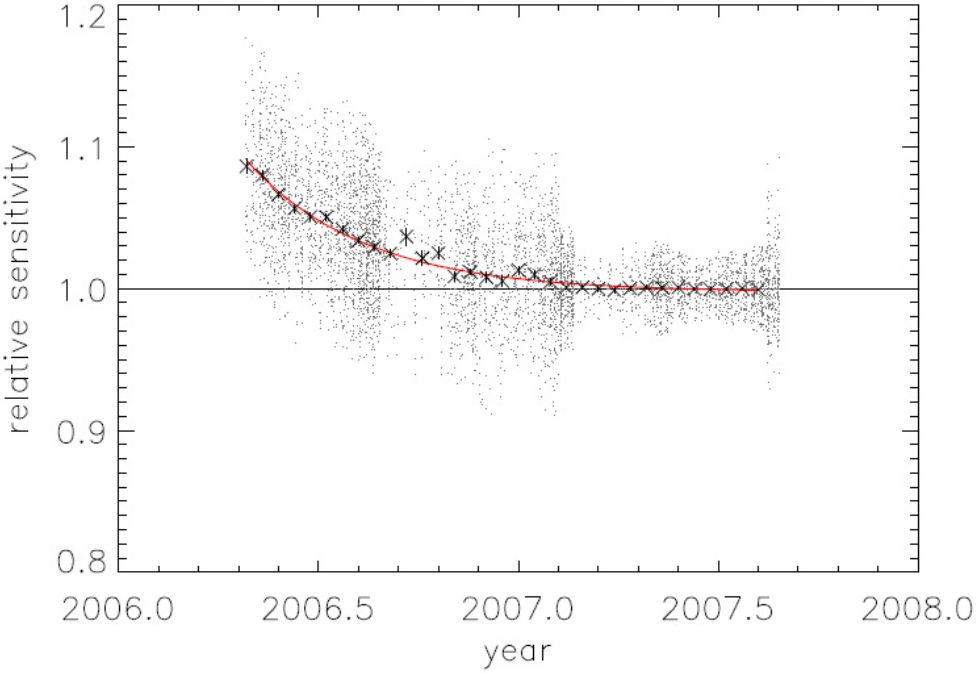

Figure 2.23 Time variation of the fluxes of the point sources normalized by the mean fluxes of those observed at Phase 2b (Amatsutsu 2015). Asterisks represent the 15-day mean values of the normalized fluxes and a red curve represents the best-fit result of fitting with an exponential function to the mean normalized fluxes.

Conversion from ADU/pix to MJy sr^{-1}

We converted the unit of the surface brightness from ADU to MJy sr^{-1}. For the pointed observations, the conversion factors had been already obtained by Tanabé et al. (2008). Here we evaluated the conversion factors for the all-sky surveys by comparing the surface brightness

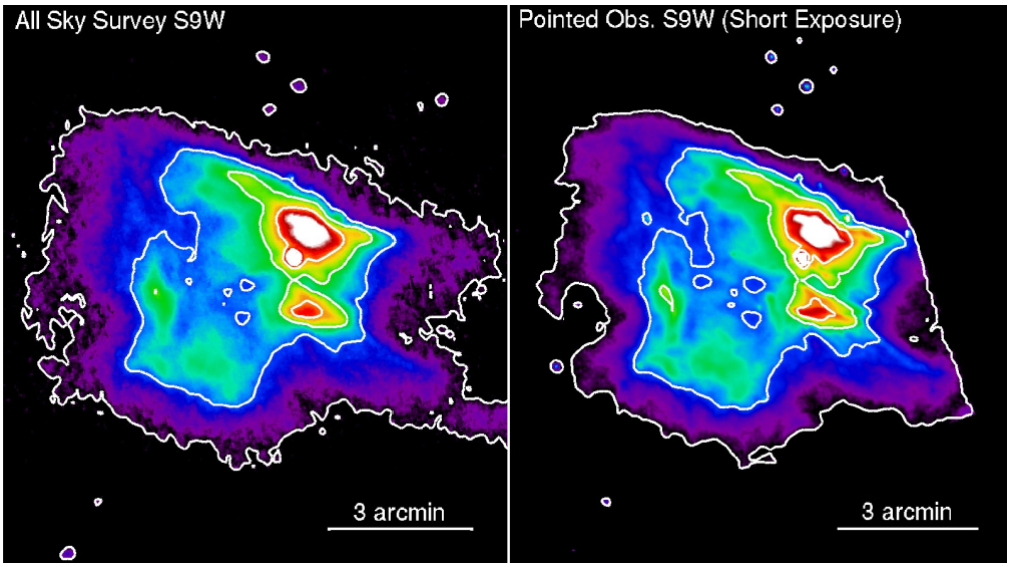

Figure 2.24 Images of NGC 7023 taken from the all-sky survey observation (left) and the pointed observation (right) in the 9 μm band (Yamagishi 2011).

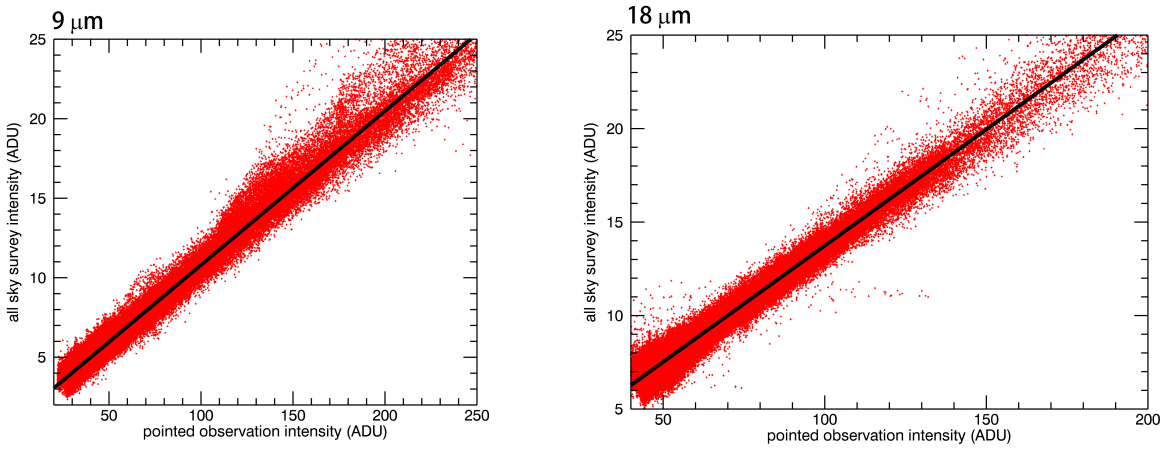

Figure 2.25 Correlation plots between the brightness taken from the all-sky survey observation and that taken from the pointed observation. Lines represent the best-fit result of linear fitting to the data points. Note that we used the median values of the brightnesses every 0.2 ADU for the brightness of the pointed observation because the number of data points in a low brightness region is about an order of magnitude larger than that in a high brightness region.

of an extended object taken from the all-sky survey observation with that taken from the pointed observation. We utilized the reflection nebula, NGC 7023, for the calibration, as shown in Fig. 2.24. Figure 2.25 shows the relations between the brightness taken from the all-sky survey observation and that taken from the pointed observation in the 9 and 18 μm bands. We fitted these relations

with lines. As a result, we obtained the conversion factors from ADU to MJy sr^{-1} for the all-sky survey observation in the maps with the pixel scale of $4\farcs68$ as 1 ADU $= 0.320 \pm 0.003$ MJy sr^{-1} and 1 ADU $= 0.501 \pm 0.006$ MJy sr^{-1} in the 9 and 18 μm bands, respectively.

Zodiacal emission subtraction

We established the IPD cloud model and removed the zodiacal emission based on the model. We describe the modeling procedure in Chapter 3 and present the results of the subtraction of the zodiacal emission in Chapter 4.

Removal of stray light from bright sources

The stray light appeared in the image when *AKARI* observed the region near a bright source whose brightness is higher than 10,000 Jy. Figure 2.26 shows the stray light from η Carina (η Car). The patterns of the stray light are parts of a distorted circle and an ellipse in the 9 and 18 μm bands, respectively. The position of the stray light with respect to the bright source depends on the scan direction as can be seen in Fig. 2.26. Fortunately, since the regions which suffer the stray light from the bright sources are different between Phases 1 (2b) and 2a, we can identify and remove the stray light by comparing the different seasonal maps.

We show the method of the removal of the stray light by taking η Car for example. Figure 2.27 shows the difference map between Phases 1 and 2a in the 18 μm band for the same region as in Fig. 2.26 . We measured the root mean square (RMS) value of the brightness fluctuation in the rectangular region indicated by the black box in Fig. 2.27. We judged that the regions of the brightness higher than the $+2\sigma$ level are affected by the scattered light at Phase 1 and that those of the brightness lower than the -2σ level are affected by the scattered light at Phase 2a. We masked the regions affected by the stray light as shown in Fig. 2.28. We recovered the masked regions in each season by combining all the seasonal maps as shown in Fig. 2.29.

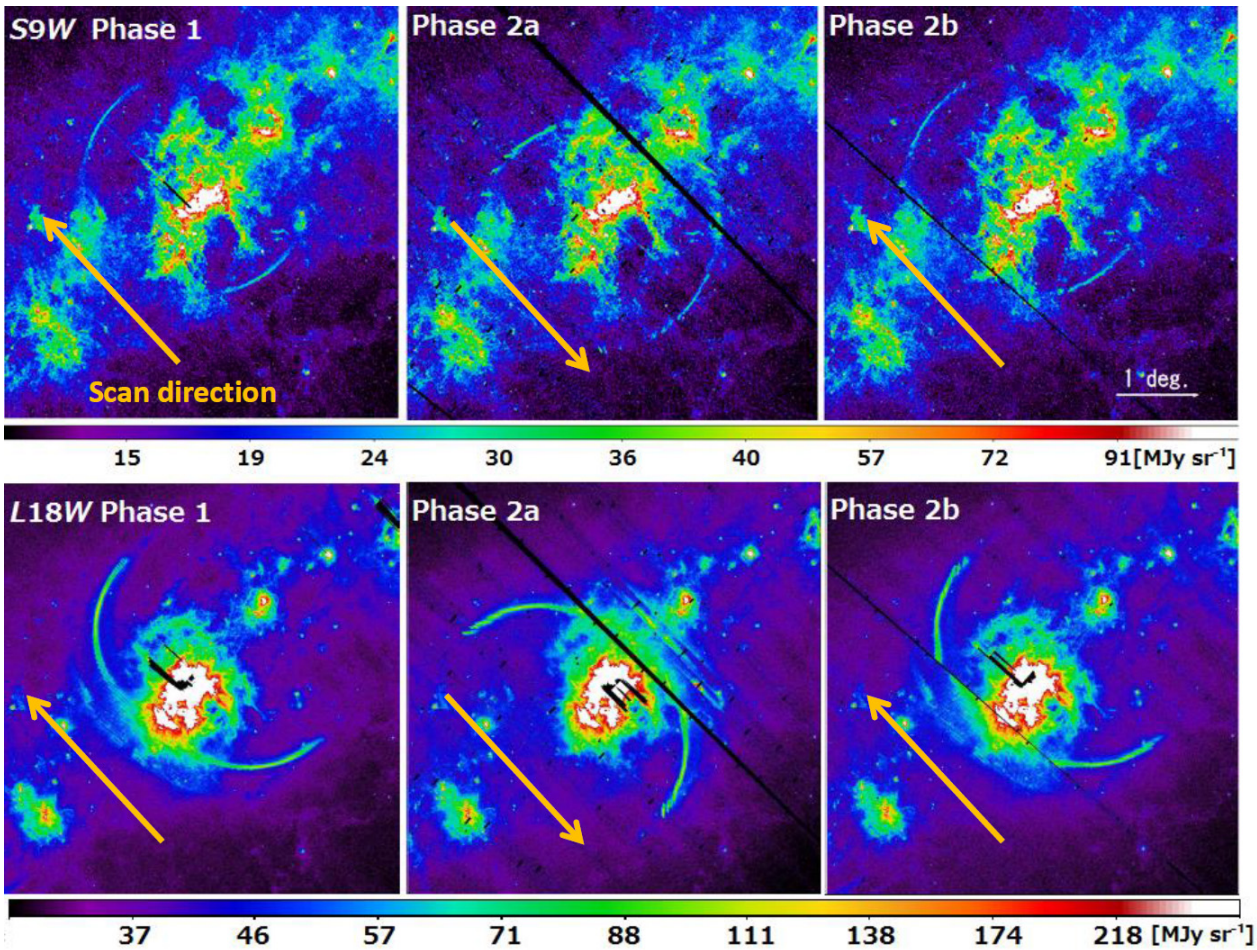

Figure 2.26 Images of η Car at Phases 1, 2a, and 2b from left to right. The top and the bottom panels show the 9 and 18 μm maps, respectively. Arrows represent the scan directions.

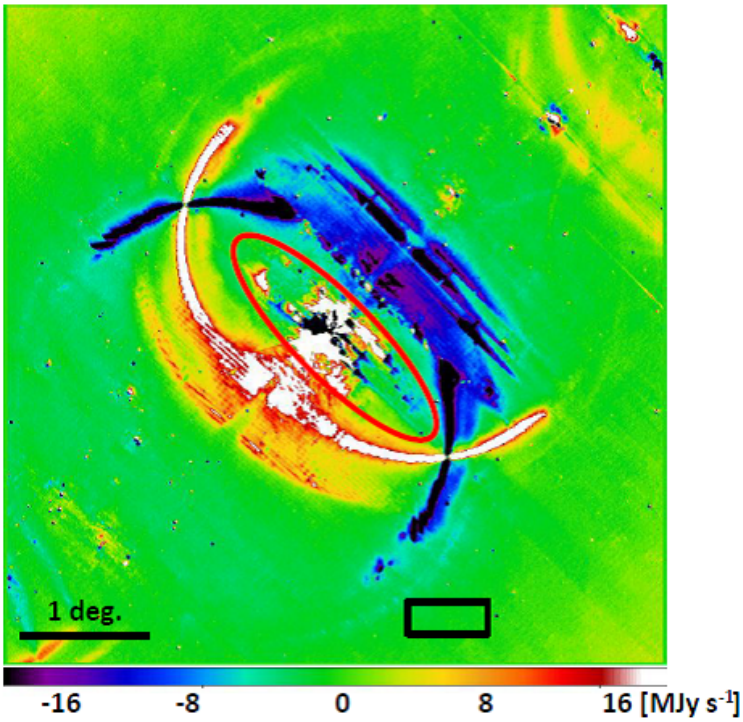

Figure 2.27 Difference image of η Car between Phases 1 and 2a in the 18 μm band. The RMS value is calculated in the region indicated by a black box to determine the threshold for the mask.

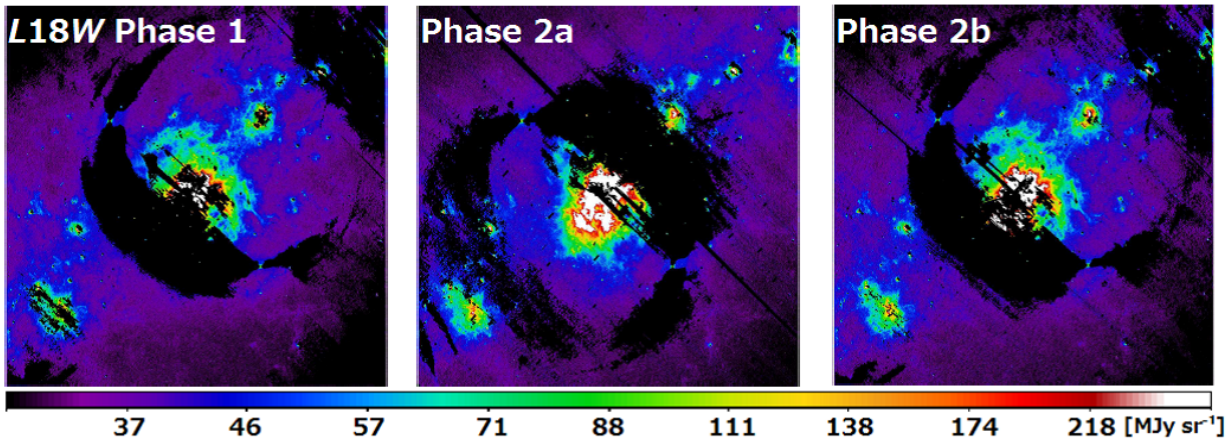

Figure 2.28 Images of η Car after masking the stray light in the 18 μm band.

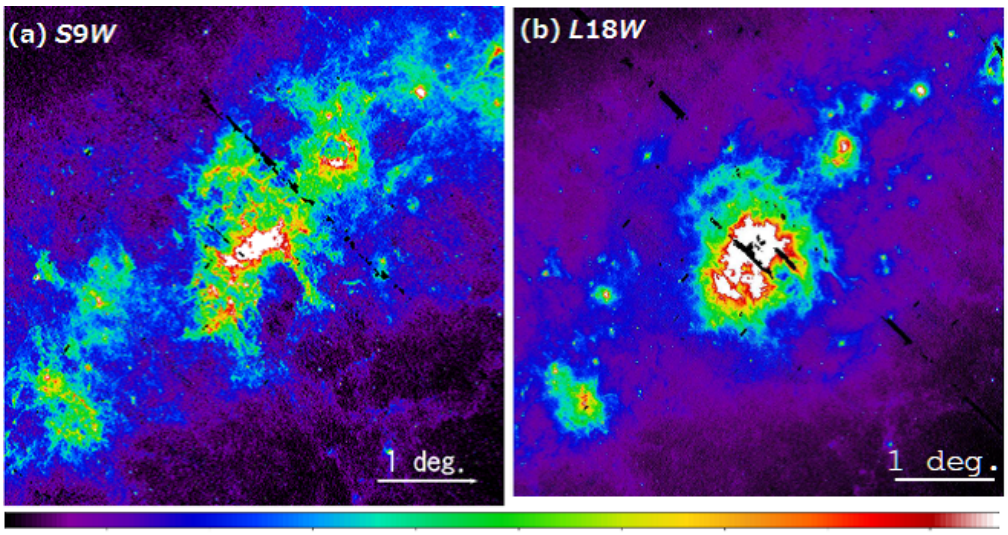

Figure 2.29 Images of η Car after subtraction of the stray light by combining all the seasonal maps where the stray light is masked in the (a) 9 μm and (b) 18 μm bands.

Earthshine subtraction

The earthshine is stray light from the Earth, which is scattered on the telescope baffle. It appeared near the ecliptic poles only at Phases 1 and 2b (Verdugo et al. 2007; Egusa et al. 2015; Pyo et al. 2010), whose brightness is ~ 1 and ~ 5 MJy sr^{-1} in the 9 and 18 μm bands, respectively. Figure 2.30 shows the *AKARI* mid-IR all-sky diffuse maps after subtraction of the zodiacal emission in the ecliptic coordinates. As can be seen in these maps, the earthshine appears in the north ecliptic pole regions only at Phases 1 and 2b. On the other hand, the earthshine at the south ecliptic pole cannot be seen clearly because the brightness is much lower than that at the north ecliptic pole. We therefore removed the earthshine only in the north ecliptic pole region. In order to remove the earthshine from the maps, we utilized the difference between the brightness at Phase 1 (2b) and that at Phase 2a. Figure 2.31 shows the templates of the distributions of the earthshine, which are defined as the regions of the brightnesses three times higher than the brightness fluctuation in the difference maps between Phases 1 (2b) and 2a at ecliptic latitudes higher than 40°. After removing the earthshine, we combined all the seasonal maps as shown in Fig. 2.32.

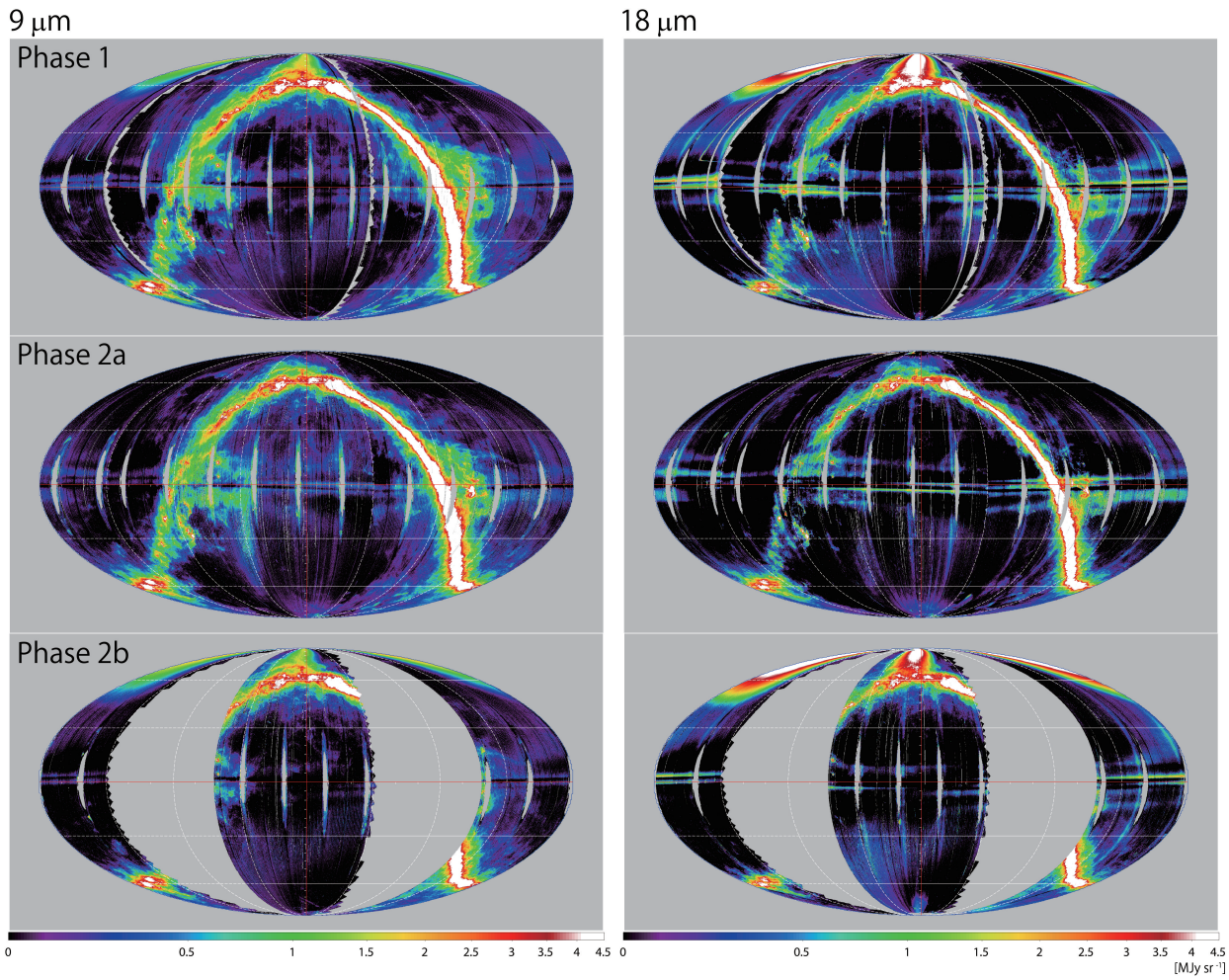

Figure 2.30 *AKARI* mid-IR all-sky diffuse maps after subtraction of the zodiacal emission in the ecliptic coordinates.

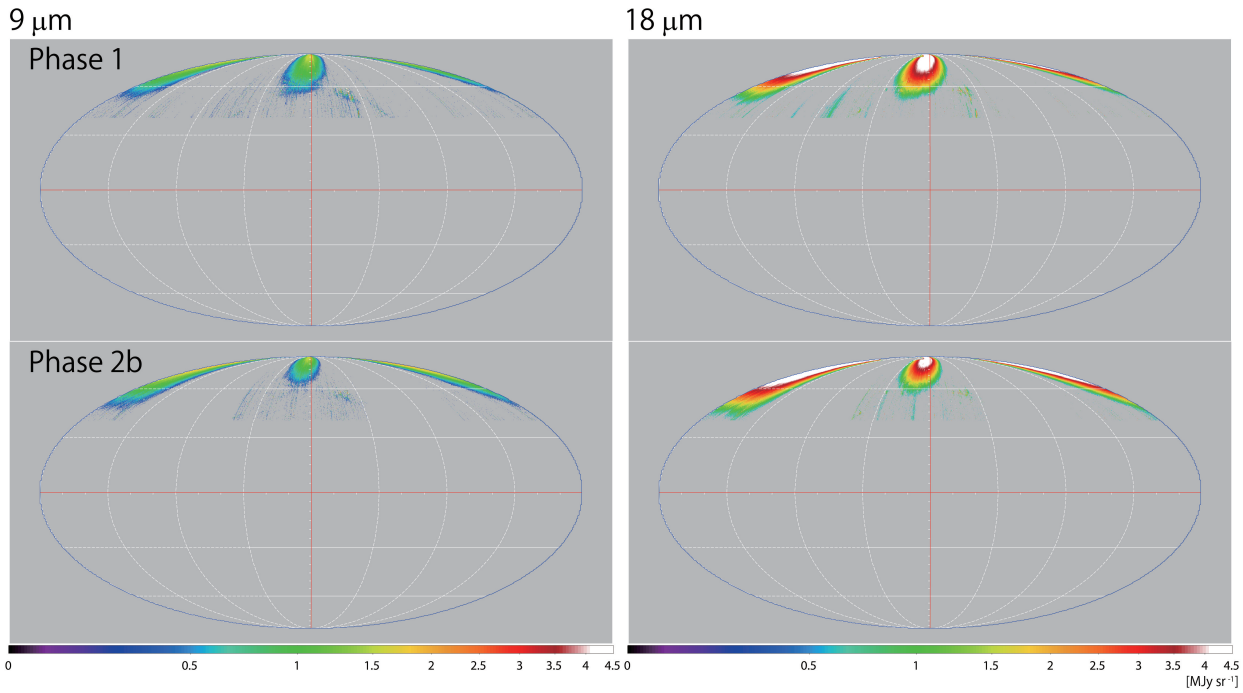

Figure 2.31 Templates of the distributions of the earthshine produced from the difference between the brightness at Phase 1 (2b) and that at Phase 2a in the regions at ecliptic latitudes higher than 40°.

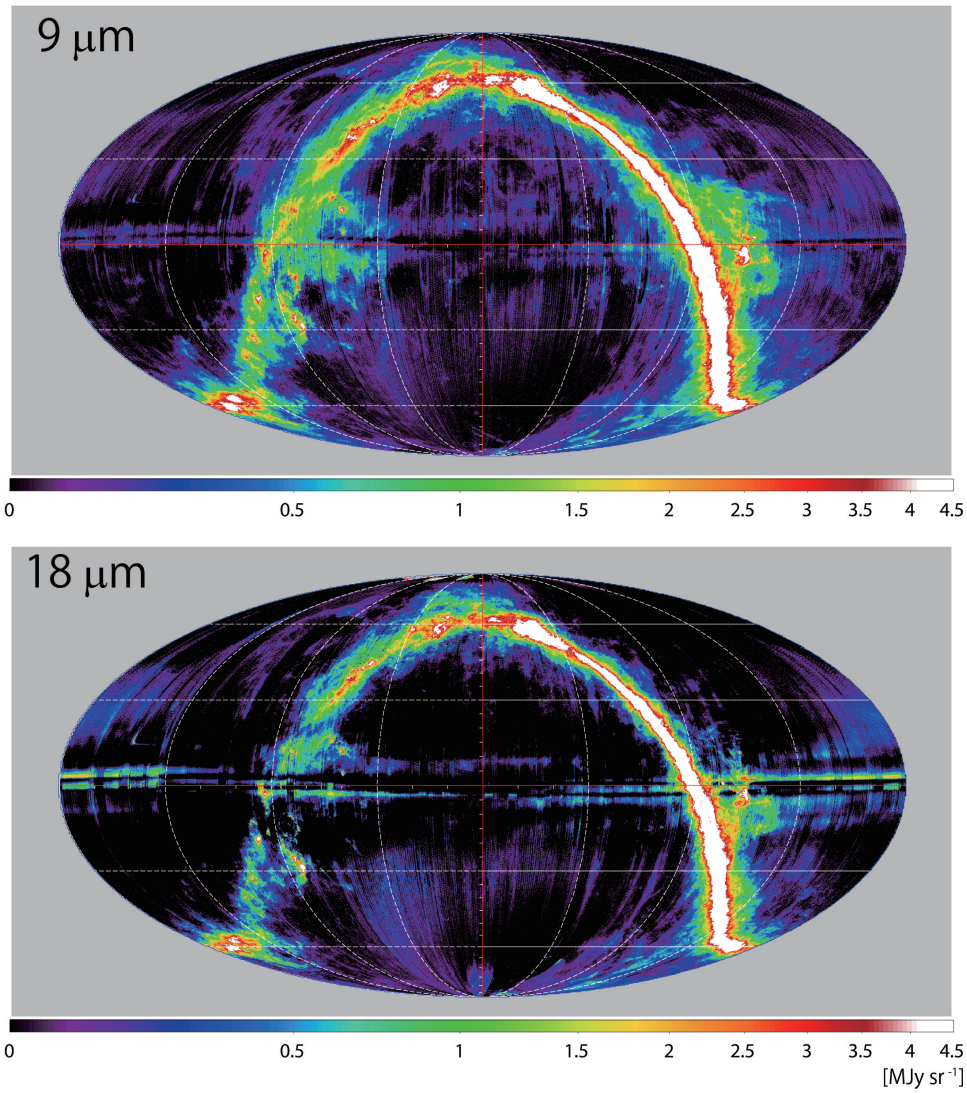

Figure 2.32 *AKARI* mid-IR all-sky diffuse maps after combining all the seasonal maps where the zodiacal emission and the earthshine are subtracted.

Chapter 3

Modeling of the Zodiacal Emission

The brightness of the zodiacal emission varies with time because of the orbital motion of the Earth relative to the IPD cloud, while the brightnesses of the other components such as the Galactic component do not vary. There are three reasons why the brightness of the zodiacal emission varies with time. The first reason is that a midplane of the IPD cloud is inclined by about 1°–3° with respect to the ecliptic plane, which has been confirmed by earlier studies such as those mentioned in Chapter 1. Figure 3.1 shows an example of the brightness variations at the ecliptic poles due to the inclination of the IPD cloud. As can be seen in this figure, the brightnesses at the poles vary with the Earth's position. The second reason is that the orbit of the Earth has an eccentricity of 0.0167. The third reason is that the cloud center is considered to be shifted from the Sun by $\sim 10^{-3}$–10^{-2} AU (Wright 1998; Kelsall et al. 1998).

For determination of the model parameters, Kelsall et al. (1998) used the seasonal variation of the brightness in the DIRBE maps as a time-varying component of the brightness of the zodiacal emission, in order to separate the zodiacal emission from the other components. However, the modeling which considers only time-varying components cannot reproduce the overall distribution of the zodiacal emission very well, because there remains the residual component, whose level is higher than 0.5 MJy sr^{-1}, in the DIRBE 12 and 25 μm maps (Kelsall et al. 1998) and the *AKARI* 9 μm map (Pyo et al. 2010). We therefore introduce a new method; we determine the parameters in the Kelsall model using the absolute brightness (i.e., both time-varying and non-time-varying components) of the zodiacal emission in the *AKARI* mid-IR maps.

3.1 The Kelsall Model

As explained in Section 1.1, the Kelsall model adopts three cloud components: the smooth cloud, the dust bands, and the MMR component. The brightness of the zodiacal emission observed at

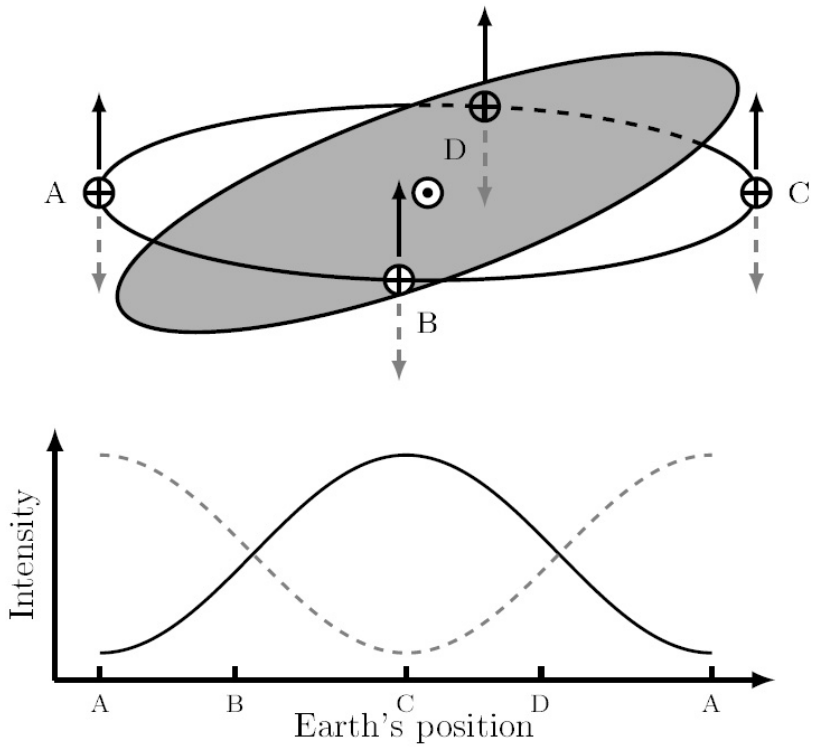

Figure 3.1 Brightness variations at the ecliptic poles against the Earth's position (Pyo et al. 2010). The Earth's positions are marked with A, B, C, and D. The upward arrows and the downward arrows indicate the directions of the north and the south ecliptic poles, respectively, in the top panel. A black solid curve and a gray dashed curve represent the surface brightnesses at the north and the south ecliptic poles, respectively, in the bottom panel.

the wavelength λ (i.e., 9 or 18 μm), at the celestial position p, and at the time t is calculated by integrating the thermal emission along the line of sight s, summed for the three components c as

$$S_\lambda(p,t) = \sum_{c=1,2,3} \int n_c(X,Y,Z)\varepsilon_\lambda B_\lambda(T)ds, \tag{3.1}$$

where $n_c(X,Y,Z)$ is the density of each component at position (X,Y,Z) and ε_λ is the emissivity modification factor that measures deviations from the Planck function $B_\lambda(T)$. The three-dimensional position in our Solar System (X,Y,Z) is defined with the geocentric ecliptic coordinates (λ,β) as

$$\begin{aligned} X &= R_\oplus \cos\lambda_\oplus + s\cos\beta\cos\lambda, \\ Y &= R_\oplus \sin\lambda_\oplus + s\cos\beta\sin\lambda, \\ Z &= s\sin\beta, \end{aligned} \tag{3.2}$$

where $R_\oplus$ is the distance from the Earth to the Sun and $\lambda_\oplus$ is the heliocentric ecliptic longitude of the Earth. For simplicity, in this study, we use the same values of ε_λ for the above three components, although there are suggestions that the far-IR emissivity may be different between the components (Planck Collaboration XIV 2014). The distribution of the dust temperature is represented by equation (1.3) and the dust temperature at 1 AU, T_0, is fixed at 286 K. We normalize ε_λ to unity at 18 μm, while Kelsall et al. (1998) normalized ε_λ to unity at 25 μm.

3.1.1 Model Components

Although the detail of the Kelsall model is described in Kelsall et al. (1998), we give basic information here. The three-dimensional distribution of each cloud component in the Kelsall model is shown in Fig. 3.2.

3.1.1.1 Smooth Cloud

The distribution of the dust density of the smooth cloud is represented as

$$n_s(X, Y, Z) = n_0 R_c^{-\alpha} f(\zeta), \tag{3.3}$$

where

$$R_c = \sqrt{(X - X_0)^2 + (Y - Y_0)^2 + (Z - Z_0)^2}, \tag{3.4}$$

$$\zeta \equiv |Z_c/R_c|, \tag{3.5}$$

$$Z_c = (X - X_0)\sin\Omega\sin i - (Y - Y_0)\cos\Omega\sin i + (Z - Z_0)\cos i, \tag{3.6}$$

and (X_0, Y_0, Z_0) is an offset from the Sun, and i and Ω are the inclination angle and the ascending node longitude of the midplane, respectively. The vertical distribution, $f(\zeta)$, is written as

$$f(\zeta) = \exp(-\beta g^\gamma), \tag{3.7}$$

where

$$g = \begin{cases} \zeta^2/2\mu & \text{for } \zeta < \mu, \\ \zeta - \mu/2 & \text{for } \zeta \geq \mu. \end{cases}$$

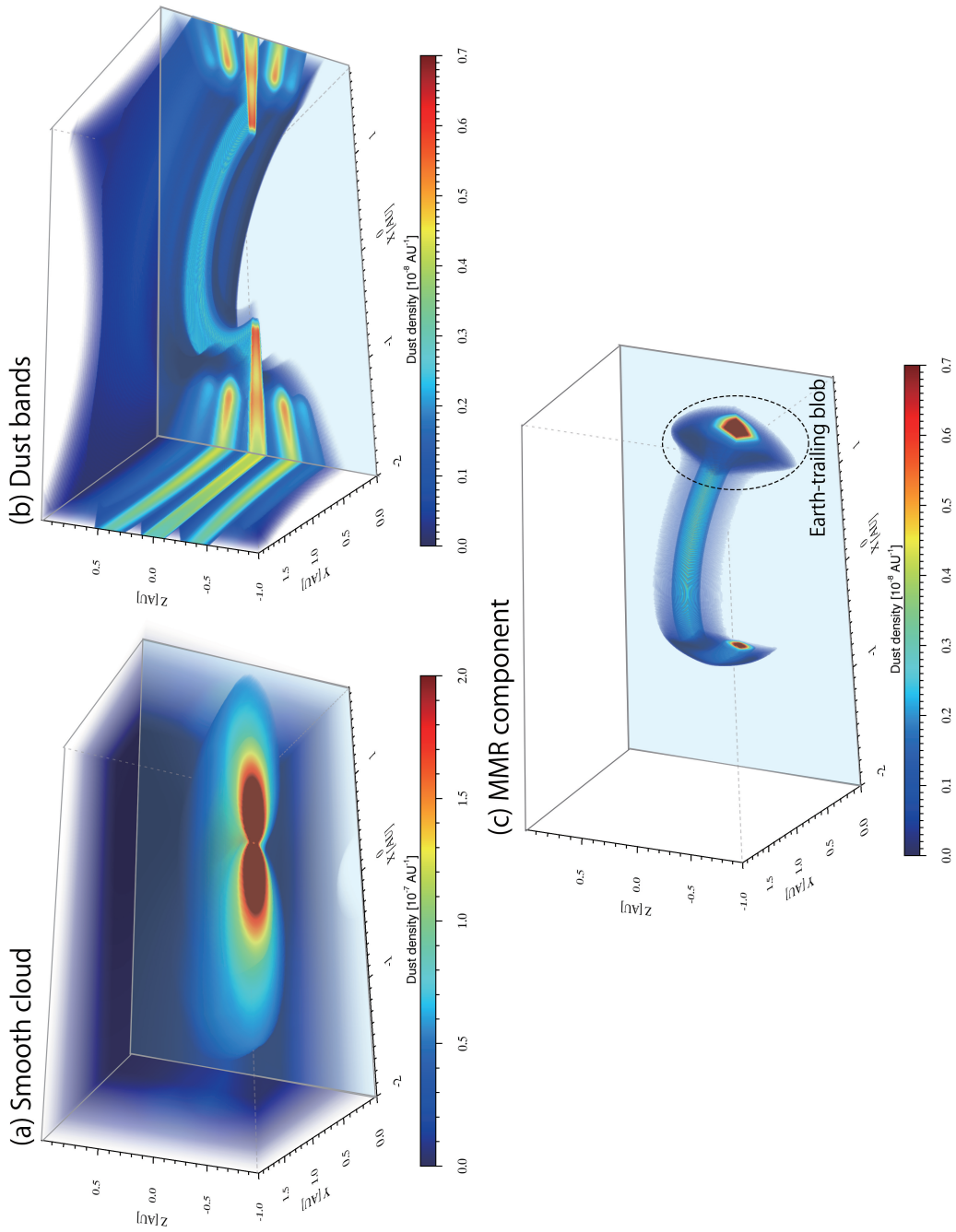

Figure 3.2 Three-dimensional distributions of the IPD cloud components in the Kelsall model: (a) the smooth cloud, (b) the dust bands, and (c) the MMR component. The cross section is the X–Z plane at $Y = 0$. The Earth-trailing blob is located at $(X, Y, Z) = (1, 0, 0)$ in this figure.

3.1.1.2 Dust Bands

As described in Section 1.1.1.2, the Kelsall model contains three pairs of the dust bands. The distribution of the dust density of each dust band i is represented as

$$n_{Bi}(X,Y,Z) = \frac{3n_{3Bi}}{R}\exp\left[-\left(\frac{\zeta_{Bi}}{\delta_{\zeta_{Bi}}}\right)^6\right]\left[1+\frac{1}{v_{Bi}}\left(\frac{\zeta_{Bi}}{\delta_{\zeta_{Bi}}}\right)^{p_{Bi}}\right]\left\{1-\exp\left[-\left(\frac{R}{\delta_{R_{Bi}}}\right)^{20}\right]\right\}, \quad (3.8)$$

where $\zeta_{Bi} \equiv |z_{Bi}/R|$. The vertical distance from the midplane, z_{Bi}, is defined in the same manner as Z_c in equation (3.6) with the inclination, i_{Bi}, and the ascending node, Ω_{Bi}, without the offset from the Sun. Note that we carry out the analysis based on the code obtained from the LAMBDA website,[1] but equation (3.8) is different from equation (8) in Kelsall et al. (1998) by a factor of $1/v_{Bi}$. We followed the code in this study.

3.1.1.3 MMR Component

The distribution of the dust density of the MMR component is represented as

$$n_R(X,Y,Z) = n_{\rm SR}\exp\left[-\frac{(R-R_{\rm SR})^2}{\sigma_{r\rm SR}^2}-\frac{|Z_R|}{\sigma_{z\rm SR}}\right]+n_{\rm TB}\exp\left[-\frac{(R-R_{\rm TB})^2}{\sigma_{r\rm TB}^2}-\frac{|Z_R|}{\sigma_{z\rm TB}}-\frac{\theta-\theta_{\rm TB}}{\sigma_{r\rm TB}}\right], \quad (3.9)$$

where the first and the second terms represent the distribution of the dust density of the circumsolar ring and that of the Earth-trailing blob, respectively. Note that there is a difference between equation (3.9) based on the code and equation (9) in Kelsall et al. (1998); a factor of 2 in the denominator of the radial and the longitude terms in the exponential were added to equation (9) in Kelsall et al. (1998). We followed the code in this study because it may be an error in the text of Kelsall et al. (1998), as argued by Planck Collaboration XIV (2014).

3.2 Fitting Technique

We carry out model fitting using the absolute brightness of the zodiacal emission in the *AKARI* 9 and 18 μm all-sky maps. We determine the model parameters to minimize the χ^2 value as

$$\chi^2 = \sum_{\lambda,p,t}\frac{1}{\sigma_\lambda^2(p,t)}\left\{I_\lambda(p,t)-S_\lambda(p,t)-C_\lambda\right\}^2, \quad (3.10)$$

where $\sigma_\lambda(p,t)$ is the uncertainty on the observed brightness, $I_\lambda(p,t)$, and C_λ is a isotropic component. We adopt 1 MJy sr^{-1} as the uncertainty considering all the calibration errors associated

[1] `http://lambda.gsfc.nasa.gov/product/cobe/dirbe_overview.cfm`

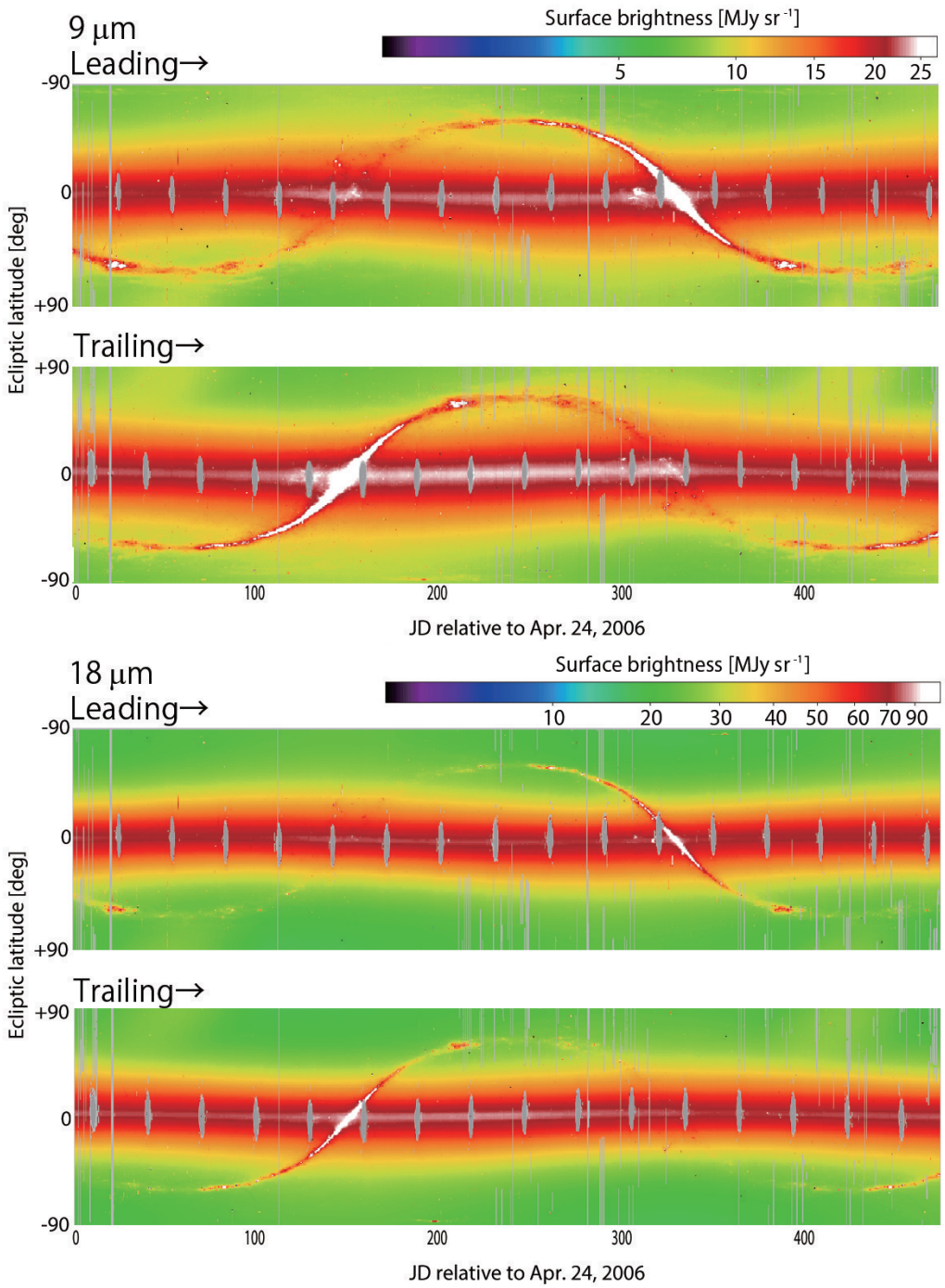

Figure 3.3 *AKARI* mid-IR all-sky diffuse maps on the plane of the ecliptic latitude versus the Julian day relative to 2006 April 24, where the scan direction is from bottom to top. For each of the 9 and 18 μm maps, the upper and the lower panels correspond to the leading and the trailing sides, respectively. The arrow shown in the top left of each map indicates the direction of the shift of the scan path, which is useful for comparison with the DIRBE maps in Fig. 4.6.

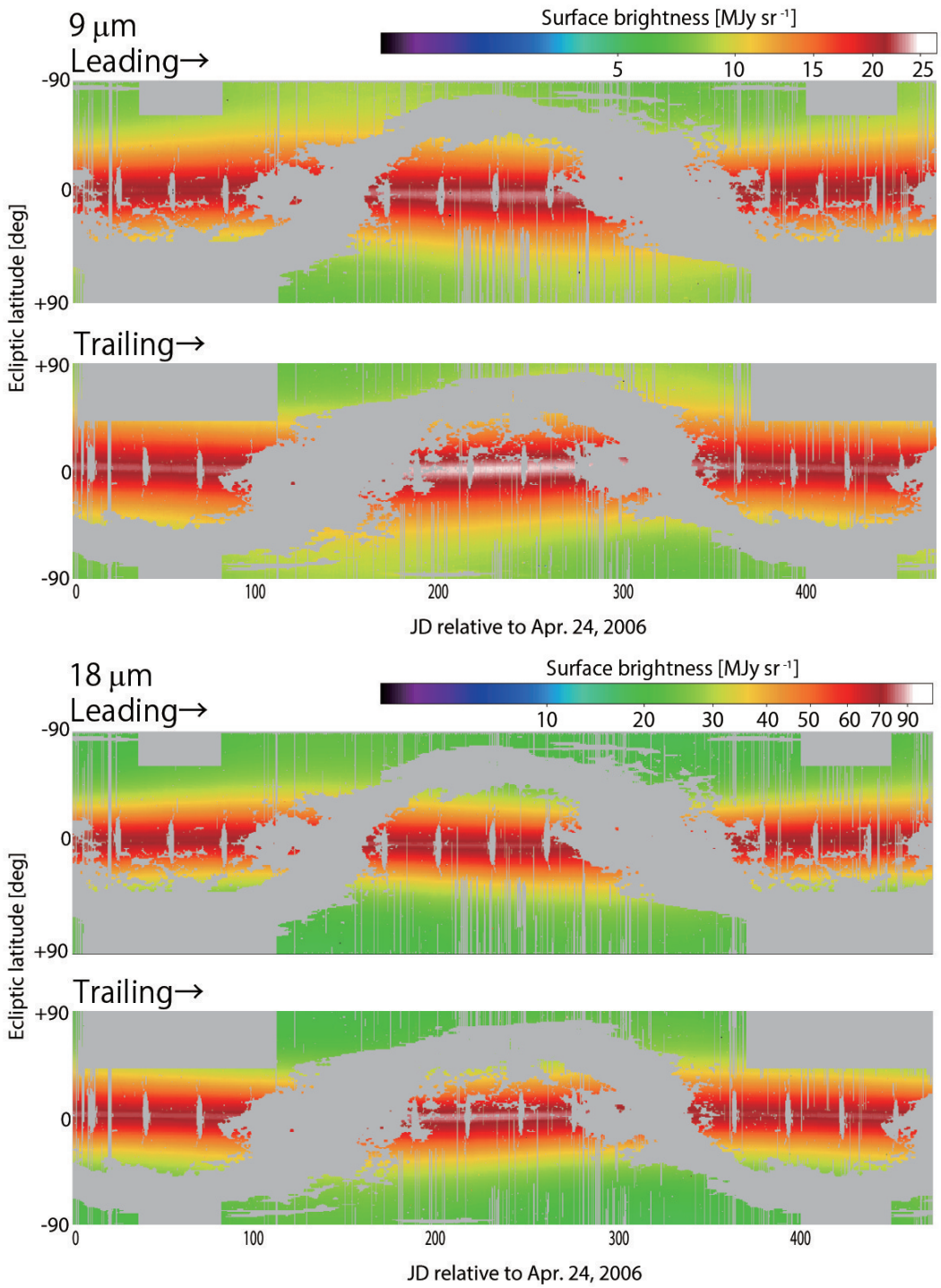

Figure 3.4 Same as Fig. 3.3, but after masking the regions affected by the Galactic emission and the earthshine.

with the data corrections described in Section 2.2. We use the all-sky maps in Fig. 3.3 with spatial sampling of $10'$ for the fitting. In order to avoid the Galactic component, we masked the regions of surface brightness levels higher than 6 MJy sr^{-1} in the *AKARI* 140 μm data (Doi et al. 2015). Considering typical interstellar colors of the mid- to far-IR brightness, the 6 MJy sr^{-1} limit at 140 μm corresponds to about 0.1 MJy sr^{-1} at 9 and 18 μm, which is 2–3 times higher than the brightness fluctuations in the 9 and 18 μm maps. In addition to the Galactic component, the *AKARI* maps suffer stray light from the Earth near the ecliptic poles, with the brightnesses of $\sim$1 and $\sim$5 MJy sr^{-1} in the 9 and 18 μm bands, respectively. This stray light corresponds to the earthshine scattered on the telescope baffle only in the summer season (Verdugo et al., 2007; Egusa et al., 2015; Pyo et al., 2010). We therefore did not use the regions observed in the period of May 5 to August 13 in 2006 and 2007 at ecliptic latitudes higher than 40° and the regions observed in the period of May 25 to July 14 in 2006 and 2007 at ecliptic latitudes lower than $-60°$. Figure 3.4 shows the maps after masking those components.

The Kelsall model intrinsically has 50 model parameters excluding those related to the scattering in the near-IR. Among them, we treat 24 parameters as free parameters, which are to be determined by the *AKARI* 9 and 18 μm band data in the present study. We mainly focus on large-scale structures of the IPD cloud in this study, and thus do not determine most of the geometrical parameters of the dust bands. We cannot determine the radial distribution of the MMR component because the solar elongation was fixed at 90°. The relations between each parameter are complicated because the observed brightness is expressed by integrating the thermal emission along the line of sight and summed for the three cloud components. In order to robustly determine the parameters, we model the zodiacal emission on a large-scale and a small-scale structure separately by taking the following step-by-step procedure as shown in Fig. 3.5.

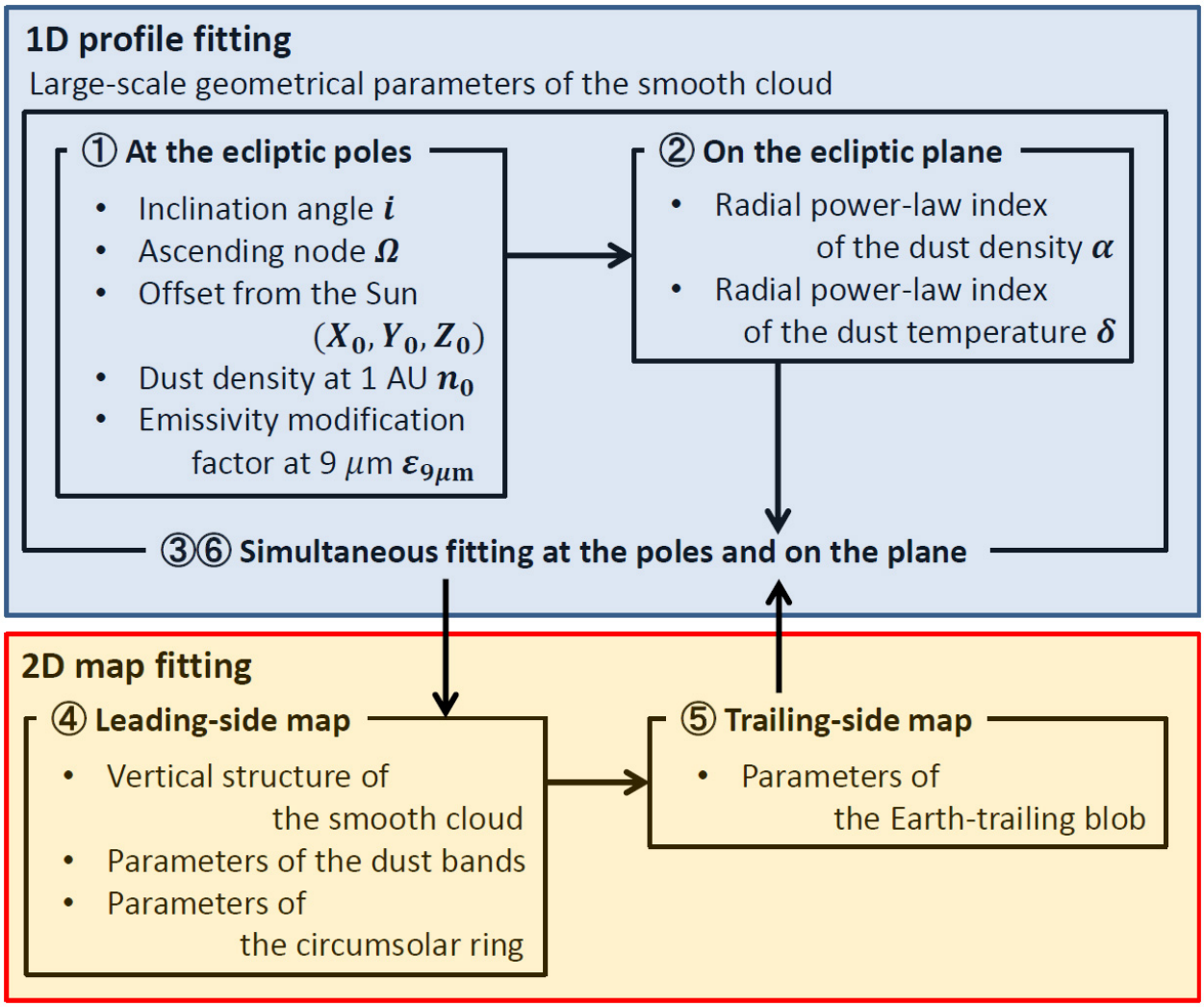

Figure 3.5 Process of the modeling of the zodiacal emission.

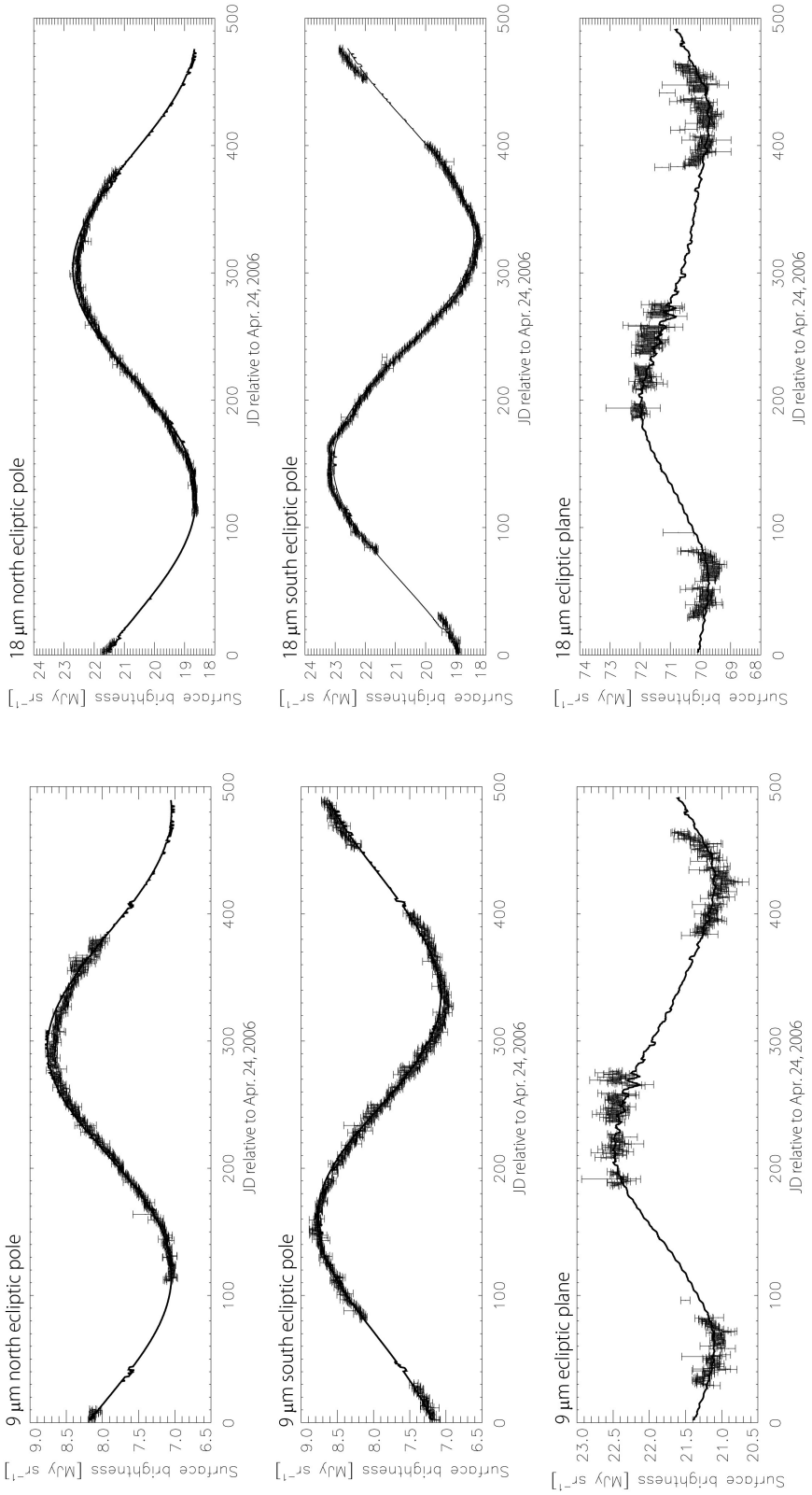

Figure 3.6 Surface brightness profiles observed at the ecliptic poles and on the ecliptic plane, where the error bars indicate the standard deviation of the brightness fluctuations calculated from the surrounding 7×5 grids. Curves represent the best-fit model.

3.2.1 One-Dimensional Fitting at the Poles and on the Plane

We determined large-scale geometrical parameters of the smooth cloud based on one-dimensional brightness profiles at the ecliptic poles and on the ecliptic plane as shown in Fig. 3.6. These profiles were created from the regions of absolute values of ecliptic latitudes higher than 89° for the ecliptic poles and lower than 0.°4 for the ecliptic plane. We used the data taken on the Earth-leading side, which are not affected by the Earth-trailing blob. Here we temporarily fixed the parameters of smaller-scale structures at those in the Kelsall model, which include the vertical structure of the smooth cloud and the parameters for the dust bands and the circumsolar ring.

First, we fitted the brightness profiles at the ecliptic poles. The brightness variations at the ecliptic poles are caused by the inclination of the smooth cloud with respect to the ecliptic plane, as shown in Fig. 3.1, and the offset from the Sun of the cloud center. We therefore determined the inclination angle, i, the ascending node, Ω, and the offset, (X_0, Y_0, Z_0). We also determined the dust density at 1 AU, n_0, and the emissivity modification factor at 9 μm, $\varepsilon_{9\mu\mathrm{m}}$, from the amplitudes of the variations and ratios of the 9 to 18 μm brightness, respectively. Next, we fitted the brightness profiles on the ecliptic plane. The brightness variations on the ecliptic plane are caused by the eccentricity of the Earth's orbit, which means that the brightness of the zodiacal emission is highest at the perihelion and lowest at the aphelion. We determined the radial power-law index of the dust density, α, and that of the dust temperature, δ, from the difference between the highest and lowest levels in the 9 and 18 μm bands. Then, we simultaneously fitted the brightness profiles at the poles and on the plane; here the above best-fit parameters were used as initial values and the fitting range was set to be within $\pm 10\sigma$ where σ was the errors estimated by the above fitting.

3.2.2 Two-Dimensional Fitting of the All-Sky Maps

Using the two-dimensional maps taken on the Earth-leading side, we determined the parameters of smaller-scale structures along the scan direction. For the large-scale geometrical parameters of the smooth cloud, the best-fit parameters in the one-dimensional fitting were used as initial values and the fitting range was again set to be within $\pm 10\sigma$. Once we obtained the parameters for the leading-side maps, we subtracted the zodiacal emission with the best-fit model parameters from the trailing-side maps, as shown in the top panel of Fig. 3.7, to determine the distribution of the Earth-trailing blob in the 9 and 18 μm bands. We then determined the parameters of the Earth-trailing blob from the subtracted maps. The bottom panel of Fig. 3.7 shows the model distribution of the Earth-trailing blob. Finally, we repeated the one-dimensional fitting where we fixed the parameters of the small-scale structures at the best-fit values in the present two-dimensional fitting but not at those in the Kelsall model. Table 4.1 summarizes the best-fit parameters thus obtained.

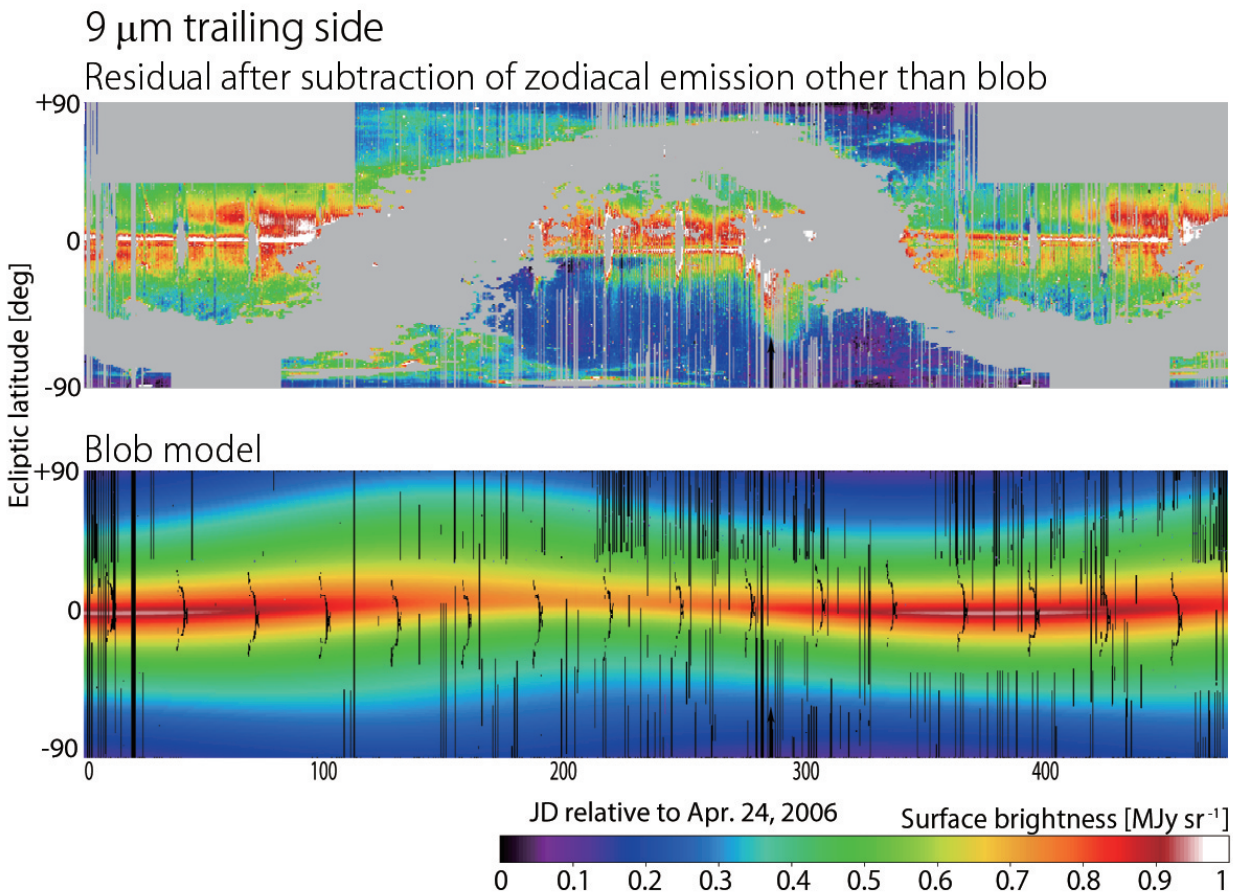

Figure 3.7 Top: *AKARI* 9 μm map on the trailing side after subtraction of the zodiacal emission other than the Earth-trailing blob. Bottom: model map of the Earth-trailing blob on the trailing side in the 9 μm band.

3.2.3 Uniqueness of the Model Parameters

Among the model parameters, the radial power-law index of the dust density, α, and that of the dust temperature, δ, have similar dependence on the brightness variations. Therefore, the uniqueness of the best-fit two parameters is checked. Figure 3.8 shows the brightness variations on the ecliptic plane obtained by changing the α and δ values from the best-fit values. As can be seen in this figure, the α-dependence and the δ-dependence on the brightness variations are different between the 9 and 18 μm bands, which means that the α and the δ values are uniquely determined by using both 9 and 18 μm data. Furthermore, Figure 3.9 shows the confidence contours of α and δ. This figure also indicates that the correlation between α and δ is small enough to show that the α value is significantly changed from the result in Kelsall et al. (1998).

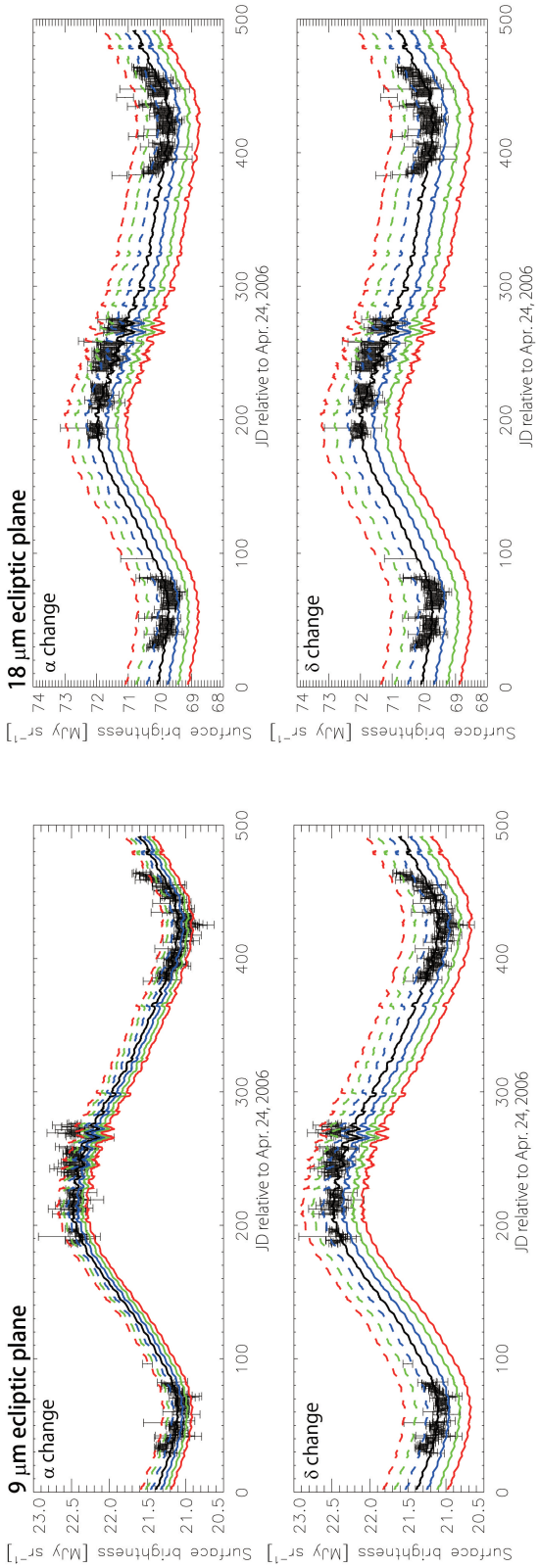

Figure 3.8 Same as the bottom panels of Fig. 3.6, but curves represent the brightness variations obtained by changing the α and δ values from the best-fit values. Blue, green, and red solid curves represent the $+1\sigma$, $+2\sigma$, and $+3\sigma$ changes, respectively, and blue, green, and red dashed curves represent the -1σ, -2σ, and -3σ changes, respectively.

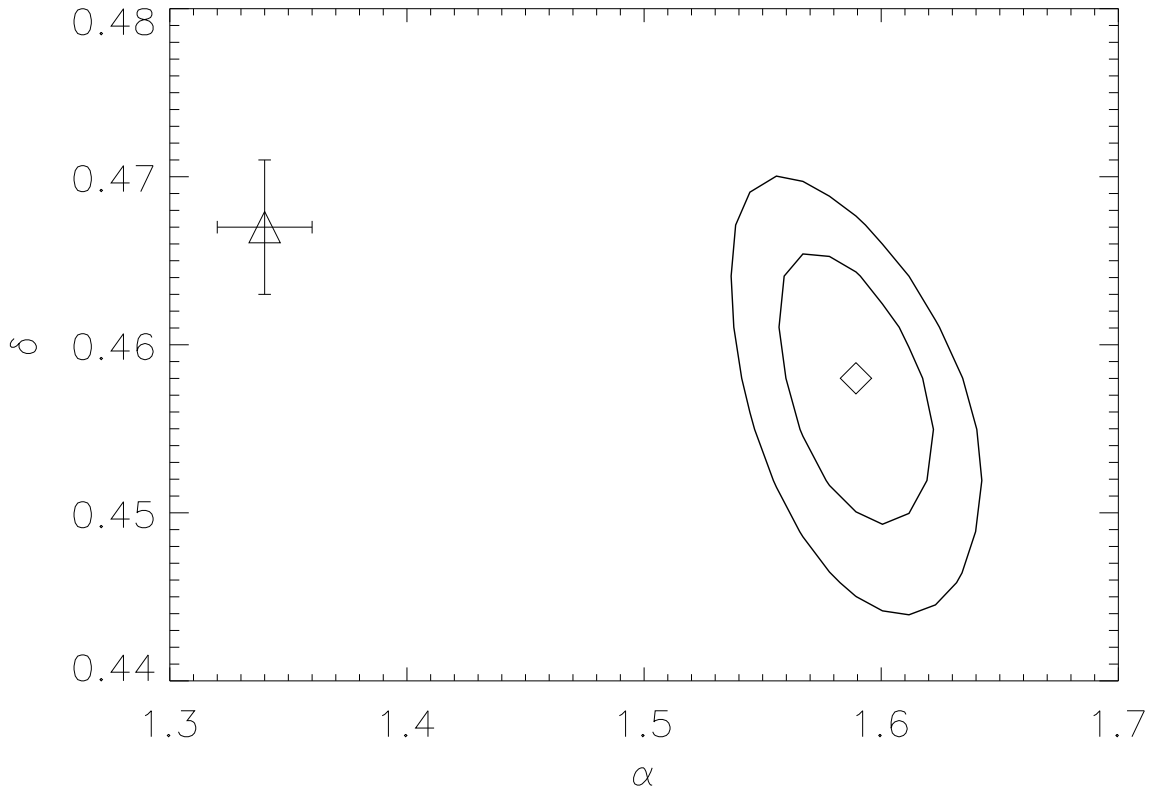

Figure 3.9 Confidence contours of the radial power-law index of the dust density of the smooth cloud, α, and the radial power-law index of the dust temperature, δ, at the 1σ and 2σ confidence levels. A diamond represents the best-fit values. A triangle represents the result in Kelsall et al. (1998), where the error bars indicate the 1σ uncertainties.

Chapter 4

Results

4.1 Improvement of the Zodiacal Model Fitting

Figure 4.1 shows the *AKARI* mid-IR all-sky maps after subtraction of the zodiacal emission obtained with the new model. For comparison, the residual maps after subtraction of the zodiacal emission with the Kelsall model are also shown in Fig. 4.2, where the emissivity modification factors and the isotropic component levels at 9 and 18 μm are determined with the *AKARI* data. As can be seen in these maps, the new model successfully reduces the residual levels. The RMS values of the residual components improve from 0.16 to 0.08 MJy sr^{-1} at 9 μm and from 0.31 to 0.20 MJy sr^{-1} at 18 μm from the Kelsall model to the new model. Figure 4.3 shows the histograms of the residual brightness after subtraction of the zodiacal emission. As can be seen in this figure, the distribution of the residual levels with the new model is more symmetrical than that with the Kelsall model, with respect to the zero level. Moreover, the width of the distribution with the new model is smaller than that with the Kelsall model, especially in the 9 μm band. This result demonstrates that the new model better reproduces the zodiacal emission in the *AKARI* data than the Kelsall model.

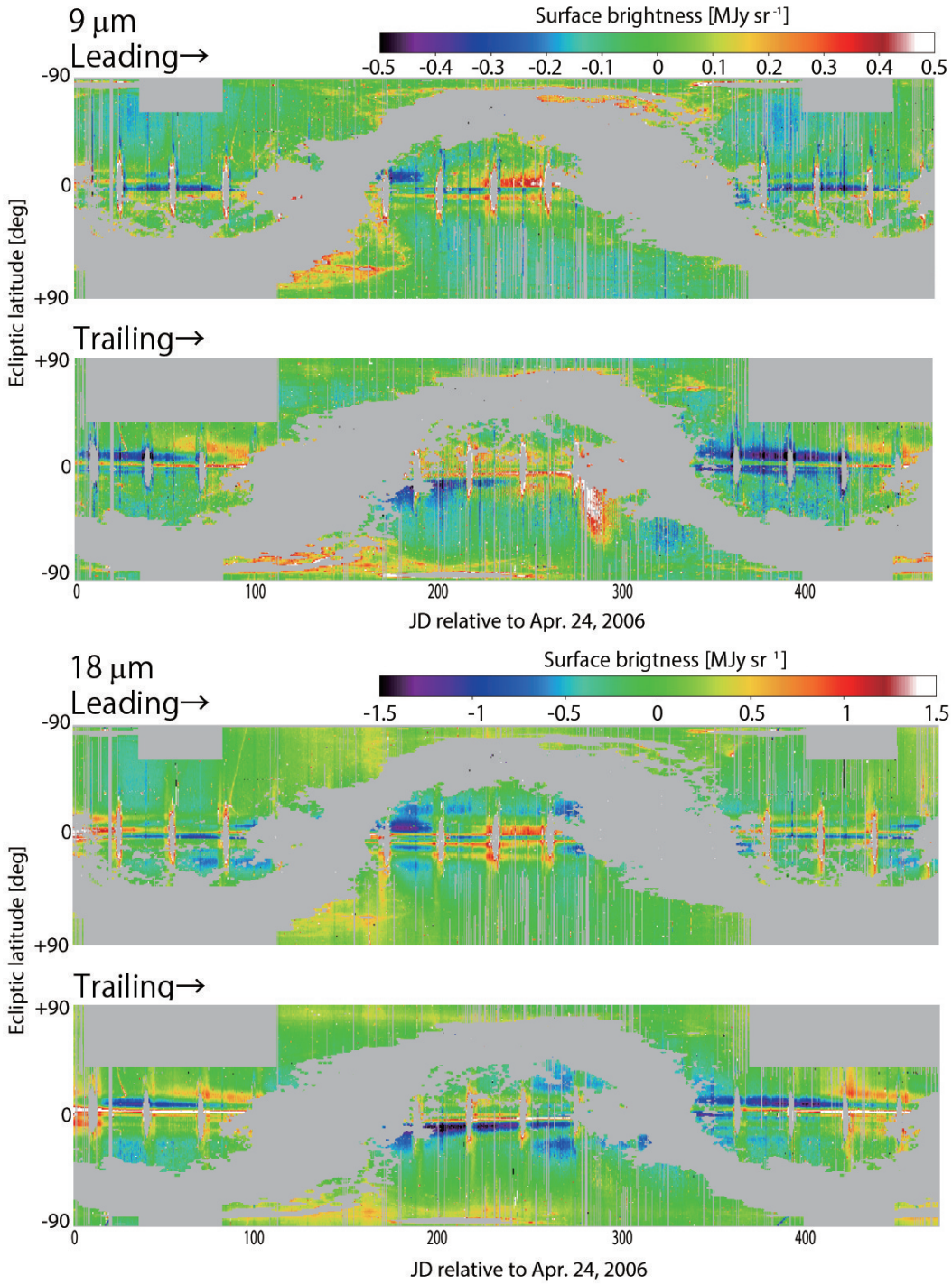

Figure 4.1 *AKARI* mid-IR maps after subtraction of the zodiacal emission with the new model. Note that the color scales are different from those used in Fig. 3.4 to emphasize faint residual components.

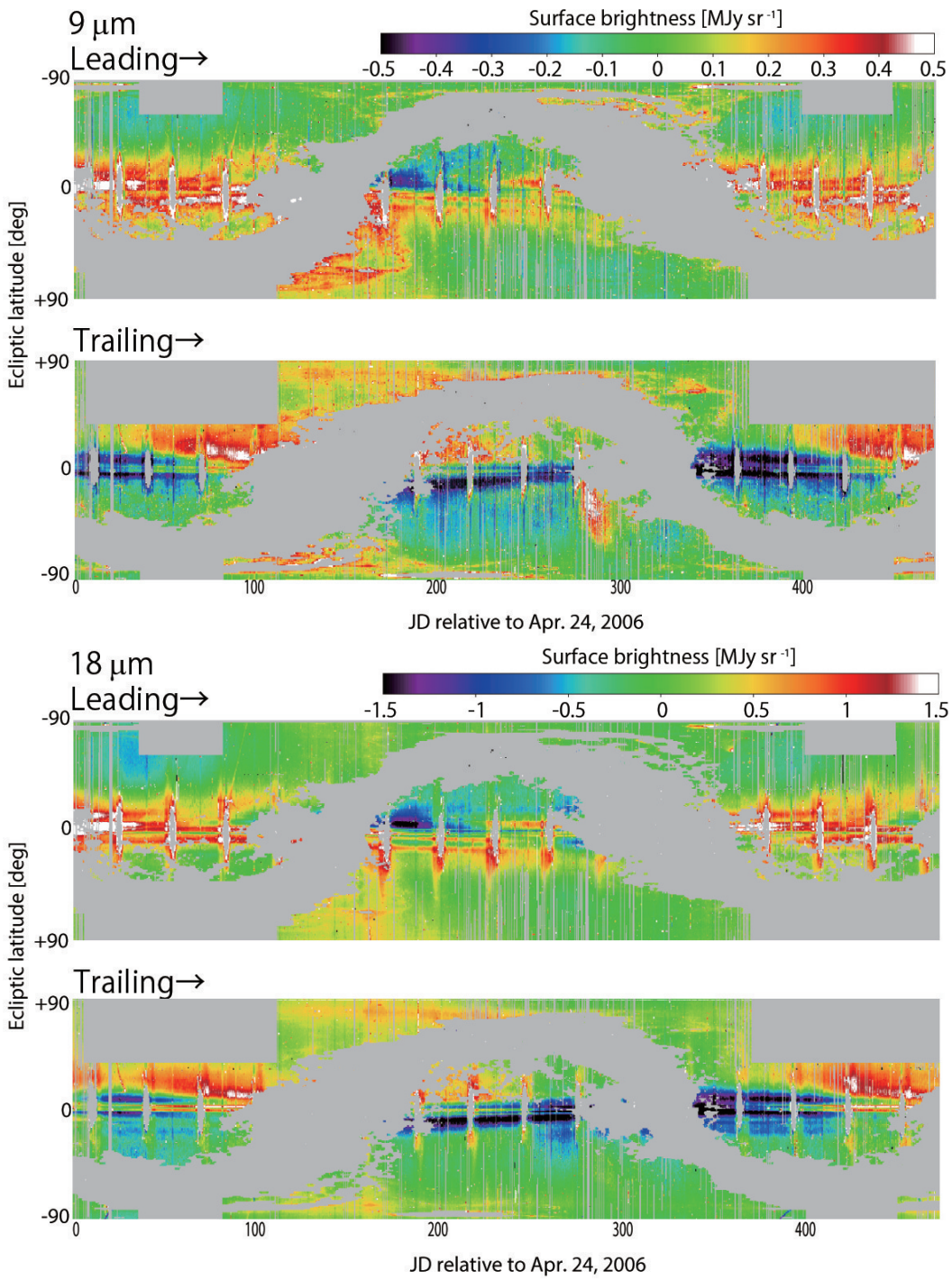

Figure 4.2 Same as Figure 4.1, but the Kelsall model is used for subtraction of the zodiacal emission.

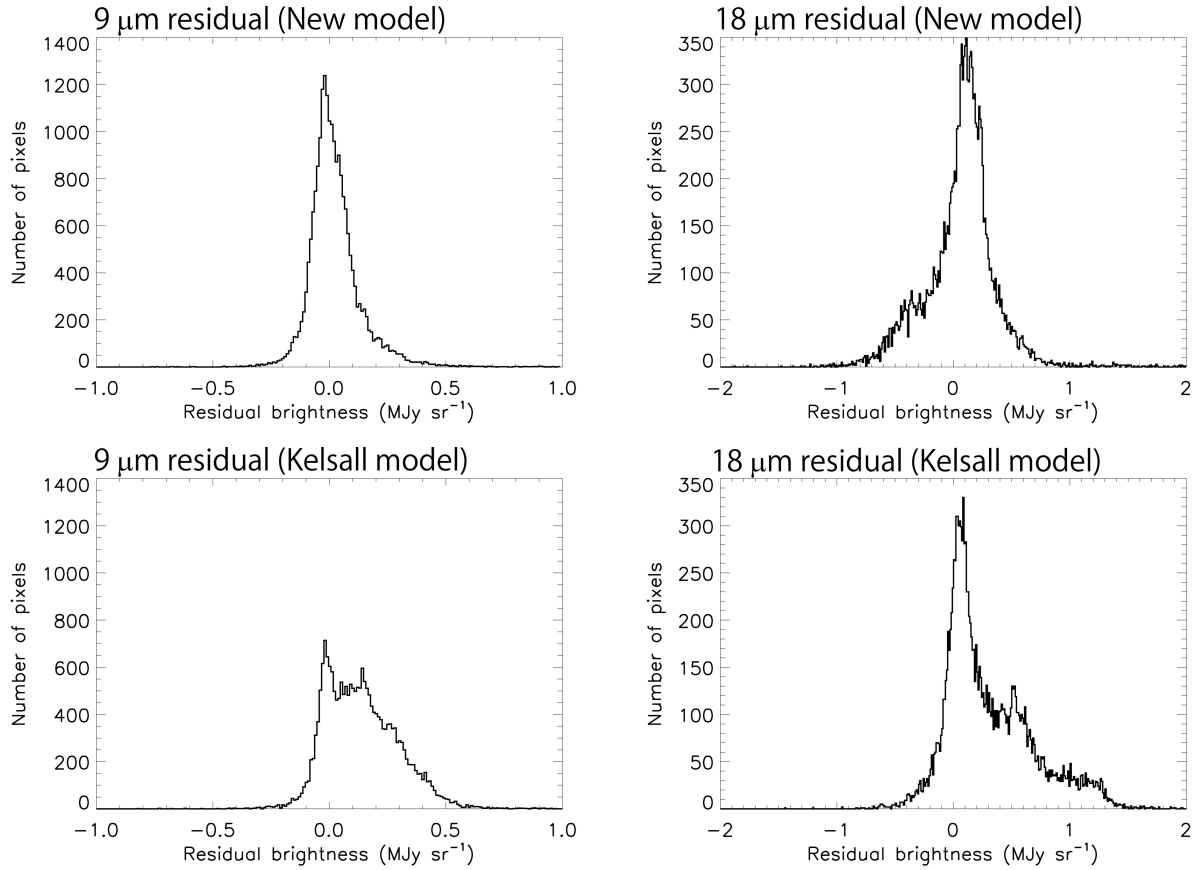

Figure 4.3 Histograms of the residual brightness after subtraction of the zodiacal emission with the new model (top) and with the Kelsall model (bottom). The bin size is 0.01 MJy sr^{-1}.

4.2 Differences between the New Model and the Kelsall Model

The model parameters thus optimized are summarized in Table 4.1 in comparison with the result in Kelsall et al. (1998). The power-law index of the radial distribution of the dust density α and the vertical shape parameter β of the smooth cloud become significantly larger than those of the Kelsall model. This implies that the size of the smooth cloud is by about 10% more compact than previously thought. Figure 4.4 compares the distributions of the smooth cloud predicted with the new model and the Kelsall model.

For the dust bands, since we did not change most of the geometrical parameters, only the density parameters are listed in Table 4.1. However, in the *AKARI* mid-IR maps, we cannot recognize the narrow double peak structure of band 2, the strongest dust band, along the ecliptic latitude, whereas the double peak structure was adopted in the Kelsall model. Therefore,

Table 4.1. Parameters of the IPD cloud model in Kelsall et al. (1998) and in the present study

Parameter	Name of parameter	Kelsall et al. 1998	Present study
	All cloud components		
T_0 (K)	Temperature at 1 AU	286 (fixed)	286 (fixed)
δ	Temperature power-law index	0.467 (0.004)	0.458 (0.006)
$\varepsilon_{9\,\mu\mathrm{m}}$	Emissivity modification factor at 9 μm	$\cdots$	0.8575 (0.0007)
	Smooth cloud		
n_0 (AU^{-1})	Density at 1 AU	1.134×10^{-7} (0.006×10^{-7})	1.578×10^{-7} (0.006×10^{-7})
α	Radial power-law index	1.34 (0.02)	1.59 (0.02)
β	Vertical shape parameter	4.14 (0.07)	4.85 (0.02)
γ	Vertical power-law index	0.94 (0.03)	1.043 (0.005)
μ	Widening parameter	0.19 (0.01)	0.180 (0.002)
i (deg)	Inclination	2.03 (0.02)	2.047 (0.007)
Ω (deg)	Ascending node	77.7 (0.6)	75.9 (0.1)
X_0 (AU)	X offset from the Sun	0.012 (0.001)	0.0153 (0.0002)
Y_0 (AU)	Y offset from the Sun	0.0055 (0.0008)	−0.0081 (0.0002)
Z_0 (AU)	Z offset from the Sun	−0.0022 (0.0004)	−0.00160 (0.00004)
	Dust bands		
n_{B1} (AU^{-1})	Density at 3 AU of band 1	5.6×10^{-10} (0.7×10^{-10})	5.6×10^{-10} (0.1×10^{-10})
n_{B2} (AU^{-1})	Density at 3 AU of band 2	2.0×10^{-9} (0.1×10^{-9})	3.70×10^{-9} (0.03×10^{-9})
n_{B3} (AU^{-1})	Density at 3 AU of band 3	1.4×10^{-10} (0.2×10^{-10})	0.06×10^{-10} (0.05×10^{-10})
	Circumsolar ring		
n_{SR} (AU^{-1})	Density at 1 AU	1.8×10^{-8} (0.1×10^{-8})	0.75×10^{-8} (0.06×10^{-8})
R_{SR} (AU)	Radius of peak density	1.0282 (0.0002)	1.0282 (fixed)
σ_{rSR} (AU)	Radial dispersion	0.025 (fixed)	0.025 (fixed)
σ_{zSR} (AU)	Vertical dispersion	0.054 (0.007)	0.066 (0.002)
	Earth-trailing blob		
n_{TB} (AU^{-1})	Density at 1 AU	1.9×10^{-8} (0.1×10^{-8})	2.08×10^{-8} (0.01×10^{-8})
R_{TB} (AU)	Radius of peak density	1.06 (0.01)	1.06 (fixed)
σ_{rTB} (AU)	Radial dispersion	0.10 (0.01)	0.10 (fixed)
σ_{zTB} (AU)	Vertical dispersion	0.09 (0.01)	0.151 (0.001)
θ_{TB} (deg)	Longitude with respect to Earth	−10 (fixed)	−10 (fixed)
$\sigma_{\theta\mathrm{TB}}$ (deg)	Longitude dispersion	12 (3)	11.10 (0.06)
$Z_{0,\mathrm{TB}}$ (AU)	z offset from the Sun	0.0 (fixed)	0.0206 (0.0005)
	Circumsolar ring + Earth-trailing blob		
i_{RB} (deg)	Inclination	0.49 (0.06)	0.97 (0.03)
Ω_{RB} (deg)	Ascending node	22.28 (0.001)	296 (1)
	Isotropic component		
$C_{9\,\mu\mathrm{m}}$ (MJy sr^{-1})	Brightness at 9 μm	$\cdots$	0.191 (0.004)
$C_{18\,\mu\mathrm{m}}$ (MJy sr^{-1})	Brightness at 18 μm	$\cdots$	0.246 (0.009)

Note. — For details of the parameters, see Kelsall et al. (1998). The values in the parentheses indicate 1σ errors.

the contribution of the double peak structure of band 2 has been removed in the new model $\left(\frac{1}{v_{B2}}\left(\frac{\zeta_{B2}}{\delta\zeta_{B2}}\right)^{p_{B2}} \to 0 \text{ in equation (3.8)}\right)$.

In addition, the Earth-trailing blob is likely to have a vertical offset, $Z_{0,\mathrm{TB}}$, of 0.0206 ± 0.0005 AU to the north direction. In order to demonstrate the necessity of introducing $Z_{0,\mathrm{TB}}$, Figure 4.5 shows a comparison between the residual maps on the trailing side with $Z_{0,\mathrm{TB}} = 0.0206$ AU and $Z_{0,\mathrm{TB}} = 0$ AU. In the residual maps with $Z_{0,\mathrm{TB}} = 0$ AU, the residual levels in the north regions are systematically higher than those in the south regions.

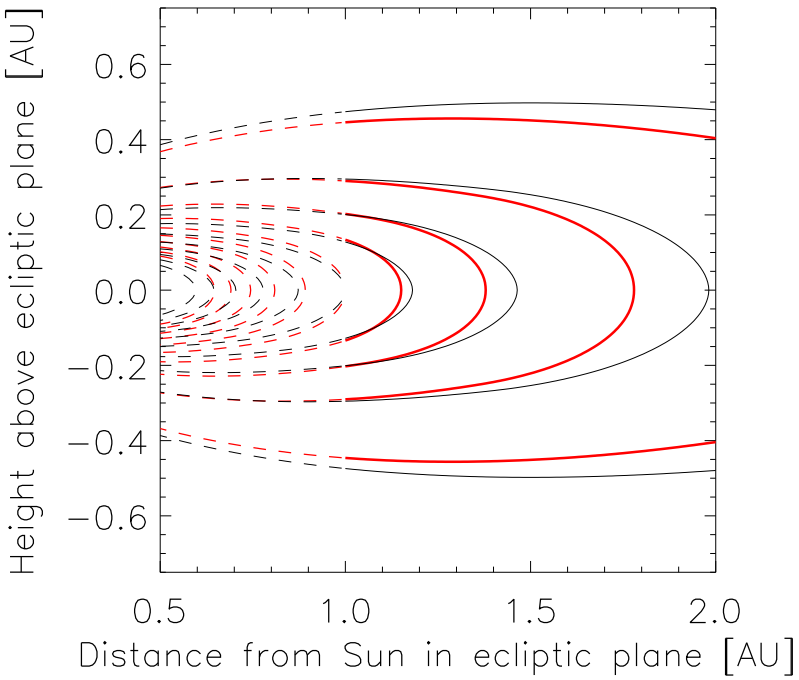

Figure 4.4 Isodensity contours for the smooth cloud. Red thick lines and black thin lines represent the new model and the Kelsall model, respectively. For the inner region where *AKARI* did not observe, the extrapolated values from the models are drawn by dashed lines. The drawing plane is the heliocentric meridian plane. Curves represent isodensities for $n = 2.0n_0$, $1.8n_0$, $1.6n_0$, $1.4n_0$, $1.2n_0$, $1.0n_0$, $0.8n_0$, $0.6n_0$, $0.4n_0$, $0.2n_0$ from inner to outer contours.

4.3 Confirmation of the Time Variation of the Zodiacal Emission

In this section, we investigate the cause of the changes in the model parameters as shown in Table 4.1. In order to confirm whether these changes are due to model improvements or temporal variations of the zodiacal emission, the new model is applied to the DIRBE data. Panels (a) and (c) of Fig. 4.6 show the DIRBE Solar Elongation = 90 deg Sky Maps in the 12 and 25 μm bands, respectively, in the ecliptic coordinates, after subtraction of the zodiacal emission with the new model. These maps contain both leading and trailing sides obtained in half a year observations; the region at ecliptic longitudes from 10° to 190° corresponds to the trailing side, while the other region corresponds to the leading side. For comparison with the *AKARI* maps, the ecliptic longitudes in these maps are equivalent to the observation days and the direction of the shift of the scan path is indicated by the arrows in Fig. 4.6.

As can be seen in these maps, the model over-predicts the brightness in the north regions on

the trailing side. The regions on the trailing side in these maps correspond to the regions with Day 250 to 440 in the *AKARI* maps in Fig. 4.1. Figure 4.7 compares the DIRBE 12 μm map with the *AKARI* 9 μm map on the trailing side. The zodiacal emission is asymmetrically subtracted from the DIRBE map with respect to the ecliptic plane comparing to the *AKARI* map. Hence the Earth-trailing blob component in the new model does not fit the DIRBE data well, suggesting that the geometry of the blob component has changed from the *COBE* epoch to the *AKARI* epoch. Since the over-subtracted region is systematically shifted to the north with respect to the ecliptic plane, the vertical offset, $Z_{0,\mathrm{TB}}$, should be smaller for the DIRBE data than for the *AKARI* data. In order to reduce the asymmetry, the $Z_{0,\mathrm{TB}}$ value is re-determined for the DIRBE data by using the 12 μm map because the asymmetry is clearer in the 12 μm map. The best-fit $Z_{0,\mathrm{TB}}$ thus determined for the DIRBE data is 0.007 ± 0.002 AU, which is smaller than that for the *AKARI* data ($Z_{0,\mathrm{TB}} = 0.0206$ AU). The change in $Z_{0,\mathrm{TB}}$ is significant (7σ), based on the χ^2 statistics. Then, we apply this value to the model for the 12 and 25 μm DIRBE data as shown in panels (b) and (d), respectively, of Fig. 4.6, where the asymmetry of the subtraction of the zodiacal emission is reduced from panels (a) and (c).

Figure 4.8 compares the new model ($Z_{0,\mathrm{TB}}$ is changed to better fit the DIRBE data) with the Kelsall model. Panels (a) and (c) show the residual maps after subtraction of the zodiacal emission with the new model at 12 and 25 μm, respectively, while panels (b) and (d) show those with the Kelsall model. As can be seen in Fig. 4.8, the DIRBE data are better fitted by the new model than by the Kelsall model. The RMS values of the residual components improve from 0.20 to 0.12 MJy sr^{-1} at 12 μm and from 0.31 to 0.20 MJy sr^{-1} at 25 μm from the Kelsall model to the new model. In summary, the changes of the model parameters are mostly due to model improvements, except for the vertical offset of the Earth-trailing blob; only the Earth-trailing blob has really changed its central offset position between the *COBE* and the *AKARI* epoch.

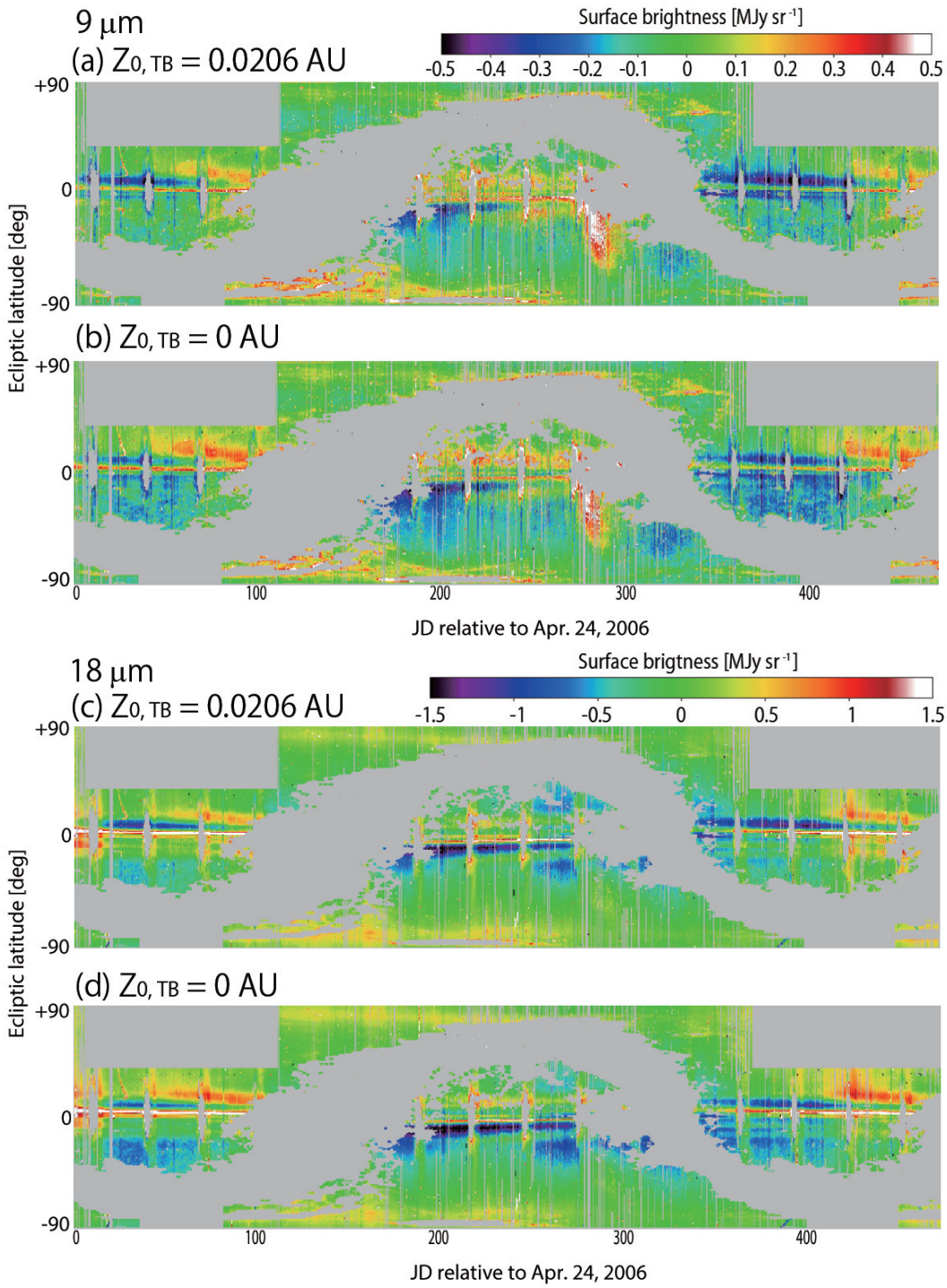

Figure 4.5 *AKARI* mid-IR maps on the trailing side after subtraction of the zodiacal emission with the new model. Panels (a) and (b) show the residual maps at 9 μm with $Z_{0,\mathrm{TB}} = 0.0206$ AU and $Z_{0,\mathrm{TB}} = 0$ AU, respectively. Panels (c) and (d) show the residual maps at 18 μm with $Z_{0,\mathrm{TB}} = 0.0206$ AU and $Z_{0,\mathrm{TB}} = 0$ AU, respectively.

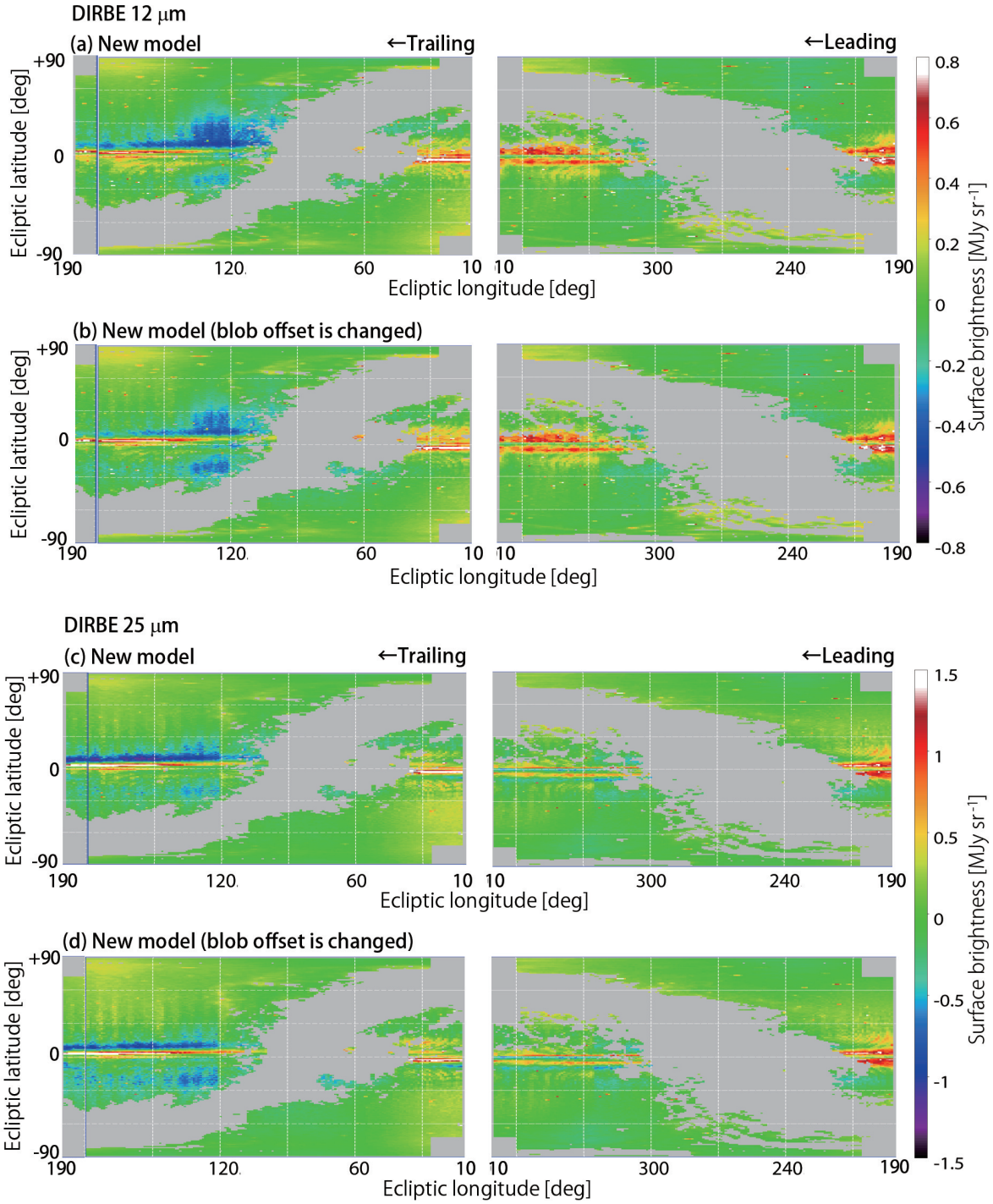

Figure 4.6 DIRBE Solar Elongation = 90 deg Sky Maps in the ecliptic coordinates, after subtraction of the zodiacal emission with the models denoted in the figure. Panels (a) and (c) show the residuals after subtraction of the zodiacal emission with the new model at 12 and 25 μm, respectively. Panels (b) and (d) show the residuals after subtraction of the zodiacal emission with the new model where the vertical offset of the Earth-trailing blob, $Z_{0,\mathrm{TB}}$, is changed to better fit the DIRBE data at 12 and 25 μm, respectively. The arrow shown in the top right of each map indicates the direction of the shift of the scan path, which is useful for comparison with the *AKARI* maps in Fig. 4.1.

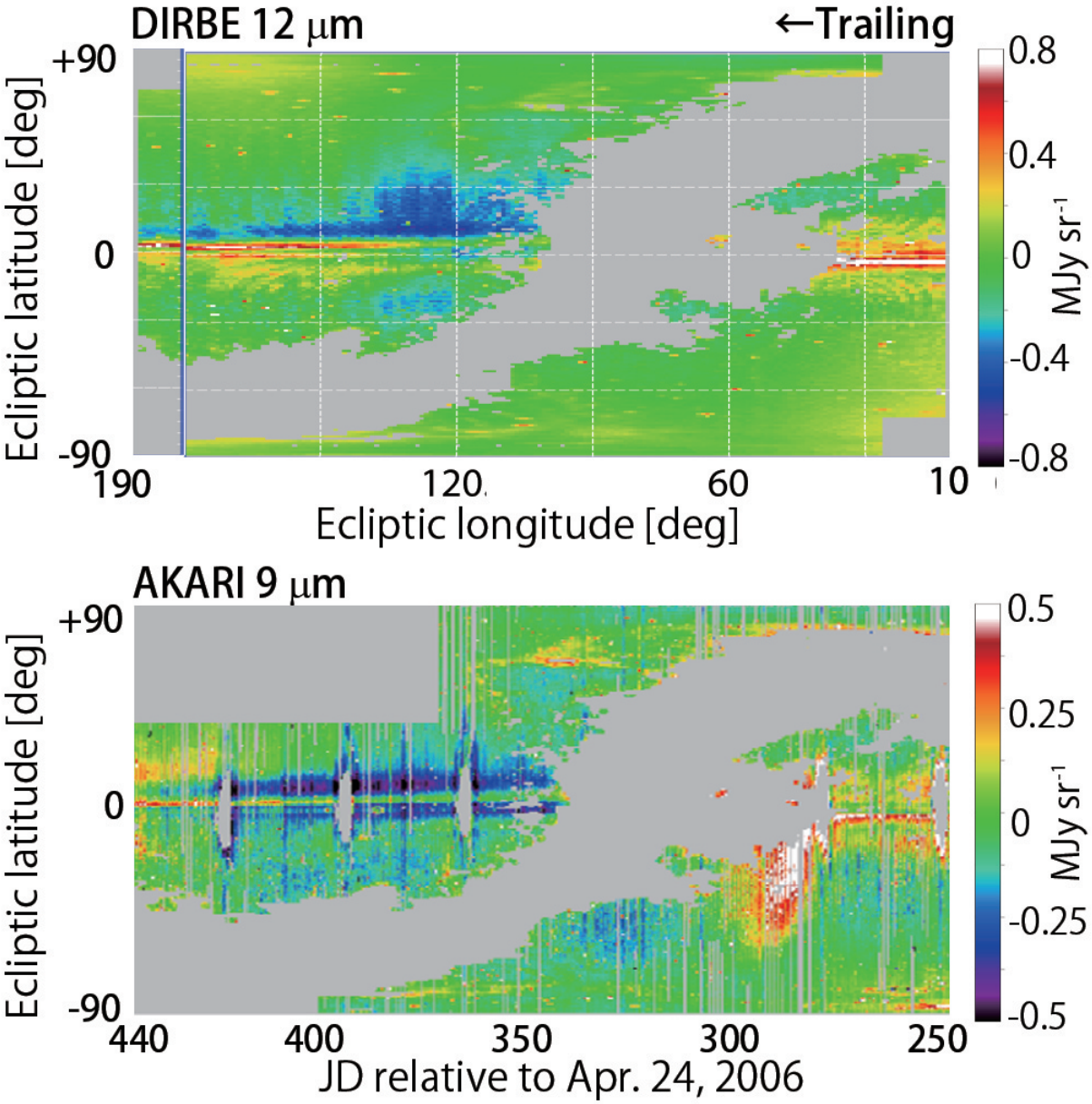

Figure 4.7 DIRBE 12 μm and *AKARI* 9 μm trailing-side maps after subtraction of the zodiacal emission with the new model.

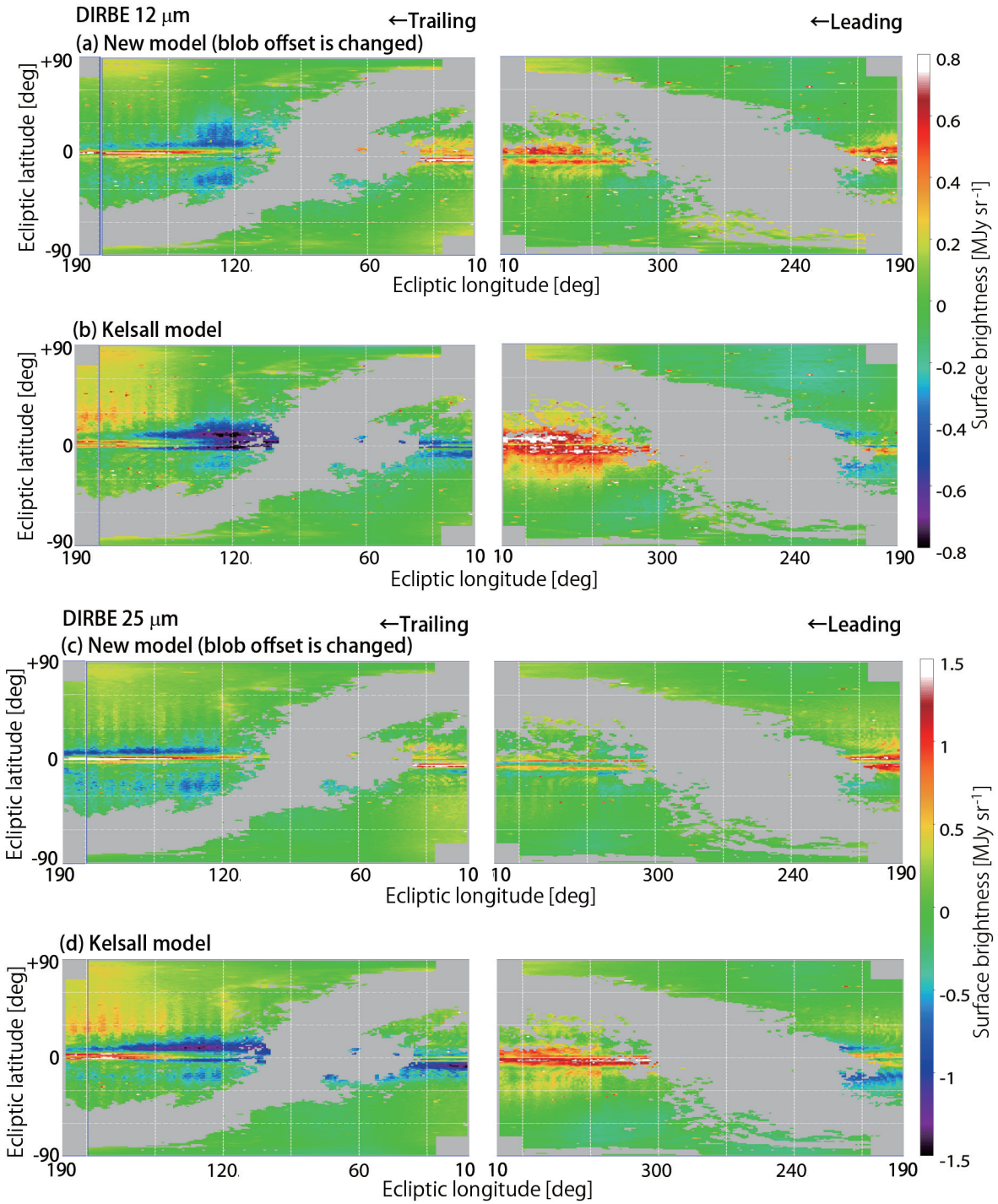

Figure 4.8 DIRBE Solar Elongation = 90 deg Sky Maps in the ecliptic coordinates, after subtraction of the zodiacal emission with the models denoted in the figure. Panels (a) and (c) show the residuals after subtraction of the zodiacal emission with the new model where the vertical offset of the Earth-trailing blob, $Z_{0,\mathrm{TB}}$, is changed to better fit the DIRBE data at 12 and 25 μm, respectively. Panels (b) and (d) show the residuals after subtraction of the zodiacal emission with the Kelsall model at 12 and 25 μm, respectively.

Chapter 5

Discussion

5.1 Radial Distribution

The radial power-law index of the dust density of the smooth cloud, α, becomes significantly larger than that of the Kelsall model from 1.34 to 1.59, which suggests that the cloud size has shrunk in the new model. Table 5.1 shows the α values in the present study and other representative studies. Among them, the present study shows the second largest value. The radial distribution of the dust density depends on the orbital evolution of the IPD grains, where the radiation pressure force from the Sun plays an important role. The orbital evolution of the IPD grains varies with the ratio of the radiation pressure force, $F_{\rm rad}$, to the gravitational force of the Sun, $F_{\rm grav}$. The IPD grains of $F_{\rm rad}/F_{\rm grav} > 0.5$ (typical grain radii < 0.4 μm; Burns et al. 1979) are blown off toward outer regions of our Solar System by the radiation pressure (Ishiguro & Ueno 2003). They are called β meteoroids (Zook & Berg 1975). On the other hand, the IPD grains with sizes lager than β meteoroids are decelerated by the radiation pressure owing to the orbital motion of the grains, and hence the IPD grains fall into the Sun (the Poynting-Robertson effect) with the time scale of 400 $R^2/(F_{\rm rad}/F_{\rm grav})$ years, where R is the distance from the Sun in units of AU (Burns et al. 1979).

If the IPD grains are constantly falling into the Sun from outer regions of our Solar System by the Poynting-Robertson effect without additional dust supply and dust destruction, the number of the IPD grains passing a spherical surface of the radius R per unit time should be constant as

$$4\pi R^2 v_R(R) n(R) = const., \tag{5.1}$$

where $v_R(R)$ is the radial velocity of the IPD grains at R. Because the Poynting-Robertson effect predicts that $v_R(R)$ is inversely proportional to R (Whipple 1955), the dust density, $n(R)$, should also be inversely proportional to R from equation (5.1), that is $\alpha = 1$. Not only the present study

Table 5.1 Comparison of the radial distribution of the IPD cloud between the present study and other representative studies

	Data	Density power-law index (α)	Temperature power-law index (δ)
Dumont & Sánchez (1975)	Teide Observatory	1.2	···
Leinert et al. (1981)	*Helios 1/2*	1.30 (0.05)	···
Rowan-Robinson et al. (1990)	*IRAS*	1.3 (fixed)	0.5 (fixed)
Jones & Rowan-Robinson (1993)	*IRAS*	1.0 (fixed)	0.5 (fixed)
Wheelock et al. (1994)	*IRAS*	1.80 (0.01)	0.359 (0.004)
Wright (1998)	DIRBE	1.22	0.445
Kelsall et al. (1998)	DIRBE	1.34 (0.02)	0.467 (0.004)
Rowan-Robinson & May (2013)	*IRAS* & DIRBE	1.3 (fixed)	0.5 (fixed)
Present study	*AKARI*	1.59 (0.02)	0.458 (0.006)

The values in the parentheses indicate 1σ errors.

but also Kelsall et al. (1998) and other previous studies in Table 5.1, except for those in which α was fixed at 1, show α values significantly larger than unity. To interpret the difference between the expected and the observed values, the previous studies have suggested dust supply mechanisms in inner regions other than migrating dust from outer regions of our Solar System. For example, Leinert et al. (1983) and Grün et al. (1985) showed that the probability of the dust production due to the collision of large grains decreases with the distance from the Sun, and Ishimoto (2000) suggested that a large amount of the dust may be supplied by comets around 1 AU. The present study strongly supports the necessity of such dust supply around 1 AU.

On the other hand, the power-law index of the radial distribution of the dust temperature, δ, is not significantly changed from that in the Kelsall model. If the dust grains emit the blackbody radiation in the thermal equilibrium, the energy balance between the absorption of the sunlight and the IR emission for a dust grain is represented as

$$\frac{L_\odot}{4\pi R^2} \times \pi a^2 = \sigma T^4 \times 4\pi a^2, \tag{5.2}$$

where $L_\odot$ is the solar luminosity, a is a grain radius, and σ is the Stefan-Boltzmann constant. In this condition, the dust temperature, T, is inversely proportional to $R^{0.5}$, that is $\delta = 0.5$. However, the δ values in both new model and Kelsall model are significantly smaller than 0.5. Other previous studies in Table 5.1, except for those in which δ was fixed at 0.5, also showed δ values smaller than 0.5. The present study is based on only the mid-IR data, while the others are on both mid- and far-IR data. Therefore, the present study indicates that the dust sizes are not large enough ($\lesssim 1$

μm) to emit the blackbody radiation even in the mid-IR, i.e., at relatively short wavelengths.

5.2 Time Variation of the Blob Structure

As mentioned in Section 4.3, the Earth-trailing blob is likely to have a vertical offset to the north direction and that the offset has been changed by about 0.014 AU to the north direction between the *COBE* and the *AKARI* epoch. It may suggest that the dust is recently supplied by comets near the Earth, asymmetrically trapped on the trailing side of the Earth (i.e., a larger amount or closer to the Earth in the north than in the south).

The mass of the supplied dust is roughly estimated below, in case of a larger amount of dust trapped on the north side. For the model distribution of the Earth-trailing blob, increasing the brightness on the north side by 20% uniformly leads to the shift of the centroid of the blob by 0.014 AU. Assuming that the flux is simply proportional to the dust mass, the 20% increase in the flux of the north-side Earth-trailing blob corresponds to the 10% increase of the total dust mass of the Earth-trailing blob. Assuming the shape of the Earth-trailing blob as an ellipsoid, the volume is calculated to be

$$V_{\rm TB} \sim \frac{4\pi}{3}\sigma_{\rm rTB}\sigma_{\rm zTB} \times 2R_{\rm TB}\tan\left(\frac{\sigma_{\theta\rm TB}}{2}\right) \sim 0.013 \ \ [{\rm AU}^3] = 4.4 \times 10^{37} \ \ [{\rm cm}^3], \tag{5.3}$$

where $\sigma_{\rm rTB}$ is the radial dispersion, $\sigma_{\rm zTB}$ is the vertical dispersion, $R_{\rm TB}$ is the radius of the peak density, and $\sigma_{\theta\rm TB}$ is the longitude dispersion of the Earth-trailing blob, which are listed in Table 4.1. These dispersions of the distribution of the Earth-trailing blob are simply regarded as the semi-axis lengths. The unit of the longitude dispersion, $\sigma_{\theta\rm TB}$, is converted from degree to AU at the blob position, $R_{\rm TB}$. Rowan-Robinson & May (2013) evaluated the mass density of the smooth cloud at $R = 1.53$ AU in the ecliptic plane to be $\rho \sim 10^{-23.3}$ g cm^{-3}. Then, the mass density of the Earth-trailing blob, $\rho_{\rm TB}$, is calculated as

$$\rho_{\rm TB} = \rho \times \frac{n_{\rm TB}}{n_0 \times 1.53^{-\alpha}} = 1.3 \times 10^{-24} \ \ [{\rm g\ cm}^{-3}], \tag{5.4}$$

where $n_{\rm TB}$ is the dust density of the Earth-railing blob at 1 AU, n_0 is the dust density of the smooth cloud at 1 AU, and α is the radial power-law index of the dust density of the smooth cloud. Using the above results, the blob mass is estimated as

$$M_{\rm TB} \sim V_{\rm TB} \ \ [{\rm cm}^3] \times \rho_{\rm TB} \ \ [{\rm g\ cm}^{-3}] \sim 6 \times 10^{13} \ \ [{\rm g}]. \tag{5.5}$$

Then, the mass of the supplied dust is $\sim 6 \times 10^{12}$ g under the above assumption. This amount of the dust can be ejected by one comet (e.g., Sarugaku et al. 2015).

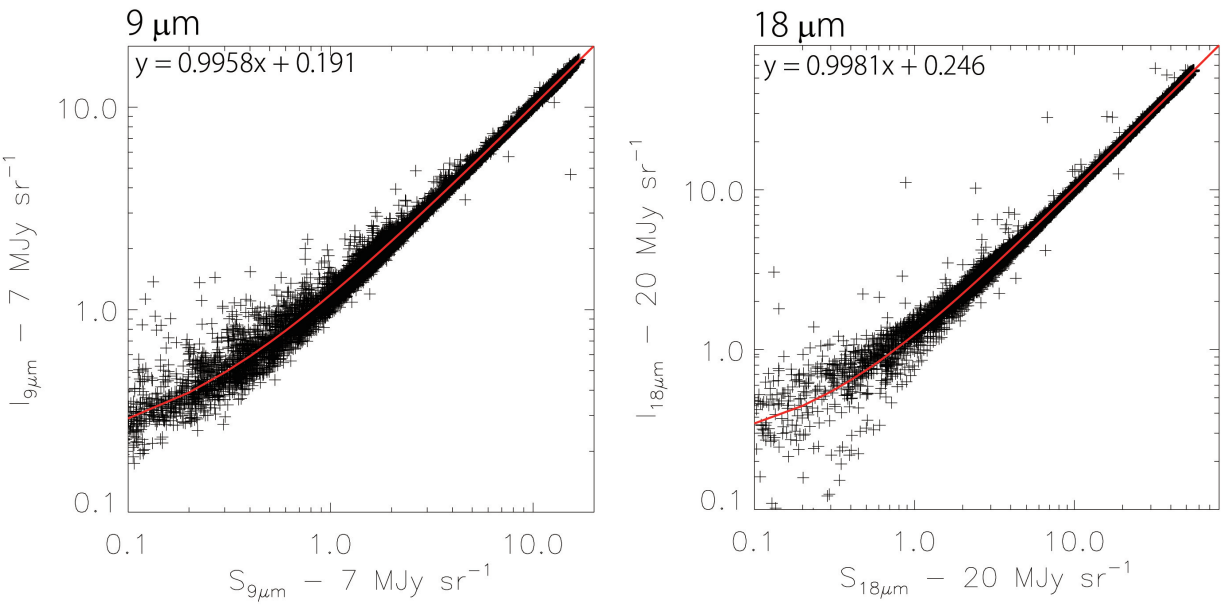

Figure 5.1 Correlation plots between the observed brightness I_λ and the predicted brightness S_λ by the model excluding the isotropic component. In order to show the presence of a small offset in the observed brightness, 7 and 20 MJy sr^{-1} are subtracted at 9 and 18 μm, respectively, from both I_λ and S_λ values for a display purpose. Lines represent the best-fit result of linear fitting to the data points.

5.3 Origin of the IPD

For simplicity, the emissivity modification factor at 9 μm, $\varepsilon_{9\mu\mathrm{m}}$, is assumed to be the same among all the three cloud components in this study. However, it is possible that the $\varepsilon_{9\mu\mathrm{m}}$ values are different among these components, owing to difference in the major origins of the IPD (i.e., cometary or asteroidal) and difference in the size distribution of the IPD grains. In order to test this possibility, the $\varepsilon_{9\mu\mathrm{m}}$ values are allowed to vary among these components. As a result, changes in $\varepsilon_{9\mu\mathrm{m}}$ are not significant; the change is smaller than 3σ for the dust bands and that is smaller than 1σ for the MMR component, based on the χ^2 statistics. Hence, the present study does not call for the difference of the dust properties among the three cloud components.

In addition to IPD grains of cometary and asteroidal origins, previous studies suggested the existence of IPD grains of interstellar origins as mentioned in Section 1.1.3. The emission from the IPD grains of interstellar origins (i.e., IPD which comes from outside our Solar System) is considered to be observed as an isotropic component (e.g., Rowan-Robinson & May 2013). In order to evaluate the brightness of the isotropic component, C_λ, we fit the relation between the observed brightness and the brightness predicted by the model excluding the isotropic component with a line as shown in Fig. 5.1. The intercepts of the fitted lines are 0.191 ± 0.004 MJy sr^{-1} and 0.246 ± 0.009 MJy sr^{-1} at 9 and 18 μm, respectively, while the slopes are 0.9958 ± 0.0003 and 0.9981 ± 0.0002 at 9 and

18 μm, respectively. Thus even considering the error of the dark current measurement (0.03 and 0.06 MJy sr^{-1} at 9 and 18 μm, respectively) mentioned in Section 2.1, the presence of the isotropic component is significant. Other than the IPD grains of interstellar origins, the isotropic component can be Galactic diffuse ISM or cosmic IR background (CIB) (e.g., Hauser et al. 1998; Arendt et al. 1998). Arendt et al. (1998) estimated the DIRBE 12 μm brightness of the Galactic diffuse ISM emission to be $\sim$ 0.03 MJy sr^{-1} in the high ecliptic ($\beta \sim 45°$) and galactic ($b \sim 53°$) latitude regions. The CIB model of Fall et al. (1996) showed that the brightness of CIB is lower than 0.01 MJy sr^{-1} in the DIRBE 12 μm band. These values are about an order of magnitude smaller than the brightness of the isotropic component estimated from the *AKARI* data. Therefore, emission from the IPD grains of interstellar origins is likely to make a dominant contribution to the isotropic component.

Since the IPD grains of interstellar origins are considered to have sizes smaller than IPD grains of internal origins (e.g., Grün et al. 1993), the modified blackbody model is used to estimate the temperature of the isotropic component from the 9 and 18 μm brightnesses. For the emissivity power-law index of unity, the temperature is estimated to be 270 ± 30 K. This value is reasonable for the temperature of dust grains at $\sim$1 AU.

5.4 Small-Scale Structures of the Dust Bands

Most of the geometrical parameters of the dust bands were fixed at those used in the Kelsall model because the present study focuses on large-scale structures of the IPD cloud. However, those model parameters of the small-scale structures are yet to be further optimized, because the small-scale residuals mostly coming from the dust bands are clearly seen in the residual maps in Fig. 4.1. The top panel of Fig. 5.2 shows the distribution of the dust bands at 18 μm, which is the residual map after subtraction of the zodiacal emission other than the dust bands with the new model. The bottom panel of Fig. 5.2 shows the model map of the dust bands at 18 μm. By comparing the top with the bottom panels, the model appears to reproduce the actual global distribution of the dust bands fairly well.

In order to check the difference between the observed data and the model in detail, the cutting profiles at the ecliptic longitudes of 20° and 180° are created on the leading and the trailing sides as shown in Fig. 5.3. By comparing the observed cutting profiles of the dust bands with those predicted by the new model, it is clear that the model reproduces the positions of the dust bands very well. However, the observed widths of the band-1 profiles of the observed data look narrower than those predicted by the model. The observed brightness of band 3 is probably higher than that predicted by the model, because faint peaks are recognized at $\lambda = \pm 16°$–$20°$ on the observed

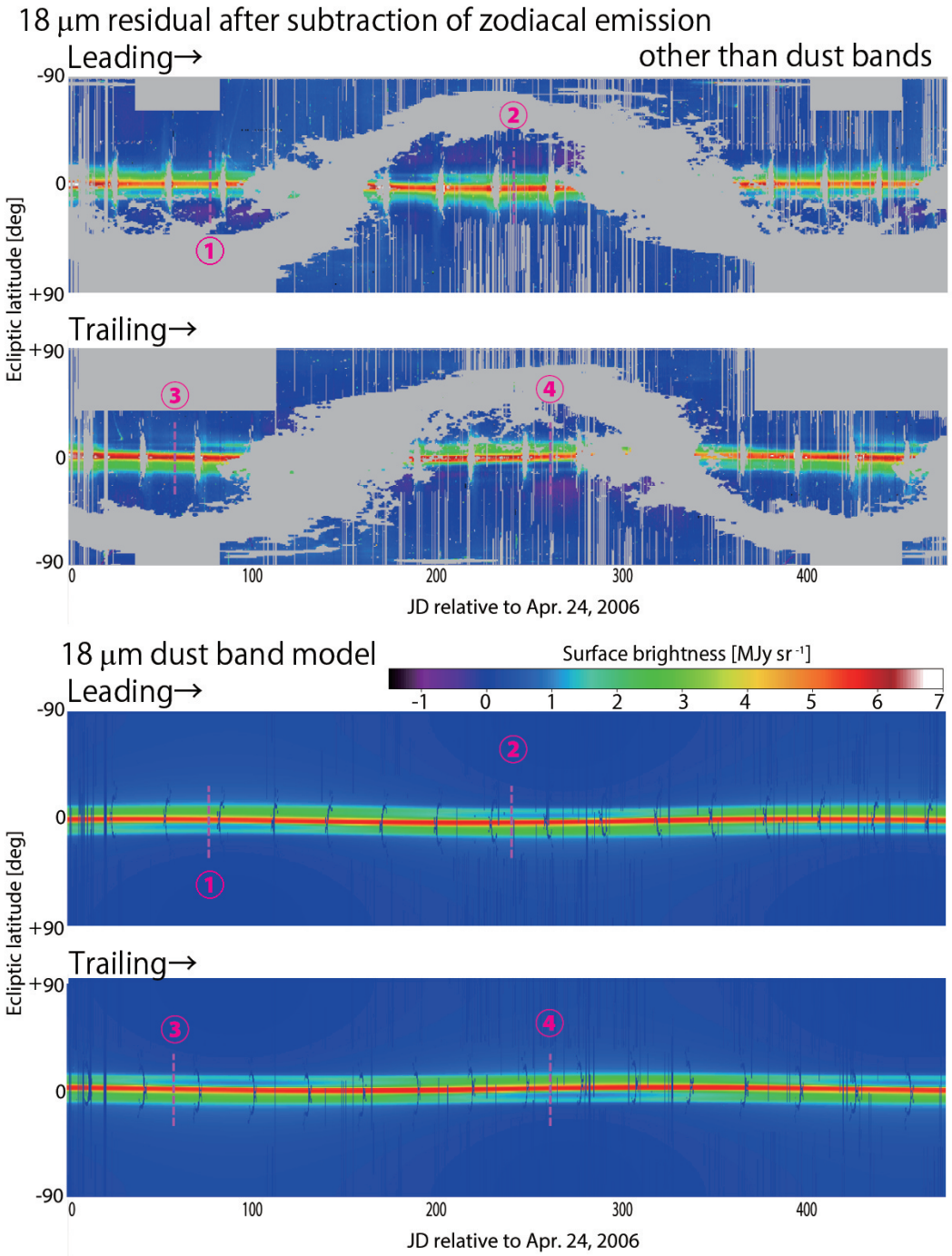

Figure 5.2 Top: *AKARI* 18 μm map after subtraction of the zodiacal emission without the dust bands with the new model. Bottom: the model map of the dust bands at 18 μm. The dashed magenta lines indicate the positions of the cutting profiles in Fig. 5.3.

profiles, whereas they are not recognized on the model profiles.

Furthermore, the model reproduces the widths of the band-2 profiles but the peaks of the observed profiles are narrower than those of the model profiles. The double peak structure is not recognized from these profiles as mentioned in Section 4.2, even though the previous studies indicated the existence of the double peak structure (e.g., Reach et al. 1997; Pyo et al. 2009). For example, Figure 5.4 shows the cutting profiles of the dust bands predicted by the Kelsall model for the same regions as Fig. 5.3. They clearly show the double peaks on band 2. Therefore, even if the double peaks exist, they are not so strong as estimated by Kelsall et al. (1998); they may have overestimated the brightness of the double peaks. It is possible that the observed brightness of the double peaks is much lower than that of the larger-scale structure of band 2. In order to confirm whether or not the double peak structure exists in the observed data, Figure 5.5 shows the observed cutting profiles after applying the spatial band-pass-filter with angular sizes between 1° and 10°, which are the angular sizes of the double peak structure expected by Reach et al. (1997), to the profiles in Fig. 5.3, by utilizing the Fourier transform. As can be seen in this figure, the band-2 structure splits into double peaks, which means that the double peak structure indeed exists but the brightness is as low as about half of that previously thought. For more accurate modeling of the dust bands, the smaller-scale structures such as the double peaks should be separately determined from the larger-scale structures although the contribution of the double peak structure has been removed in the new model as mentioned in Section 4.2.

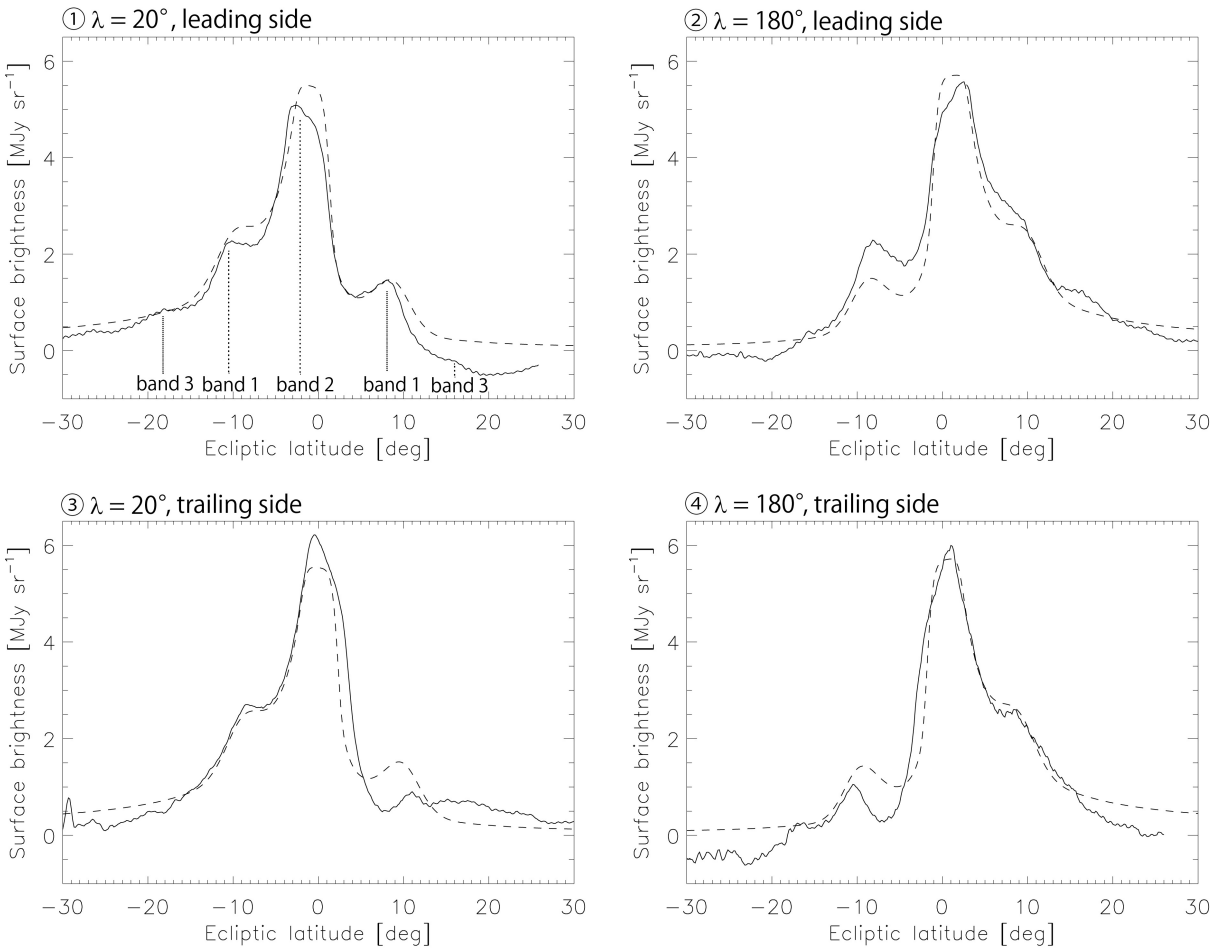

Figure 5.3 Cutting profiles of the dust bands whose positions are indicated by the dashed magenta lines in Fig. 5.2. Solid and dashed lines represent the observed and the model predicted brightnesses, respectively. The labels correspond to those in Fig. 5.2: (1) $\lambda = 20°$ on the leading side, (2) $\lambda = 180°$ on the leading side, (3) $\lambda = 20°$ on the trailing side, and (4) $\lambda = 180°$ on the trailing side.

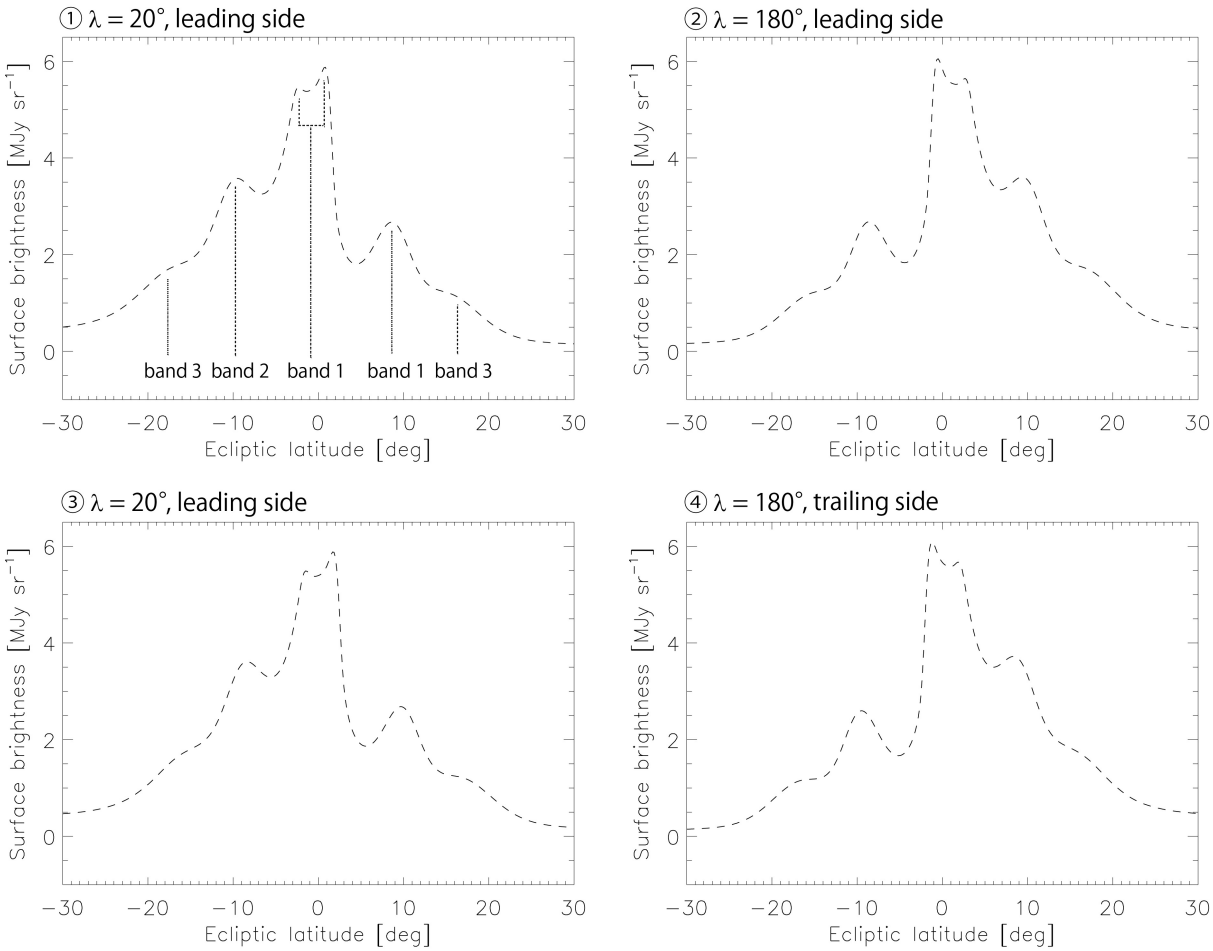

Figure 5.4 Cutting profiles of the dust bands predicted by the Kelsall model, whose positions are the same as those in Fig. 5.3.

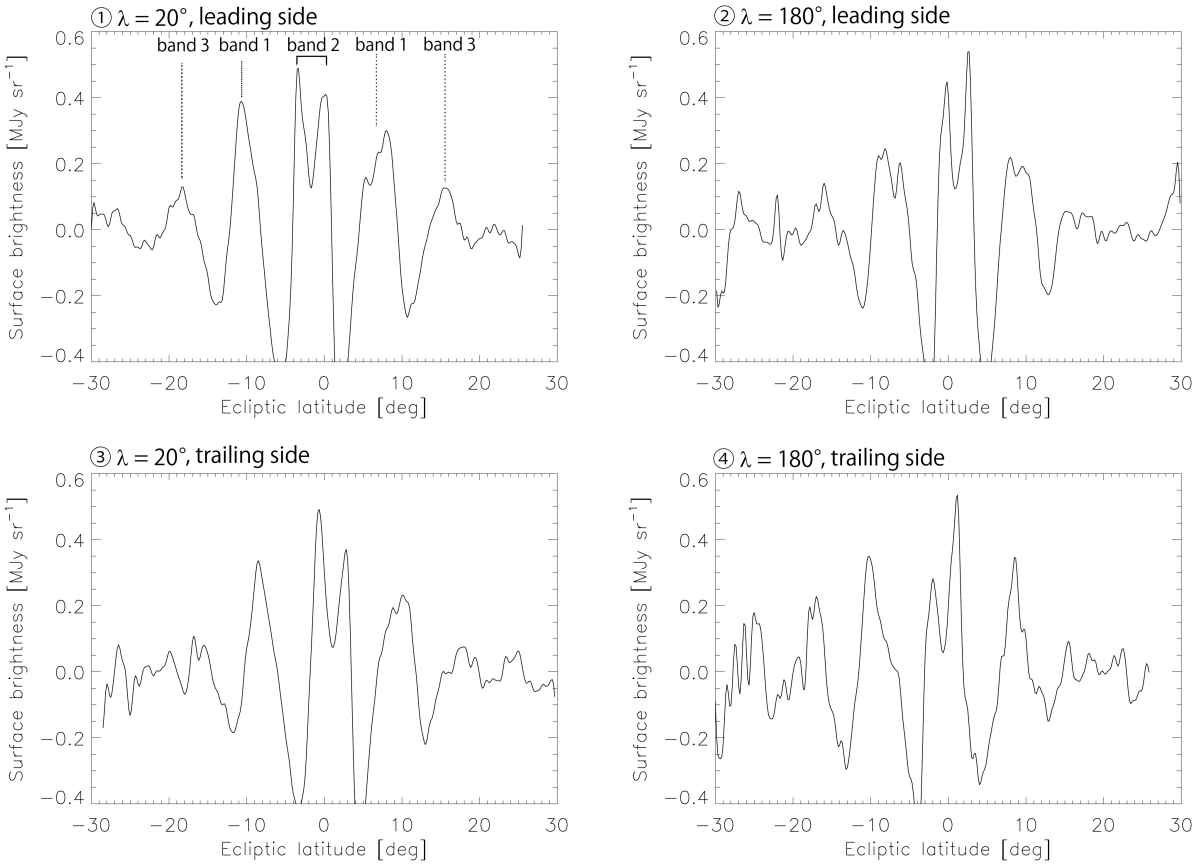

Figure 5.5 Cutting profiles of the dust bands which are spatially band-pass-filtered with angular sizes between 1° and 10° by utilizing the Fourier transform. They are produced from the cutting profiles in Fig. 5.3.

5.5 Likely Local Cloud Passing near the Earth

Through the analysis, in the 9 μm map, we found a likely local cloud passing near the Earth which was serendipitously detected by the *AKARI* all-sky survey. The position of the component is indicated by the solid boxes in Fig. 5.6. It is obviously not the Galactic emission because it appears only on the trailing side; this component is not recognized on the leading side at the same celestial position indicated by the dashed boxes. That large structure cannot be explained by any instrumental artifacts. Thus, this may be a small cloud crossing the Earth's orbit. The flux of the cloud is calculated to be $21,000 \pm 2,000$ Jy and $\leq 11,000$ Jy (3σ upper limit) at 9 and 18 μm, respectively, for the rectangular area of $8^\circ \times 25^\circ$ in Fig. 5.6. The errors are estimated from the brightness fluctuations in the adjacent area of $8^\circ \times 15^\circ$ to the south. The 9 μm flux and the 18 μm flux upper limit indicate that the temperature of the cloud may be higher than 700 K assuming the blackbody radiation. This temperature is considerably higher than that of IPD clouds around the Earth, so that the cloud may have come from inner regions of our Solar System with a high velocity.

The existence of this component is recognized during about 20 days since 2007 January 29. One possibility is that it originates in the coronal mass ejection (CME), because the CME event occurred on 2007 January 25 (e.g., Grigoryeva et al. 2009; Webb et al. 2009) and the CME front was observed at the solar elongation of 90° on 2007 January 29 by the Solar Mass Ejection Imager (SMEI) aboard the *Coriolis* satellite as shown in Fig. 5.7 (Webb et al. 2009). Figure 5.8 shows the fish-eye view of the interplanetary CME brightness distribution taken with the SMEI on 2007 January 29. As can be seen in this figure, the brightness is relatively high in the south region on the trailing side, which corresponds to the region where the likely local cloud is detected in the *AKARI* maps. The local cloud may consist of nanometer-sized dust grains, because the *STEREO*/WAVES data showed that the probability of detecting the flux of nanometer-sized dust grains is higher when the CMEs occur than the probabilities in the other situations (Le Chat et al. 2015). The nanometer-sized dust grains whose velocities are about 300 km s^{-1} have been detected at around 1 AU by the *International Space Station* (Carpenter et al. 2007) and the *STEREO* spacecraft (Meyer-Vernet et al. 2009). Czechowski & Mann (2010) carried out simulations of grain dynamics to show that nanometers-sized dust grains in inner regions of our Solar System are accelerated to a solar wind speed through interaction with interplanetary magnetic field due to high ratios of the charge to mass of the nanometer-sized dust grains. Le Chat et al. (2015) suggested that the nanometer-sized dust grains, which have already been accelerated by the above mechanism, are transfered to around 1 AU with the CMEs, using the *STEREO*/WAVE data. Therefore, the present study may provide another observational evidence for the interaction between the nanometer-sized dust grains and the CME.

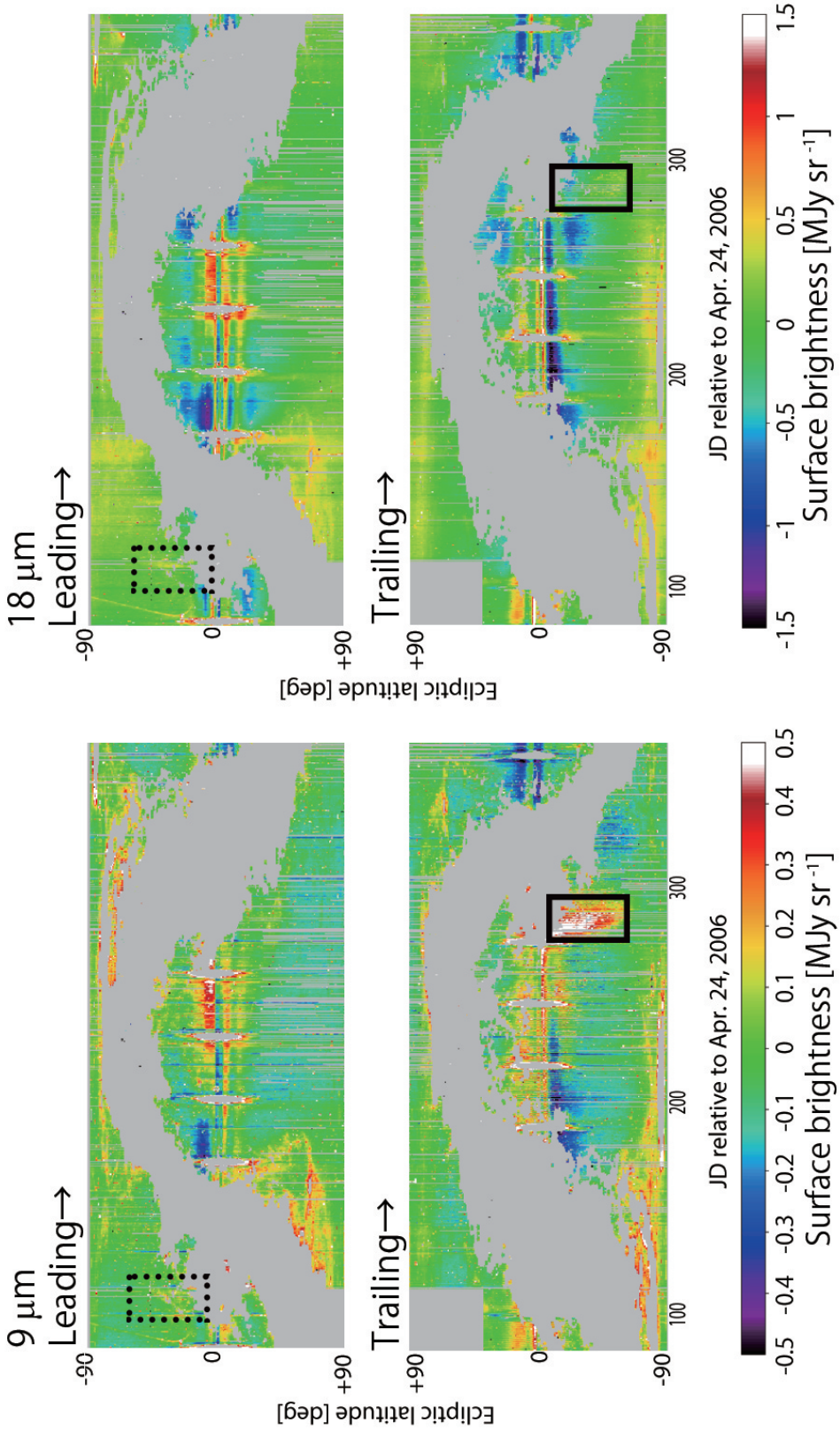

Figure 5.6 A part of the *AKARI* mid-IR maps after subtraction of the zodiacal emission with the new model in Fig. 4.1. Solid boxes indicate the position of a likely local cloud passing near the Earth. For comparison, dashed boxes are drawn at the same celestial position on the leading side.

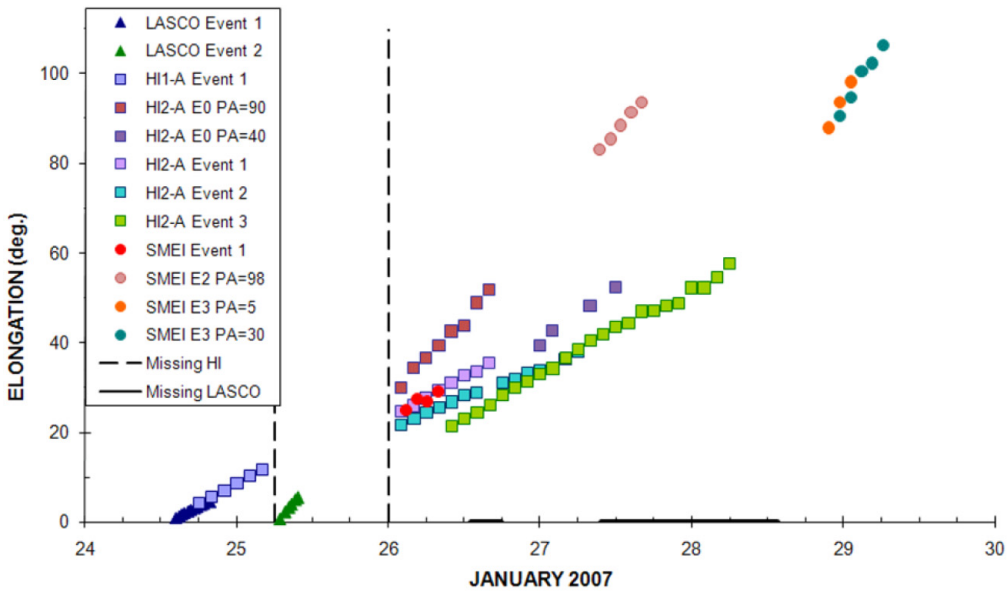

Figure 5.7 Solar elongation of the CME fronts as a function of the date. The CME fronts were observed from 2007 January 24–30 by the *SOHO*/LASCO, the *Coriolis*/SMEI, and the *STEREO*/HIs (Webb et al. 2009).

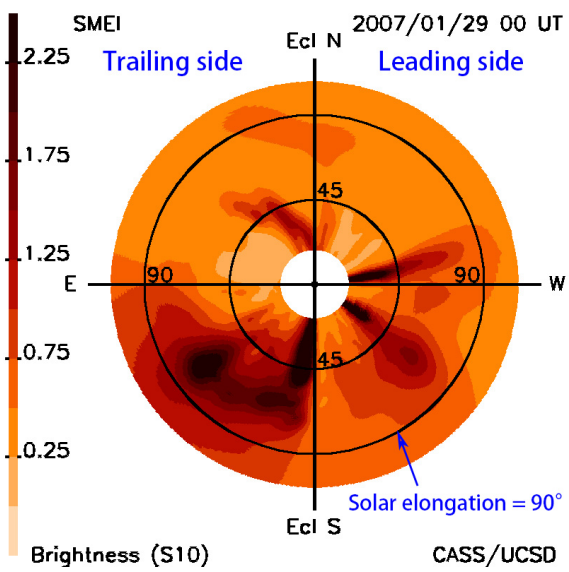

Figure 5.8 Fish-eye view of the interplanetary CME brightness distribution taken from the SMEI on 2007 January 29. This figure is obtained from the SMEI website.[2]

[2] http://smei.ucsd.edu/new_smei/index.html

Chapter 6

Final Products and Future Works

Figure 6.1 shows the *AKARI* 9 and 18 μm all-sky maps in the galactic coordinates. In these maps, the Galactic diffuse components spread above and below the Galactic plane. However, the residuals of the zodiacal emission still remain along the ecliptic plane, especially in the 18 μm map. These residuals most likely come from the dust bands. In Fig. 6.2, the regions of surface brightness levels lower than 0.24 and 0.60 MJy sr^{-1} are masked at 9 and 18 μm, respectively. These levels correspond to 3σ, where σ is the RMS value in the residual maps after subtraction of the zodiacal emission in Fig. 4.1. In the 9 μm map, the Galactic diffuse components are significantly detected in the regions of $|b| \leq 15°$ at almost every galactic longitude. In particular, in the Scorpio and the Ophiuchus regions ($l \sim 0°$) and the Taurus and the Orion regions ($l \sim 180°$), the emission reaches such high galactic latitudes as $|b| \sim 45°$. Figure 6.3 shows an enlarged view of the Taurus and the Orion regions in the 9 μm map, where the emission exhibits intricate patterns of extended filamentary structures. Since we consider that the PAH emission makes a dominant contribution to the 9 μm emission, PAHs are likely to exist widely in filamentary structures in our Galaxy. On the other hand, in the 18 μm map, the regions where the emission is significantly detected are more compact than those in the 9 μm map. Considering that the 18 μm map traces the distribution of very small grains (VSGs) stochastically heated to high temperatures ($\sim$ 100 K), the compact distribution may be reasonable. However, since there still remain larger residuals of the zodiacal emission in the 18 μm map than in the 9 μm map, the possibility of the existence of the VSG emission at high Galactic latitudes cannot be ruled out from the 18 μm map. We therefore plan to carry out more accurate modeling of smaller-scale structures of the zodiacal emission such as the dust bands, so that we can investigate whether even fainter Galactic emission exists or not in high-latitude regions.

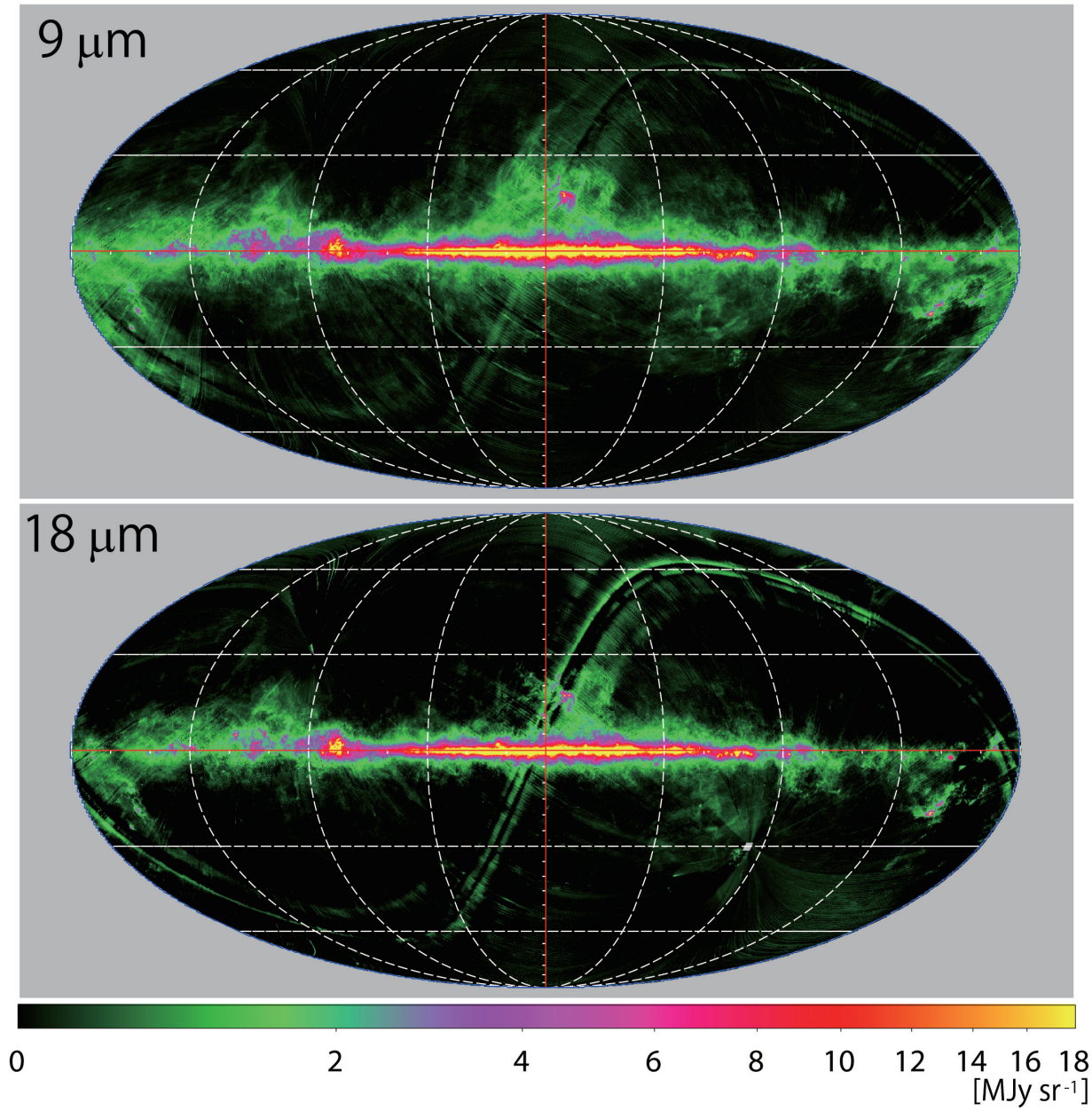

Figure 6.1 *AKARI* 9 and 18 μm all-sky maps after subtraction of the zodiacal emission in the galactic coordinates.

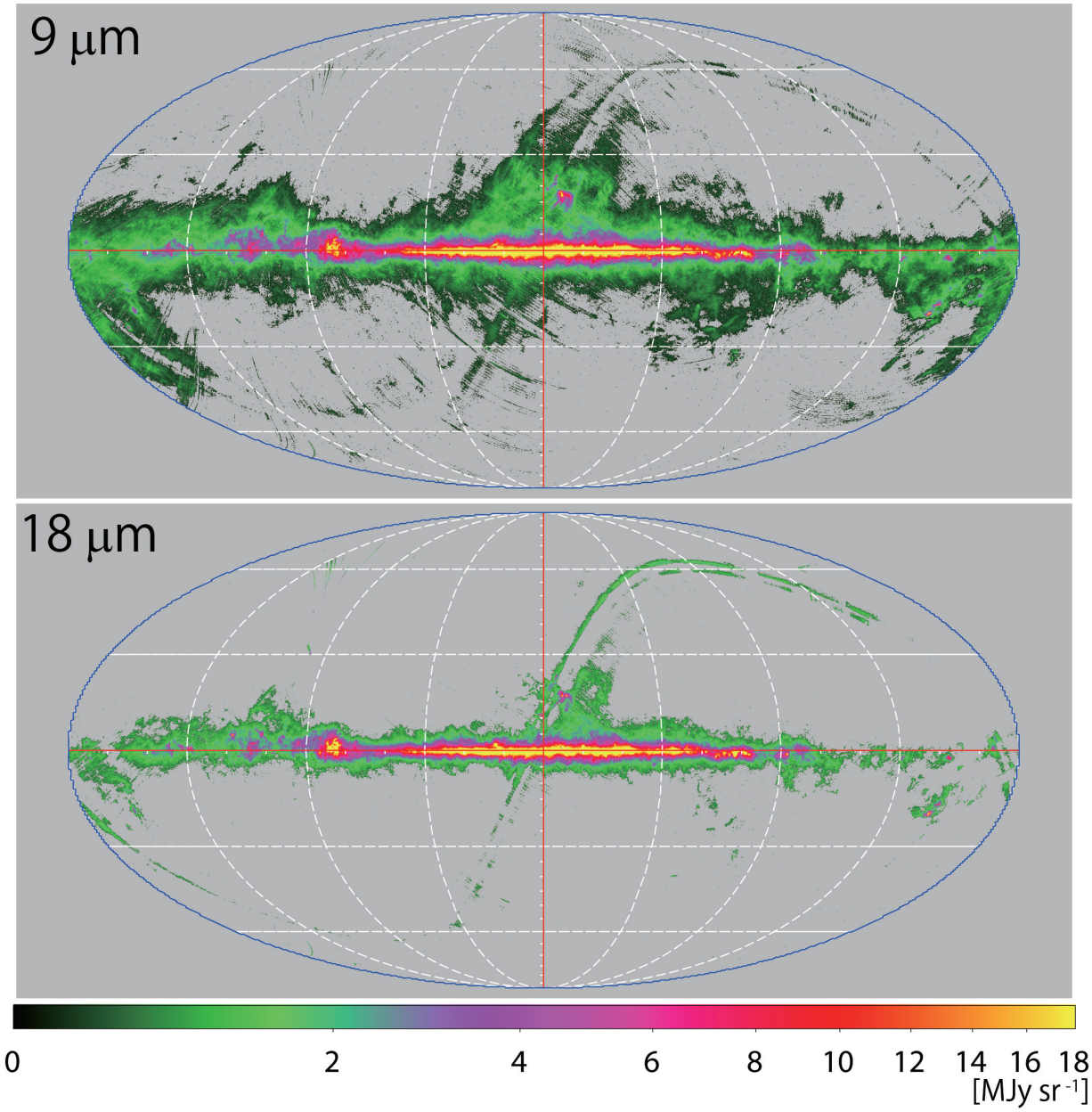

Figure 6.2 Same as Fig. 6.1, but the regions of surface brightness levels lower than 0.24 and 0.60 MJy sr^{-1} are masked at 9 and 18 μm, respectively.

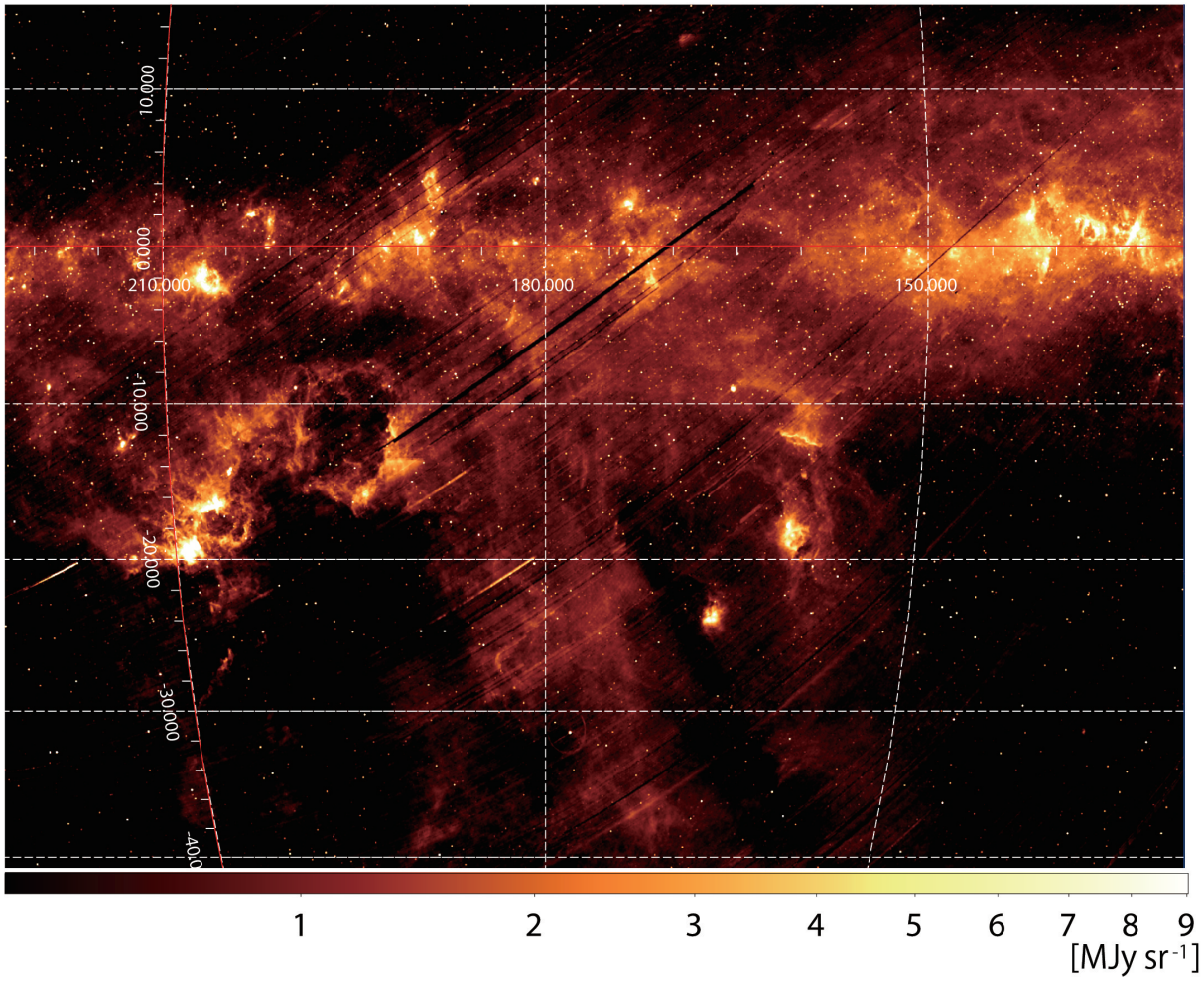

Figure 6.3 Enlarged view of the the Taurus and the Orion regions for an area of about $80° \times 60°$. The color and the scale are changed from Fig. 6.1 to emphasize filamentary structures.

Chapter 7

Summary

We have carried out the modeling of the zodiacal emission, using the *AKARI* 9 and 18 μm all-sky data which have higher spatial resolution than the *COBE* and the *IRAS* data. Before modeling the zodiacal emission, we produced the *AKARI* mid-IR all-sky diffuse maps through many data processes such as corrections for reset anomaly and non linearity of the detector, the ionizing radiation effect by high-energy cosmic rays, and scattered light from the moon. Since previous models have not been successful to reproduce the all-sky distribution of the zodiacal emission, we changed the fitting method from Kelsall et al. (1998); we modeled the absolute intensity of the zodiacal emission on a large-scale and a small-scale structure separately by taking a step-by-step procedure.

In this study, the following results are obtained:

1. The new model successfully reduces the residual levels in the *AKARI* 9 and 18 μm all-sky maps after subtraction of the zodiacal emission. The RMS values of the residual components improve from 0.16 to 0.08 MJy sr^{-1} at 9 μm and from 0.31 to 0.20 MJy sr^{-1} at 18 μm from the Kelsall model to the new model.

2. The radial distribution of the dust density of the smooth cloud is steeper than previously thought. This result suggests the necessity of extra dust supply mechanisms around 1 AU in addition to the migrating dust from outer regions of our Solar System by the Poynting-Robertson effect.

3. The radial distribution of the dust temperature is significantly different from the distribution expected if the dust grains emit the blackbody radiation in the thermal equilibrium. The present study indicates that the dust sizes are not large enough to emit the blackbody radiation in the mid-IR.

4. An isotropic component is significantly detected, owing to accurate measurement of dark current with *AKARI*. The brightness is evaluated to be 0.191±0.004 MJy sr^{-1} and 0.246±0.009 MJy sr^{-1} at 9 and 18 μm, respectively. This component is likely to be dominated by the emission from the IPD grains of interstellar origins which come from outside our Solar System, because these brightnesses are an order of magnitude higher than those expected for high-latitude Galactic diffuse emission or CIB. The color temperature is estimated to be 270 ± 30 K, assuming the modified blackbody radiation with the emissivity power-law index of unity. This value is reasonable for the temperature of dust grains at ∼1 AU.

5. The new model reproduces the zodiacal emission in both *COBE* maps and *AKARI* maps significantly better than the Kelsall model. The changes of the model parameters are mostly due to model improvements, but not temporal variations between the *AKARI* and the *COBE* epoch, except for the spatial distribution of the Earth-trailing blob.

6. The Earth-trailing blob is likely to have a vertical offset to the north direction and the offset has been changed by about 0.014 AU to the north direction between the *COBE* and the *AKARI* epoch. The change in the offset may suggest that dust is recently supplied by comets near the Earth, asymmetrically trapped on the trailing side of the Earth.

7. A likely local cloud passing near the Earth was detected serendipitously. The 9 μm flux and the 18 μm flux upper limit indicate that the temperature of the cloud may be higher than 700 K assuming the blackbody radiation. Considering the observed date and position of the cloud, it may be related to the solar CME which took place on 2007 January 25.

We obtain final products of the *AKARI* 9 and 18 μm all-sky diffuse maps after subtraction of the zodiacal emission with the new model. They show the Galactic diffuse emission spreading well above and below the Galactic plane. In particular, the 9 μm map exhibits widely-distributed PAH emission in filamentary structures. However, there still remain non-negligible residuals of the zodiacal emission especially in the 18 μm map. These residuals most likely come from the dust bands. In order to investigate the existence of even fainter Galactic emission due to PAHs and VSGs at high latitudes, we need to carry out further detailed modeling of small-scale structures of the zodiacal emission such as the dust bands.

Acknowledgments

I am deeply grateful to my supervisor Prof. H. Kaneda for showing the way of this study, discussion, and education. I also want to thank Dr. D. Ishihara for a lot of helpful advice on this study and the data analysis of the *AKARI* data. The discussion with Prof. T. Ootsubo, Drs. J. Pyo, H. Kobayashi, and K. Tsumura was very helpful for this study. I would like to thank all the member of the *AKARI* project because this study cannot be carried out without the *AKARI* data. I am financially supported by Grant-in-Aid for JSPS Fellows No. 25002536 and the Nagoya University Program for Leading Graduate Schools, "Leadership Development Program for Space Exploration and Research," from MEXT. Finally, I thank all the members of the laboratory, especially Dr. K. Torii, Mr. K. Nakamichi, and Ms. S. Takaba for the great efforts to produce the *AKARI* mid-IR all-sky maps.

References

Amatsutsu, T. 2015, Master's thesis, Nagoya University

Arendt, R. G., Odegard, N., Weiland, J. L., et al. 1998, ApJ, 508, 74

Baguhl, M., Hamilton, D. P., Grun, E., et al. 1995, Science, 268, 1016

Bertin, E., & Arnouts, S. 1996, A&AS, 117, 393

Burns, J. A., Lamy, P. L., & Soter, S. 1979, Icarus, 40, 1

Carpenter, J. D., Stevenson, T. J., Fraser, G. W., et al. 2007, Journal of Geophysical Research (Planets), 112, E08008

Cassini, J. D. 1685, Découverte de la lumière celeste qui paroist dans le zodiaque (Paris: Imprimerie Royale)

Czechowski, A., & Mann, I. 2010, ApJ, 714, 89

Dermott, S. F., Jayaraman, S., Xu, Y. L., Grogan, K., & Gustafson, B. A. S. 1996, American Institute of Physics Conference Series, 348, 25

Dermott, S. F., Jayaraman, S., Xu, Y. L., Gustafson, B. Å. S., & Liou, J. C. 1994, Nature, 369, 719

Dermott, S. F., Nicholson, P. D., Burns, J. A., & Houck, J. R. 1984, Nature, 312, 505

Doi, Y., Takita, S., Ootsubo, T., et al. 2015, PASJ, 67, 50

Dumont, R., & Sánchez, F. 1975, A&A, 38, 405

Durda, D. D., & Dermott, S. F. 1997, Icarus, 130, 140

Egusa, F., Lorente, R., Onaka, T., et al. 2015, AKARI IRC Data User Manual Version 2.0, available in electronic form from ISAS at `http://www.ir.isas.jaxa.jp/AKARI/Observation`

Fall, S. M., Charlot, S., & Pei, Y. C. 1996, ApJ, 464, L43

Giese, R. H., Kneissel, B., & Rittich, U. 1986, Icarus, 68, 395

Grigoryeva, I. Y., Borovik, V. N., Livshits, M. A., et al. 2009, Sol. Phys., 260, 157

Grogan, K., Dermott, S. F., & Gustafson, B. A. S. 1996, ApJ, 472, 812

Grün, E., Zook, H. A., Baguhl, M., et al. 1993, Nature, 362, 428

Grün, E., Zook, H. A., Fechtig, H., & Giese, R. H. 1985, Icarus, 62, 244

Hanner, M. S., Weinberg, J. L., Beeson, D. E., & Sparrow, J. G. 1976, Interplanetary Dust and Zodiacal Light, 48, 29

Hauser, M. G., Arendt, R. G., Kelsall, T., et al. 1998, ApJ, 508, 25

Ishiguro, M., & Ueno, M. 2003, The Astoronomical Herald, 96, 206

Ishihara, D., Onaka, T., Kataza, H., et al. 2010, A&A, 514, A1

Ishihara, D., Wada, T., Onaka, T., et al. 2006, PASP, 118, 324

Ishihara, D., Wada, T., Watarai, H., et al. 2003, Proc. SPIE, 4850, 1008

Ishimoto, H. 2000, A&A, 362, 1158

Jackson, A. A., & Zook, H. A. 1989, Nature, 337, 629

Jones, M. H., & Rowan-Robinson, M. 1993, MNRAS, 264, 237

Kaneda, H., Ishihara, D., Mouri, A., et al. 2012, PASJ, 64, 25

Kaneda, H., Ishihara, D., Suzuki, T., et al. 2010, A&A, 514, A14

Kaneda, H., Kim, W., Onaka, T., et al. 2007, PASJ, 59, 423

Kaneda, H., Onaka, T., Nakagawa, T., et al. 2005, Appl. Opt., 44, 6823

Kawada, M., Baba, H., Barthel, P. D., et al. 2007, PASJ, 59, 389

Kelsall, T., Weiland, J. L., Franz, B. A., et al. 1998, ApJ, 508, 44

Kondo, T., Kaneda, H., Ishihara, D., et al. 2013, Proceedings of The Life Cycle of Dust in the Universe: Observations, Theory, and Laboratory Experiments (LCDU2013), id.33, online at `http://pos.sissa.it/cgi-bin/reader/conf.cgi?confid=207`

Kondo, T., Kaneda, H., Oyabu, S., et al. 2012a, ApJ, 751, L18

—. 2012b, Publication of Korean Astronomical Society, 27, 257

Le Chat, G., Issautier, K., Zaslavsky, A., et al. 2015, Sol. Phys., 290, 933

Leinert, C., Richter, I., Pitz, E., & Planck, B. 1981, A&A, 103, 177

Leinert, C., Röser, S., & Buitrago, J. 1983, A&A, 118, 345

Liou, J. C., Dermott, S. F., & Xu, Y. L. 1995, Planet. Space Sci., 43, 717

Low, F. J., Beintema, D. A., Gautier, T. N., et al. 1984, ApJ, 278, L19

Marzari, F., & Vanzani, V. 1994a, A&A, 283, 275

—. 1994b, Planet. Space Sci., 42, 101

Meyer-Vernet, N., Maksimovic, M., Czechowski, A., et al. 2009, Sol. Phys., 256, 463

Mori, T. I., Sakon, I., Onaka, T., et al. 2012, ApJ, 744, 68

Mouri, A. 2012, Master's thesis, nagoya University

Mouri, A., Kaneda, H., Ishihara, D., et al. 2011, PASP, 123, 561

Murakami, H., Baba, H., Barthel, P., et al. 2007, PASJ, 59, 369

Nesvorný, D., Bottke, W. F., Levison, H. F., & Dones, L. 2003, ApJ, 591, 486

Nesvorný, D., Bottke, W. F., Vokrouhlický, D., et al. 2008, ApJ, 679, L143

Nesvorný, D., Vokrouhlický, D., Bottke, W. F., & Sykes, M. 2006, Icarus, 181, 107

Onaka, T., Matsuhara, H., Wada, T., et al. 2007, PASJ, 59, 401

Planck Collaboration XIV. 2014, A&A, 571, A14

Pyo, J., Hong, S. S., Kwon, S. M., et al. 2009, AKARI, a Light to Illuminate the Misty Universe, 418, 39

Pyo, J., Ueno, M., Kwon, S. M., et al. 2010, A&A, 523, A53

Reach, W. T., Franz, B. A., & Weiland, J. L. 1997, Icarus, 127, 461

Reach, W. T., Franz, B. A., Weiland, J. L., et al. 1995, Nature, 374, 521

Rowan-Robinson, M., Hughes, J., Vedi, K., & & Walker, D. W. 1990, MNRAS, 246, 273

Rowan-Robinson, M., & May, B. 2013, MNRAS, 429, 2894

Sarugaku, Y., Ishiguro, M., Ueno, M., Usui, F., & Reach, W. T. 2015, ApJ, 804, 127

Schramm, L. S., Brownlee, D. E., & Wheelock, M. M. 1989, Meteoritics, 24, 99

Struve, O. 1943, ApJ, 98, 129

Sykes, M. V. 1990, Icarus, 85, 267

Sykes, M. V., & Greenberg, R. 1986, Icarus, 65, 51

Tanabé, T., Sakon, I., Cohen, M., et al. 2008, PASJ, 60, 375

Verdugo, E., Yamamura, I., & Pearson, C. 2007, AKARI FIS Data User Manual Version 1.3, available in electronic form from ISAS at `http://www.ir.isas.jaxa.jp/AKARI/Observation`

Webb, D. F., Howard, T. A., Fry, C. D., et al. 2009, Sol. Phys., 256, 239

Wheelock, S. L., Gautier, T. N., Chillemi, J., et al. 1994, NASA STI/Recon Technical Report N, 95, 22539

Whipple, F. L. 1955, ApJ, 121, 750

Wright, E. L. 1998, ApJ, 496, 1

Yamagishi, M. 2011, Master's thesis, Nagoya University

Yamagishi, M., Kaneda, H., Ishihara, D., et al. 2012, A&A, 541, A10

Zook, H. A., & Berg, O. E. 1975, Planet. Space Sci., 23, 183